Trabajo Fin de Grado
Ingeniería Aeroespacial

Optimal Planning and Guidance Strategies in Coplanar Circular Interplanetary Missions using Electric Solar Wind Sails

Autor: Fco. Javier Urrios Gómez

Tutores: Guillermo Pacheco Ramos, Rafael Vázquez Valenzuela

Dpto. Ingeniería Aeroespacial y Mecánica de Fluidos
Escuela Técnica Superior de Ingeniería
Universidad de Sevilla

Sevilla, 2022

Trabajo Fin de Grado
Ingeniería Aeroespacial

Optimal Planning and Guidance Strategies in Coplanar Circular Interplanetary Missions using Electric Solar Wind Sails

Autor:
Fco. Javier Urrios Gómez

Tutores:
Guillermo Pacheco Ramos, Rafael Vázquez Valenzuela
Profesor Sustituto Interino, Profesor Titular

Dpto. Ingeniería Aeroespacial y Mecánica de Fluidos
Escuela Técnica Superior de Ingeniería
Universidad de Sevilla

Sevilla, 2022

Trabajo Fin de Grado: Optimal Planning and Guidance Strategies in Coplanar Circular Interplanetary Missions using Electric Solar Wind Sails

Autor: Fco. Javier Urrios Gómez
Tutores: Guillermo Pacheco Ramos, Rafael Vázquez Valenzuela

El tribunal nombrado para juzgar el trabajo arriba indicado, compuesto por los siguientes profesores:

Presidente:

Vocal/es:

Secretario:

acuerdan otorgarle la calificación de:

El Secretario del Tribunal

Fecha:

Agradecimientos

Parece que fue ayer cuando un chaval de 17 años llamado Javier, aunque más conocido como Urrios, entraba a la carrera en Sevilla. Lleno de incertidumbre, pero cautivado por el espacio, la tecnología y las matemáticas, optó por estudiar Ingeniería Aeroespacial. A día de hoy puedo firmemente decir no solo que no me arrepiento, sino que la aventura continúa. Estos cuatro años en la escuela me han servido para afianzarme en la idea de que mi futuro es como ingeniero. Puede que su repercusión en la sociedad no sea tan directa como la de otros ámbitos, pero la tarea a la que se encomienda la ingeniería me parece admirable. Controlar las indomables leyes físicas y matemáticas del universo para ponerlas a disposición del ser humano no debe ser tarea fácil.

Sin embargo, tal y como dice un famoso proverbio chino, "si caminas solo, irás más rápido; si caminas acompañado, llegarás más lejos". Este hito en mi vida no habría sido posible sin la ayuda de esas personas que me apoyan incondicionalmente, y de las que aprendo algo nuevo cada día.

A mis padres, Javier y Cristina, gracias. Gracias por la confianza que habéis depositado en mí, y por haberme enseñado a luchar para convertirme en la mejor versión de mí mismo. La entrega incondicional que demostráis a vuestros hijos es vuestra mejor carta de presentación, y yo solo espero algún día poder educar a los míos igual de bien que lo habéis hecho vosotros.

Gracias a mis amigos, la familia que he tenido la suerte de elegir. Me siento profundamente agradecido de tener compañeros de vida que genuinamente se preocupan por mí. Peña, Pani, Jaime, Miki, Javi y otros muchos igual de importantes, sois la razón por la que, por mucho tiempo que pase, cuando vuelvo a Córdoba siento que nunca me he ido. Rodrigo, Salva, Javi, Fer, Tomás, Jose, gracias por haberme ayudado a disfrutar de esta etapa universitaria como se merece, y por hacerme ver que a veces hay otras cosas igual de importantes, y que todo tiene su momento.

A la generación que me lleva un año de ventaja; Gallo, Mendiola, Miguel, gracias por haber estado en todo momento para lo que necesitara. Vuestro compromiso es digno de admiración y desde luego me habéis servido de guías para afrontar este reto. Gracias también a mis amigos de clase por hacerme la carrera más amena, y en especial a Alejandro, por estar conmigo en todo momento, incluso cuando las cosas se ponían complicadas, eres único.

Sin duda alguna mi etapa universitaria no hubiera sido igual sin el Colegio Mayor San Juan Bosco, mi casa de Sevilla. Gracias a todos los allí presentes por cada una de las enseñanzas y experiencias que me habéis aportado. Entré como un niño y salgo como un hombre. Aquí he descubierto que la vida no se improvisa, y que tenemos mucho que aprender de cada persona que nos rodea. He conocido a Alguacil, Drolu, Linde, Jose e innombrables personas más que me llevo para siempre.

Por último, gracias a mis tutores Rafa y Guillermo, por la disponibilidad y atención que me habéis brindado en todo momento. Gracias a vosotros he podido adentrarme en el apasionante mundo del espacio, y aprender a valorar todo el esfuerzo que hay detrás de cada avance. Es un honor que hayáis confiado en mí para hacer este proyecto.

Fco. Javier Urrios Gómez
Sevilla, 2022

Resumen

Título

Planificación Óptima y Estrategias de Guiado para Misiones Interplanetarias entre Órbitas Circulares Coplanarias con Velas Solares Eléctricas.

Resumen del trabajo

Las Velas Solares Eléctricas son un nuevo tipo de propulsión espacial que no requiere de combustible ya que obtiene la energía de los protones del viento solar, y que es potencialmente útil para misiones interplanetarias. Con un modelo propulsivo apropiado, que puede ser obtenido de la literatura, es posible estudiar órbitas óptimas para vuelos interplanetarios. El primer objetivo de este proyecto es estudiar las propiedades de las órbitas de tiempo mínimo en misiones hacia Marte y Júpiter utilizando un método indirecto aplicando las ecuaciones de Euler-Lagrange y el Principio del Mínimo de Pontryagin, y luego hallar dichas órbitas usando métodos de transcripción directa para convertir el problema en un problema de Programación No Lineal. Tras esto, se añaden las perturbaciones del viento solar, y múltiples estrategias de guiado basadas en el Regulador Cuadrático Lineal y el Control Predictivo por Modelo se desarrollan, simulan y comparan, obteniendo resultados satisfactorios.

Palabras clave

Velas Solares Eléctricas, Misiones de Rendezvous, Planificación Óptima, Estrategias de Guiado, Programación No Lineal, Regulador Cuadrático Lineal, Control Predictivo por Modelo.

Conclusiones

Se ha implementado un código para la planificación mediante Programación No Lineal órbitas óptimas para misiones de rendezvous tanto a Marte como a Júpiter, además de realizar un estudio paramétrico de los tiempos de vuelo. Para misiones a Marte, se han comparado las soluciones con las obtenidas mediante métodos indirectos y con valores de la literatura, verificando la proximidad de los resultados. Tras esto, se ha comparado el rendimiento de las tres estrategias de guiado empleadas una vez introducidas las perturbaciones solares. Las estrategias basadas en el Regulador Cuadrático Lineal y el Control Predictivo por Modelo de Horizonte Decreciente consiguen llegar al destino en el tiempo planificado, aunque la misión no siempre resulta exitosa, poseyendo tasas de fallo significantes. Por el contrario, el Control Predictivo por Modelo de Horizonte Deslizante resulta ser asintóticamente estable, lo que asegura el éxito de la misión siempre que se defina una función coste adecuada. En esta última estrategia el tiempo de vuelo puede ser superior al planificado, aunque se verifica que el incremento es escaso. Se concluye que, dado que una característica imperante en las estrategias de guiado de misiones aeroespaciales es la fiabilidad, el mejor algoritmo de guiado resulta ser el Control Predictivo por Modelo de Horizonte Deslizante.

Abstract

Electric Solar Wind Sails are a new type of spacecraft propellantless propulsion system that gathers its energy from solar wind protons and is potentially useful for interplanetary missions. With an appropriate thrust model, which can be obtained from the literature, one can study optimal orbits for interplanetary flights. The first goal of this project is to study the properties of time-optimal orbits for missions to Mars and Jupiter using an indirect approach by applying Euler-Lagrange equations and Pontryagin's Minimum Principle, and then compute them with direct transcription methods, converting the problem into Non Linear Programming form. Then, solar wind perturbations are added, and several guidance strategies based on Linear Quadratic Regulator Control and Model Predictive Control are developed, simulated and compared, yielding satisfactory results.

Contents

Resumen III
Abstract V

List of Figures IX
List of Tables XI
Notation XIII

1 Introduction **1**
1.1 Motivation 1
1.2 State of the art 3
1.3 Aim of the project 4
1.4 Structure 5

2 Basics of Orbital mechanics and Esails **7**
2.1 Equation of Motion 7
2.1.1 Derivation of the Equation of Motion 7
2.1.2 Validation of 2D-problem and circular planet motion hypotheses 8
2.1.3 Dynamic equations in polar coordinates 9
2.2 Esail continuous thrust 10
2.2.1 Thrust model 10
2.2.2 Practical limitations of the Esail 13
2.3 Solar wind uncertainty 14
2.3.1 High variability of solar wind 15
2.3.2 Modeling the solar dynamic pressure 15
2.4 Neglecting other forces 16

3 Optimal mission planning **19**
3.1 Optimal Control Problem formulation 19
3.1.1 Problem hypotheses 19
3.1.2 Defining our optimal control problem 19
3.2 Indirect approaches for OCPs 22
3.3 Direct approaches for OCPs 28
3.3.1 Transforming our OCP to a NLP problem. Direct Transcription 29
3.3.2 Strengthening arrival conditions and varying characteristic acceleration 32
3.3.3 Optimal transfer for Mars. Comparison with indirect methods 43
3.3.4 Parametric study of flight times 46

4 Guidance strategies considering solar wind uncertainties **49**
4.1 The effect of solar wind perturbations and stiffness of the problem 49
4.1.1 Different characteristic times between mission and control parameters. Saturation problem 49
4.1.2 Problem stiffness due to limited maneuvering capability 50

4.1.3 Setting a control margin 51
4.2 LQR control 52
4.2.1 Introduction to the Linear Quadratic Regulator 52
4.2.2 First strategy. Identity weighting matrices 56
4.2.3 Second strategy. Prioritizing thrust lever error 60
4.2.4 Third strategy. Prioritizing arrival position error 60
4.2.5 Limitations of LQR Control Strategy 62
4.3 Shrinking Horizon Model Predictive Control Strategy 63
4.3.1 New OCP formulation for Shrinking Horizon Strategy 63
4.3.2 Strategies under low solar wind conditions. Full thrust arcs 64
4.3.3 Strategies for trajectory determination in future time arcs 66
4.3.4 Shrinking Horizon MPC simulation results 68
4.3.5 Limitations of Shrinking Horizon MPC Strategy 72
4.4 Receding Horizon Model Predictive Control Strategy 72
4.4.1 New OCP formulation for Receding Horizon MPC Strategy 73
4.4.2 Cost function definition 74
4.4.3 Receding Horizon MPC Simulation results 76
4.4.4 Limitations of Receding Horizon MPC Strategy 79

5 Conclusions and future work 83

Appendix A Flowchart of developed MATLAB programs 85
A.1 Shrinking Horizon MPC Strategy 86
A.2 Receding Horizon MPC Strategy 87

Appendix B Esail additional mission simulations for different guidance strategies 89
B.1 LQR Control Strategy 90
B.2 Shrinking Horizon MPC Strategy 92
B.3 Receding Horizon MPC Strategy 94
Bibliography 97
Glossary 101

List of Figures

1.1 Paths followed by Voyager 1 and Voyager 2 space probes, showing gravity assist maneuvers 2
1.2 Real image of *LightSail 2* spacecraft before launch 3
1.3 Schematic functioning concept of the Esail. Credit: [1] 3
1.4 Depiction of *ESTCube-1* satellite in space, first Esail powered spacecraft 5

2.1 Gravitational attraction between two objects 8
2.2 Conceptual Esail thrust model illustration 12
2.3 Variation with respect to α_n of α (top) and γ (bottom) 12
2.4 Conceptual representation of thrust variation depending on sail pitch angle 13
2.5 Evolution with time of proton density and speed on solar wind. Data extracted from NASA 15
2.6 Probability density function of $p_\oplus$. Image taken from [2] and data extracted from NASA 16
2.7 Gamma distribution approximation of $p_\oplus$ (red line) compared with real data gathered from NASA (bars). Image taken from [3] 17

3.1 Representation of α_{n_1}, α_{n_2}, $\alpha_n^\star$ and its impact on the Hamiltonian 25
3.2 Saturation region of α_n in terms of λ_{v_r} and λ_{v_θ} 26
3.3 Visual representation of τ boundary in terms of λ_{v_r} and λ_{v_θ} 26
3.4 Visual representation of Direct Transcription of an Optimal Control Problem 31
3.5 Trajectory and evolution of variables in a transfer orbit to Jupiter ignoring arrival velocity constraints for $a_c = 0.36$ mm/s^2 34
3.6 Trajectory and evolution of variables in a transfer orbit to Jupiter considering zero arrival radial velocity for $a_c = 0.36$ mm/s^2 35
3.7 Trajectory and evolution of variables in a transfer orbit to Jupiter considering equal arrival velocity modulus for $a_c = 0.36$ mm/s^2 36
3.8 Trajectory and evolution of variables in a transfer orbit to Jupiter considering arrival rendezvous for $a_c = 0.36$ mm/s^2 37
3.9 Trajectory and evolution of variables in a transfer orbit to Jupiter considering arrival rendezvous for $a_c = 0.1$ mm/s^2 39
3.10 Trajectory and evolution of variables in a transfer orbit to Jupiter considering arrival rendezvous for $a_c = 1$ mm/s^2 40
3.11 Trajectory and evolution of variables in a transfer orbit to Mars considering arrival rendezvous for $a_c = 1$ mm/s^2 42
3.12 Trajectory and evolution of variables in a transfer orbit to Mars considering arrival rendezvous for $a_c = 0.36$ mm/s^2 44
3.13 Trajectory and evolution of variables comparison between direct and indirect methods in a transfer orbit to Mars considering arrival rendezvous for $a_c = 0.36$ mm/s^2 45
3.14 Parametric study of Esails flight time for different characteristic accelerations and final distances for circular-circular rendezvous 46
3.15 Zoomed version of the parametric study for higher values of characteristic acceleration 47

4.1 Probability of entering in a deviation arc as a function of control margin 53

4.2 Block diagram for the LQR closed loop control strategy 56
4.3 Histograms of arrival distance values for simulations to Jupiter (top) and Mars (bottom) with Finite Horizon LQR with unit diagonal weighting matrices 57
4.4 Trajectory and evolution of state and control variables in a successful mission to Jupiter using Finite Horizon LQR with unit diagonal weighting matrices 58
4.5 Trajectory and evolution of state and control variables in an unsuccessful mission to Jupiter using Finite Horizon LQR with unit diagonal weighting matrices 59
4.6 Histograms of arrival distance values for simulations to Jupiter (top) and Mars (bottom) with Finite Horizon LQR prioritizing thrust lever error in weighting matrices 61
4.7 Histograms of arrival distance values for simulations to Jupiter (top) and Mars (bottom) with Finite Horizon LQR prioritizing final conditions errors in weighting matrices 62
4.8 Histograms of arrival distance values for simulations to Mars with SHMPC using maximum thrust cone angle (top), maximum radial thrust (middle) and maximum tangential thrust (bottom) 67
4.9 Histograms of arrival distance values for simulations to Mars with SHMPC using different strategies for κ^{max}, from top to bottom: *Nominal*, *Mean*, *Current*, *Linear* 69
4.10 Trajectory and evolution of state and control variables in a successful mission to Mars using optimal Shrinking Horizon MPC 70
4.11 Trajectory and evolution of state and control variables in a successful mission to Jupiter using optimal Shrinking Horizon MPC 71
4.12 Trajectory oscillations due to cost function evaluating distance between points 74
4.13 Contour representation of the three different cost functions considered 75
4.14 Histograms of mission flight time to Mars with RHMPC using different time-depending weights 78
4.15 Trajectory and evolution of state and control variables in a mission To Mars using optimal Receding Horizon MPC 80
4.16 Trajectory and evolution of state and control variables in a mission To Jupiter using optimal Receding Horizon MPC 81

A.1 Flowchart for Shrinking Horizon MPC Strategy MATLAB program 86
A.2 Flowchart for Receding Horizon MPC Strategy MATLAB program 87

B.1 Trajectory and evolution of state and control variables in a successful mission to Mars using Finite Horizon LQR with unit diagonal weighting matrices 90
B.2 Trajectory and evolution of state and control variables in a failed mission to Mars using Finite Horizon LQR with unit diagonal weighting matrices 91
B.3 Trajectory and evolution of state and control variables in a failed mission to Mars using optimal Shrinking Horizon MPC 92
B.4 Trajectory and evolution of state and control variables in a failed mission to Jupiter using optimal Shrinking Horizon MPC 93
B.5 Trajectory and evolution of state and control variables in a prolonged mission to Mars using Receding Horizon MPC 94
B.6 Trajectory and evolution of state and control variables in a prolonged mission to Jupiter using Receding Horizon MPC 95

List of Tables

2.1	Real planet orbit inclinations with respect to the Ecliptic plane	8
2.2	Real planet orbit eccentricities	9
2.3	Statistical properties differences between real NASA gathered data and Gamma PDF approximation	16
2.4	Standard Gravitational Parameters of planets of the Solar System and the Sun and radii of spheres of influence	17
3.1	Classic Runge Kutta scheme	30
3.2	Flight time comparison for a rendezvous mission to Mars with $a_c = 1$ mm/s^2	41
4.1	Performance of Finite Horizon LQR for Jupiter and Mars with unit diagonal weighting matrices. The value $\overline{d}$ denotes the arrival distance to the planet and σ_d its standard deviation	57
4.2	Performance of Finite Horizon LQR for Jupiter and Mars prioritizing thrust lever error in weighting matrices. The value $\overline{d}$ denotes the arrival distance to the planet and σ_d its standard deviation	60
4.3	Performance of Finite Horizon LQR for Jupiter and Mars prioritizing final conditions errors in weighting matrices. The value $\overline{d}$ denotes the arrival distance to the planet and σ_d its standard deviation	61
4.4	Performance of different LQR Control Strategies grouped by planet. The value $\overline{d}$ denotes the arrival distance to the planet and σ_d its standard deviation	62
4.5	Performance comparison for Shrinking Horizon MPC for various *full thrust arc* strategies. The value $\overline{d}$ denotes the arrival distance to the planet and σ_d its standard deviation	66
4.6	Performance comparison for Shrinking Horizon MPC for different κ^{max} for future intervals. The value $\overline{d}$ denotes the arrival distance to the planet and σ_d its standard deviation. The value $\overline{d}$ denotes the arrival distance to the planet and σ_d its standard deviation	68
4.7	Performance final results for missions to Mars and Jupiter with an optimal Shrinking Horizon MPC Strategy. The value $\overline{d}$ denotes the arrival distance to the planet and σ_d its standard deviation	68
4.8	Performance comparison between LQR Control and SHMPC Strategies. The value $\overline{d}$ denotes the arrival distance to the planet and σ_d its standard deviation	68
4.9	Performance comparison for Receding Horizon MPC for Mars missions using J_3 and different time-depending weightings	77
4.10	Performance comparison for Receding Horizon MPC for Jupiter missions using J_3 and different weightings	78

Notation

$\boldsymbol{A}$	Linearized state matrix in LQR control
$\boldsymbol{a}$	Esail acceleration vector
a	Esail acceleration modulus
a_c	Esail characteristic acceleration
a_r	Esail acceleration in radial direction
a_θ	Esail acceleration in tangential direction
$\boldsymbol{B}$	Linearized control matrix in LQR control
$\boldsymbol{c}$	Vector of constraints in NLP formulation
$\boldsymbol{f}$	Set of state equations in OCP formulation
$\boldsymbol{g}$	Set of boundary conditions in OCP formulation
H	Hamiltonian of the system
$\tilde{H}$	Hamiltonian term proportional to thrust lever
$\boldsymbol{h}$	Set of path constraints in OCP formulation
J	Cost function
$\boldsymbol{K}$	Gain matrix in LQR control
$\overline{k}$	Mean value of variable k
N	Number of time segments in NLP formulation
N_ξ	Number of time segments per arc in MPC Strategy
n_ξ	Number of recalculation arcs in MPC Strategy
$p_\oplus$	Solar wind dynamic pressure at 1 AU distance from the Sun
$\boldsymbol{Q}$	Weighting matrix for state variables in LQR control
$\boldsymbol{Q}_{end}$	Weighting matrix for final conditions in LQR control
$\boldsymbol{R}$	Weighting matrix for control parameters in LQR control
r	Distance from the Sun
r_i	Planet's orbit mean radius, where $i = \{\oplus, \sigma, \jmath\}$
r_{SOI}	Sphere of influence radius
t	Time
t_f	Arrival time
$\boldsymbol{u}$	Set of the system's control parameters $\{\tau, \alpha_n\}$ or $\{\kappa, \alpha_n\}$
V_0	Tether grid voltage
v_r	Radial velocity
v_θ	Tangential velocity
w_i	Time dependent weighting function number i in MPC
$\boldsymbol{x}$	Set of the system's state variables $\{r, \theta, v_r, v_\theta\}$
x_{nom}	Value of x referred to the nominal orbit, where $x = \{r, \theta, v_r, v_\theta\}$
$\boldsymbol{y}$	Vector of variables in NLP formulation
α	Thrust cone angle
α_n	Sail pitch angle
γ	Thrust nondimensional parameter in thrust model. Flight path angle in MPC
Δt	Time step size in NLP formulation

δx	Error in variable i with respect to nominal in LQR control, where $x = \{r, \theta, v_r, v_\theta\}$
ε	Position error measuring function in Receding Horizon MPC
η	Current time segment in NLP formulation
θ	True anomaly
θ_i	True anomaly of the planet i, where $i = \{\oplus, \sigma, \jupiter\}$
κ	Esail acceleration parameter
κ^{max}	Maximum value of kappa
λ_i	Corresponding adjoint variable, where $i = \{r, \theta, v_r, v_\theta\}$
μ_i	Standard Gravitational Parameter of body i (when omitted, referred to the Sun)
ξ	Current recalculation arc in MPC Strategy
σ_i	Standard deviation of variable i
τ	Thrust lever parameter
φ	Mayer term of the cost function
$\mathscr{L}$	Lagrange term of the cost function
$\mercury$	Mercury
$\venus$	Venus
$\oplus$	Earth
σ	Mars
$\jupiter$	Jupiter
$\saturn$	Saturn
$\uranus$	Uranus
Ψ	Neptune
$\odot$	Sun

1 Introduction

Exploration is in our nature. We began as wanderers, and we are wanderers still. We have lingered long enough on the shores of the cosmic ocean. We are ready at last to set sail for the stars.

Carl Sagan, 1980

The sky has been a subject matter for thousands of years. Since the ancient civilizations, humans have studied the celestial bodies above their heads and tried to predict their orbits. Centuries of investigation let us realize not only that the Earth is not the center of the Universe, but neither the Sun, nor the Milky Way. Having that in mind, and given our intrinsic curiosity, nobody doubted that we would start studying objects further and further away. But there is one big inconvenience, the vast size of the Universe.

1.1 Motivation

The closest system to our Sun is "Alpha Centauri", with "Proxima Centauri" as its center star, which is 4.25 light-years away from the Earth. That means that light takes 4.25 years to travel the distance between "Proxima Centauri" and our planet. To put that in context, the highest speed that a human-made object has achieved is 530,000 km/h, or 0.05% the speed of light, and it was accomplished by NASA's "Parker Solar Probe", by flying really close to the Sun with a high eccentricity orbit. Even if we could escape the Solar System with that velocity, we would have to wait 8,500 years for the spacecraft to reach "Proxima Centauri", ignoring relativistic effects.

So, as of today, interstellar travel is little more than a dream, and we should focus on what we can reach: targets inside our Solar System.

There have been numerous spatial missions in the realms of our Solar System. We have visited all the eight planets and various of their moons, including other celestial bodies such as dwarf planets and asteroids. Some planets have been visited more than once, for example Jupiter, which has had 7 fly-by or related missions: "Pioneer 10" (1973), "Pioneer 11" (1974), "Voyager 2" (1979), "Voyager 1" (1979), "Galileo" (1995-2003), "New Horizons" (2007) and Juno (2016-today). Other planets have been explored just once, like Uranus and Neptune, that were only visited by "Voyager 2" (1986 and 1989 respectively).

Many of those missions were accomplished with the aid of gravity assist maneuvers, because otherwise travel times would get exaggeratedly high, given our current impulsive propulsion technology. But the problem with these maneuvers is that we have to wait for the planets to align in a certain way, and time necessary for these configurations to repeat can get really high if more than two planets are involved. Voyager 2 is an example of this, flights by Jupiter, Saturn and Uranus allowed it to obtain the necessary speed to reach Neptune and even to achieve the Solar System escape velocity, but this four-planet configuration only repeats approximately every 175 years [4]. In figure 1.1 a picture of the trajectory that followed Voyager 1 and Voyager 2 as part of the mission *Voyager* is shown. Many gravity assist maneuvers were made in order to

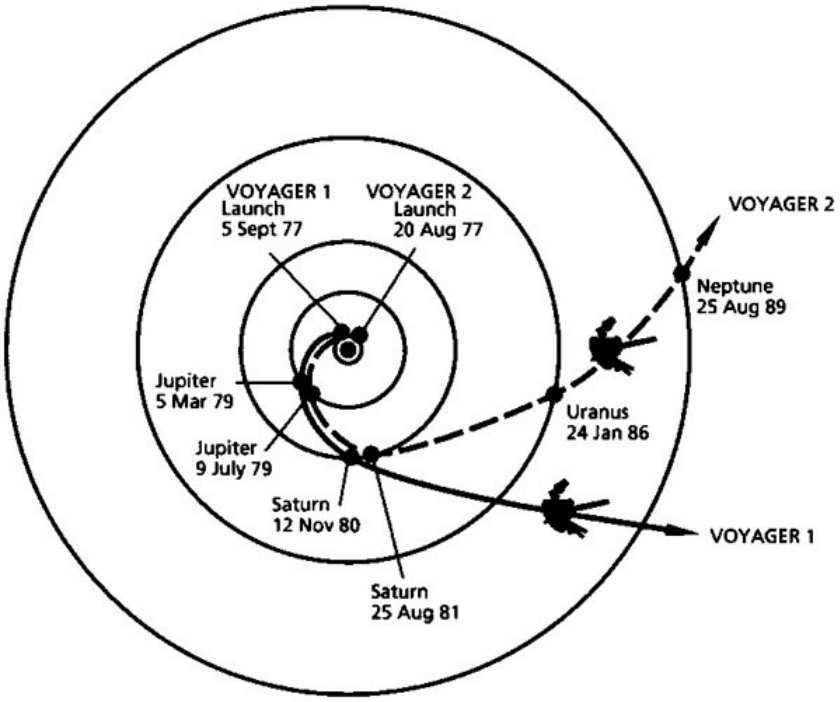

Figure 1.1 Paths followed by Voyager 1 and Voyager 2 space probes, showing gravity assist maneuvers.

reach those deep regions of the outer solar system space.

The recent advancements in Low-Thrust Continuous Propulsion systems such as Ion Thrusters present a viable solution to reach high velocities without the aid of gravity assists maneuvers, by accelerating the spacecraft for a longer period of time. However, its usage for interplanetary missions is limited, since the total amount of propellant that needs to be consumed limits its applicability.

That is where Low-Thrust Propellantless Continuous Propulsion systems come in, as an alternative to reach far away objects without depending on gravity assist maneuvers. The idea is to use the Sun as the main source of energy, taking advantage of the solar wind that reaches the spacecraft. Different concepts have been studied to exploit this solar wind radiation, examples are Photonic, Magnetic and Electric Solar Wind Sails.

This is not the only incentive for Solar Wind Sails. There is another common problem in classical space maneuvers: mass. Thrust is usually generated using Newton's Third Law, so propellant needs to be expelled at high speed each time a maneuver has to be made. This propellant is finite, so space missions that require periodic maneuvers have an intrinsic operational time span: until all the propellant is consumed. This is the example of the new *James Webb Space Telescope* (JWST), which will operate in the next 10 years, until all its propellant is consumed and it can no longer maintain the HALO orbit around the second Lagrange point (L2) of the system Sun-Earth. If we are able to accomplish these missions with Solar Wind Sails, mass consumption will not be required, and missions like James Webb could theoretically last longer.

The most studied and earliest formulated concept is the Photonic Solar Wind Sail, also simply known as Solar Sail; it works similar to a sailing boat, hence its name. The idea is to deploy a big reflective surface around the spacecraft to reflect photons from the solar wind. By the laws of conservation of momentum and energy, a resultant force (not necessarily perpendicular to the surface) is exerted, and so the orbit can be modified. One example of this technology is *LightSail 2* (figure 1.2), a Photonic Solar Wind Sail spacecraft that is currently orbiting the Earth and changing its orbit exclusively with Sun energy [5].

Magnetic and Electric Sails work similarly, by slowing down the protons of the solar wind with magnetic or electric fields respectively, and transferring their energy to the spacecraft as thrust. The reasons of their late development compared to the Photonic Sails is due to practical limitations, even though they present

Figure 1.2 Real image of *LightSail 2* spacecraft before launch.

interesting advantages too, specially the latter. These differences are presented in the next Chapter 1.2.

This project focuses its attention on Electric Solar Wind Sails since recent investigations present them as a feasible solution with a bright future.

1.2 State of the art

The concept of an Electric Solar Wind Sail (Esail) was first invented in 2004 by the Finnish space physicist, astrobiologist and inventor Pekka Janhunen. At that time, Photonic Solar Sails were being deeply studied, and Dr. Janhunen considered the possibility of designing a system that repelled protons instead of photons by using an electric field, obtaining some raw calculations that proved its feasibility [6].

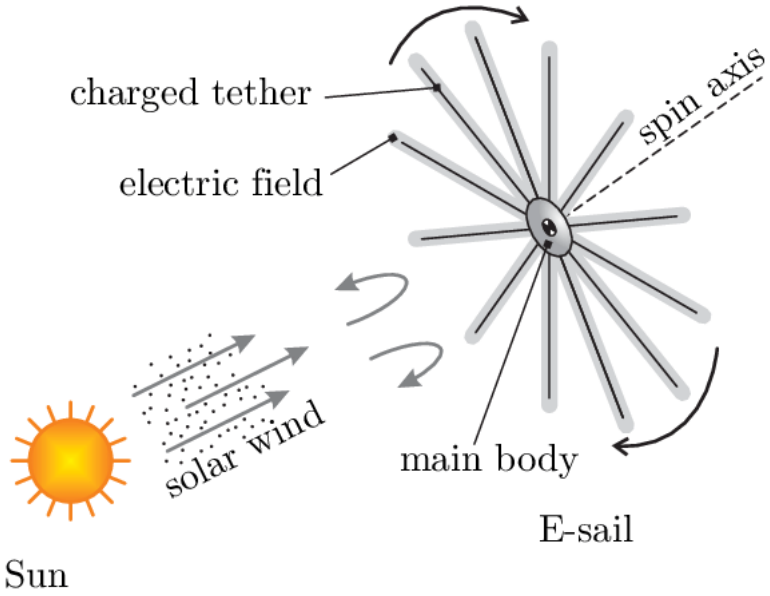

Figure 1.3 Schematic functioning concept of the Esail. Credit: [1].

The reason protons were not tackled before is because, at 1 Astronomical Units (AU) distance, the distance from the Sun to the Earth, the effect of solar dynamic pressure (exerted by protons, about 2 nPa) is approximately 5,000 times weaker than the solar radiation pressure (exerted by photons, about 9 μPa), so the thrust that can be generated for equal frontal areas is substantially lower. But there is a way to tackle this problem, and that is by obtaining greater surface areas with the electric solar wind sails, compared to the photonic ones. If we construct a mesh of wires with a separation distance comparable to the Debye length of the plasma[1], charged with a high positive electric potential, protons will see that mesh as an impenetrable surface. That makes greater surface areas with lower weights possible, and, even though resulting forces between these two type of Solar Wind Sails are not comparable, accelerations are.

There is also a key difference between the photonic and the electric solar wind sails. As different studies suggest, thrust produced by a Photonic Solar Wind Sail is proportional to the inverse of the distance r from the Sun squared [7]. In contrast, the thrust produced by an Esail decays with r, not with r^2 [8]. That makes Esails feasible for missions to distant planets such as Neptune in a reasonable time, without needing to use gravity assist maneuvers.

Magnetic Solar Wind Sails are also promising, because greater surface areas can be created with even lower mass, surpassing Esails, but superconductors are needed, and as of today more work has to be done on that subject to make that kind of mission feasible. That is why our attention is focused on Esails [9].

Several papers of the Esail concept have been published in various scientific journals, most of them elaborated partly by Dr. Janhunen himself, in collaboration with other scientists. Originally, the prototypical grid was squared, with an electron gun on its side to expel the electrons that are absorbed by the structure because of the positive electric potential.

Last tendencies, in contrast, lean towards a circular shape instead. The payload now rests in the center, and really long (order of km) and thin positively charged tethers extend radially from it [10]. By inducing a rotation in the spacecraft, wires are maintained stretched, as a result of the centrifugal force. Auxiliary tethers are also used, connecting the farthest ends of the main radial tethers, so the stability of the structure is preserved while rotating. Remote units appear to be useful too, as they can store the auxiliary tethers before deployment and can also initiate (and control if needed) the rotation of the spacecraft [11].

Many papers of the matter have been published in the last years. The principal interest is centered around Esail performance, characterization of its thrust and control of its spin plane, along with possible mission applications. It has been suggested that Esails could potentially be more useful than regular photonic solar sails near most stars [12]. The Estonian *ESTCube-1* satellite (figure 1.4) was launched in 2013 and inserted in LEO (Low Earth Orbit), and its primary missions were to test the tether deployment mechanism (which did not go as expected) and characterize on-board electron guns [13]. After one year of studying its behaviour, it reentered Earth. NASA has also studied this concept with its *HERTS* project (Heliopause Electrostatic Rapid Transit System) [14]. Furthermore, there are also initiatives to make manned Mars missions feasible and affordable by reducing propellant use [15], as well as missions to near-Earth asteroids to return samples [16]. Possible applications for Outer Solar System Exploration have also been considered [17], as well as a fleet of nanospacecrafts equipped with Esails for touring multiple asteroids [18]. A preliminar overview of possible applications can be consulted in [19].

1.3 Aim of the project

As it was previously stated, thrust in Esails decays as 1/r (on average, and assuming constant voltage in tethers), which makes it an interesting alternative to travel to distant planets. The resulting path of that mission is some kind of outward spiral, and a control strategy can be applied to maintain an specific orbit law, for example, finding a minimal-time transfer orbit. The aim of this project is then not to study the physical mechanisms that make the Esail produce thrust, nor to understand its attitude behaviour, but to control thrust appropriately to perform missions of interest, taking into account solar wind variability. We can divide the objectives in two general categories.

[1] Effective length in which solar wind plasma tends to shield the Esail electric field

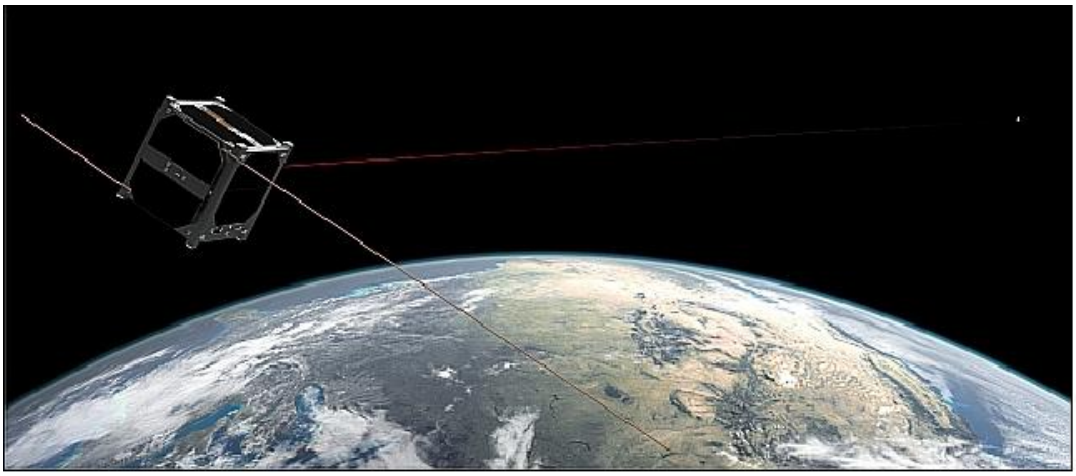

Figure 1.4 Depiction of *ESTCube-1* satellite in space, first Esail powered spacecraft.

- **Optimal Mission Planning**. First, we present an appropriate thrust model for the Esail, in term of thrust lever and pitch angle. We then solve the optimal control problem that arises using a direct transcription method to obtain time-optimal orbits for transfers to Mars and Jupiter.
- **Optimal Guidance and Uncertainty Mitigation**. Solar wind perturbations are now introduced. The goal is to come up with a guidance strategy that is able to mitigate those perturbations and track the optimal path previously obtained.

We center our focus on missions including solar wind uncertainty because it is observed that not too many investigations tackle this problem. Nominal solar wind is often assumed ([20] and [17] among others) and few reports that include closed-loop control strategies due to solar wind variability can be found ([2] and [3]).

In this project, we treat the attitude problem as a given. Many investigations are being developed in regards to spin plane control. Voltage modulation (different voltage along the main tethers) is typically used for this purpose of modifying the spacecraft's attitude [21]. Since we tackle this matter as a black box, it is supposed that we are able to achieve the attitude desired instantaneously at any time.

Some basic hypotheses are considered in the realms of this project:

- Planets move in circular motion.
- All planet orbits are contained in the ecliptic plane. Hence, the 2D simplification is assumed.
- Only the gravitational attraction of the Sun is considered. Gravitational effects of other planets are neglected.

These simplifications are further detailed on Chapters 2.1.2 and 2.4.

1.4 Structure

The structure of the project is defined as follows:

Chapter 1: This chapter serves as an introduction for the reader to Electric Solar Wind Sails. Motivation, State of the Art and Aim of the project sections are included, to define the scope of this project, present the current progress and technology, indicate the corresponding hypotheses and emphasize key important aspects.

Chapter 2: Here, a basic overview of the problem is presented. It starts by demonstrating basic equations in orbital mechanics. Then, an appropriate thrust model for Esails is included, as well as its limitations. Lastly, solar wind perturbations are introduced, as well as a statistical model to approximate them.

Chapter 3: This chapter starts by formulating the nominal Optimal Control Problem, without solar wind perturbations. Next, indirect approaches are presented to learn about the aspects of the optimal solution. After that, the problem is solved using direct transcription methods and using NLP algorithms for various missions. Additionally, a particular mission to Mars is solved using indirect methods to compare the results of both approaches.

Chapter 4: In this chapter, solar wind perturbations are presented, as well as their impact on Esail orbits. Then, several guidance strategies to mitigate those perturbations are presented. The first uses a Linear Quadratic Regulator to follow the nominal orbit. The second and third use Model Predictive Control formulations with orbit updating, using a shrinking and receding horizon respectively. Then, results are compared.

Chapter 5: Several conclusions are extracted from all the data and knowledge gathered. Moreover, a list of improvements that could potentially enhance our solutions or prepare the problem for other scenarios is also included and proposed as future work.

2 Basics of Orbital mechanics and Esails

In this chapter, we take a look to the basics of orbital mechanics. The equation of motion is introduced and adapted to our case of continuous thrust, introducing then a simple model to estimate the thrust produced by the Esail. Later, solar perturbations are characterised, and the neglect of other weaker forces is explained.

2.1 Equation of Motion

2.1.1 Derivation of the Equation of Motion

For the discovery of the equation of motion, we have to date back to 1687, when Sir Isaac Newton (1642-1727) published his *Philosophiæ Naturalis Principia Mathematica*. In that book, he included a law for gravitational force that was deducted empirically, known today as Newton's Law of Universal Gravitation. That law states that the gravitational force exerted by two massive bodies is directly proportional to the product of the masses and inversely proportional to the distance between their centers of mass squared. Its direction is the line that connects both centers of mass, in the sense of attraction. The equations for both of the bodies are:

$$\begin{aligned} \boldsymbol{F}_{12} &= G\frac{m_1 m_2}{r^2}\frac{\boldsymbol{R_2}-\boldsymbol{R_1}}{|\boldsymbol{R_2}-\boldsymbol{R_1}|} \\ \boldsymbol{F}_{21} &= G\frac{m_1 m_2}{r^2}\frac{\boldsymbol{R_1}-\boldsymbol{R_2}}{|\boldsymbol{R_1}-\boldsymbol{R_2}|} \end{aligned} \tag{2.1}$$

where G is the Universal Gravitational Constant, $G \approx 6.674 \cdot 10^{-11} m^3 kg^{-1} s^{-2}$; F_{ij} is the force felt in the body i exerted by the body j and $\boldsymbol{R_1}$, $\boldsymbol{R_2}$ are the position vectors of each body given an inertial frame of reference. Vector $\boldsymbol{r}$ points from mass 1 to mass 2:

$$\boldsymbol{r} = \boldsymbol{R_2} - \boldsymbol{R_1}, \qquad r = |\boldsymbol{r}| \tag{2.2}$$

We can now introduce Newton's Second Law

$$\begin{aligned} m_1 \ddot{\boldsymbol{R}}_{\boldsymbol{1}} &= \boldsymbol{F}_{12} = G\frac{m_1 m_2}{r^2}\frac{\boldsymbol{r}}{r} \\ m_2 \ddot{\boldsymbol{R}}_{\boldsymbol{2}} &= \boldsymbol{F}_{21} = -G\frac{m_1 m_2}{r^2}\frac{\boldsymbol{r}}{r} \end{aligned} \tag{2.3}$$

and dividing by m_1 and m_2 in first and second equation respectively

$$\begin{aligned} \ddot{\boldsymbol{R}}_{\boldsymbol{1}} &= G\frac{m_2}{r^2}\frac{\boldsymbol{r}}{r} \\ \ddot{\boldsymbol{R}}_{\boldsymbol{2}} &= -G\frac{m_1}{r^2}\frac{\boldsymbol{r}}{r} \end{aligned} \tag{2.4}$$

And recalling the definition of $\boldsymbol{r}$ in (2.2)

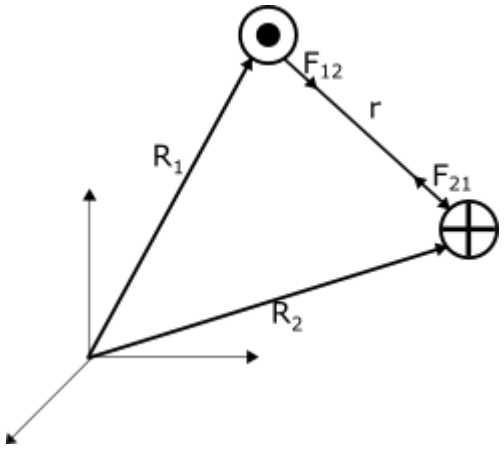

Figure 2.1 Gravitational attraction between two objects.

$$\ddot{\boldsymbol{R}}_{\boldsymbol{2}} - \ddot{\boldsymbol{R}}_{\boldsymbol{1}} = \ddot{\boldsymbol{r}} = -G\frac{m_1 + m_2}{r^2}\frac{\boldsymbol{r}}{r} \tag{2.5}$$

This equation has an analytic solution (not the case if more than 2 bodies with mass are involved). The center of gravity of both bodies always moves with constant velocity, and so for convenience we define our inertial frame of reference to be the one in which the center of mass of the system stays still. From that point of view, both of the bodies are "orbiting" this fixed point.

Given our specific scenario, some hypotheses that simplify the problem can be made. If one of the bodies has a significantly higher mass than the other ($m_1 \gg m_2$), then the center of mass of the system is really close to the center of mass of that massive body, and so it can be assumed that they coincide (it is equivalent to saying that the massive body does not move in comparison to the lighter one). Given this simplification, $\boldsymbol{R_1}$ is constant and the equation of motion for the second mass is now:

$$\ddot{\boldsymbol{r}} = -\frac{\mu}{r^2}\frac{\boldsymbol{r}}{r} \tag{2.6}$$

where $\mu = G \cdot m_1$, since $m_1 \gg m_2$ implies that $m_1 + m_2 \approx m_1$. The parameter μ is usually called the Standard Gravitational Parameter, widely used in orbital mechanics.

2.1.2 Validation of 2D-problem and circular planet motion hypotheses

For this project, it is assumed that all planets orbit in the same plane, the Ecliptic, which is defined as the plane that contains the orbit of the Earth. This can be supported by analysing the inclination of the real orbits of the planets with respect to this Ecliptic plane, which are presented in table 2.1.

Table 2.1 Real planet orbit inclinations with respect to the Ecliptic plane.

Planet	☿	♀	⊕	♂	⚳	♃	♄	♅	♆
i (º)	7.01	3.39	0	1.85	1.31	2.49	0.77	1.77

Because of the small inclination values, specially in the case of Mars and Jupiter (which become relevant later), we can, as an initial approximation, suppose the orbits to be co-planar, and hence reduce the problem to two dimensions. This simplification is primarily made to simplify the set of dynamic equations and reduce the computational complexity of the problem.

It is also assumed as stated before that the planet orbits are circular. This hypothesis can be supported by looking at the table 2.2, which show the eccentricity of the eight planet orbits.

To put these numbers in perspective, an eccentricity of 0.1 represents a 10% difference between the farthest point of the orbit (apoapsis) and the semi-major axis. Mercury's eccentricity value differs significantly from the rest, and can not be considered small, however, this does not affect us, since we center our attention on

Table 2.2 Real planet orbit eccentricities.

Planet	☿	♀	⊕	♂	♃	♄	♅	♆
e	0.2056	0.0068	0.0167	0.0934	0.0484	0.0541	0.0472	0.0086

Mars and Jupiter. Thus, this simplification is reasonable in first approximation.

These two hypotheses ease the departure date calculation, which depends now only on the synodic period between the planets that are going to intervene in the transfer. For example, if the transfer is between the Earth and Jupiter, each phase configurations repeats roughly each 400 days, calculation obtained from

$$T_{syn} = \frac{1}{\frac{1}{T_{\oplus}} - \frac{1}{T_{♃}}} = 398.9 \text{ days} \tag{2.7}$$

Another assumed hypothesis is that departure can be chosen as will, which implies that the desired phase angle between the Earth and the arrival planet is free to choose; it depends only on the results of the time-optimal orbit calculation, and then a suitable departure date is chosen to encounter the planet when we reach its orbit.

2.1.3 Dynamic equations in polar coordinates

Since our problem is assumed to be two-dimensional, and planets' motion to be circular, it is reasonable to use polar coordinates to write the dynamic equations of the system.

We first derive these equations ignoring thrust produced by the Esail, in other words, only by the effects of the Sun's gravitational force. Since (2.6) involves a second order derivative of the position, and position is defined by two independent variables (2D problem), we seek for four first order differential equations; two for position and two for velocity.

The first step to obtain these equations is to differentiate the position vector $\boldsymbol{r} = r\boldsymbol{u_r}$ with respect to time in polar coordinates, to obtain the radial and tangential accelerations as follows:

$$\begin{aligned} \dot{\boldsymbol{r}} &= \frac{\mathrm{d}\boldsymbol{r}}{\mathrm{d}t} = \frac{\mathrm{d}\left(r\boldsymbol{u_r}\right)}{\mathrm{d}t} = \dot{r}\boldsymbol{u_r} + r\dot{\theta}\boldsymbol{u_\theta} \\ \ddot{\boldsymbol{r}} &= \frac{\mathrm{d}\dot{\boldsymbol{r}}}{\mathrm{d}t} = \frac{\mathrm{d}\left(\dot{r}\boldsymbol{u_r} + r\dot{\theta}\boldsymbol{u_\theta}\right)}{\mathrm{d}t} = \left(\ddot{r} - r\dot{\theta}^2\right)\boldsymbol{u_r} + \left(2\dot{r}\dot{\theta} + r\ddot{\theta}\right)\boldsymbol{u_\theta} \end{aligned} \tag{2.8}$$

We now combine (2.6) and (2.8) to obtain equations for both radial and tangential acceleration. Since gravitational force is radial, the tangential component of acceleration in (2.8) is equal to 0.

$$\begin{aligned} \ddot{r} - r\dot{\theta}^2 &= -\frac{\mu}{r^2} \\ 2\dot{r}\dot{\theta} + r\ddot{\theta} &= 0 \end{aligned} \tag{2.9}$$

Note that the spacecraft mass does not appear in these equations. The parameter $\mu = \mu_{\odot}$ is known the Standard Gravitational Parameter of the Sun. We now introduce tangential and radial velocities

$$\begin{aligned} v_r &= \dot{r} \\ v_\theta &= r\dot{\theta} \end{aligned} \tag{2.10}$$

Introducing those velocities in (2.9), we can obtain

$$\begin{aligned} \dot{r} &= v_r \\ \dot{\theta} &= \frac{v_\theta}{r} \\ \dot{v_r} &= \frac{v_\theta^2}{r} - \frac{\mu}{r^2} \\ \dot{v_\theta} &= -\frac{v_r v_\theta}{r} \end{aligned} \tag{2.11}$$

Consequently, it is clear that the state variables of our problem are $\{r, \theta, v_r, v_\theta\}$. Given the values $\{r(t_0), \theta(t_0), v_r(t_0), v_\theta(t_0)\}$ at an instant t_0, we can compute the orbit that the spacecraft follows. If the spacecraft is only affected by Sun attraction, the motion it describes is called a *Keplerian arc*. There are several coordinates systems one can use for this type of problems, Keplerian Orbital Elements are extensively used, for example; given that we know the plane of motion, we can define the state of the spacecraft by using the set of parameters $\{a, e, \omega, \nu\}$. With this set of parameters, the only variable that changes with time is ν, following the equations of motion, one can calculate ν given the time since the body last crossed the periapsis. Therefore, given $\{a, e, \omega, \nu(t_0)\}$, we can also compute the trajectory of the spacecraft. Keplerian elements ω and ν depend on the frame of reference. If we set $\omega = 0$ (the periapsis of the orbit coincides with $\theta = 0$), then $\nu = \theta$. Keplerian elements a and e can be expressed in terms of position and velocity as

$$\begin{aligned} e &= \left| \frac{\boldsymbol{v} \times (\boldsymbol{r} \times \boldsymbol{v})}{\mu} - \frac{\boldsymbol{r}}{r} \right| \\ a &= \frac{r(1 + e\cos\theta)}{1 - e^2} \end{aligned} \tag{2.12}$$

However, it is easier to express Esail thrust in terms of polar coordinates rather than in keplerian orbital elementes, as is seen in Chapter 2.2, hence our use of them. When 3D problems are approached, other coordinates systems like Modified Equinoctial Orbital Elements (MEOEs) [22], designed to avoid singularities, are often used ([20] and [23]).

2.2 Esail continuous thrust

In this section a simple and recent model for the continuous thrust produced by the Esail is presented, as well as typical ranges of values of the parameters involved.

2.2.1 Thrust model

The task of modeling thrust force produced by the Esail in a simple manner handleable for complex optimization algorithms has already been deeply studied.

Initially, perpendicular solar wind (achieved by aiming the spacecraft exactly towards the Sun) was the only studied case, in which thrust, by symmetry, points towards the radial direction. This assumption was made because the simulations conducted on a charged wire were originally only applicable to that configuration [24]. With that restriction, not all orbits are feasible, and possible solutions are studied in [25]. In fact, to travel from one orbit to another, we have to be able to change the angular momentum of the spacecraft. That is, change the angular momentum of the osculating orbit, and that is not possible with radial thrust; a perpendicular component is needed.

For that reason, an extension including a pitch angle was proposed. The first approximations assumed that the pitch angle did not affect thrust modulus, and that the direction of it coincides with the perpendicular vector to the surface of the Esail [26]. The equations of radial and tangential thrust were then given by

$$\begin{aligned} T_r &= T\cos\alpha \\ T_\theta &= T\sin\alpha \end{aligned} \tag{2.13}$$

where T is the thrust modulus and α is the angle formed between the Esail thrust vector $\boldsymbol{a}$ and the position vector $\boldsymbol{r}$, also known as thrust cone angle. A visual representation can be seen in figure 2.2, although α should be equal to α_n and $\boldsymbol{r}$ should go in the direction of $\boldsymbol{u_n}$. The dependence of thrust modulus with respect to the distance to the Sun was estimated by analyzing the evolution of the electrons temperature and density with that distance. It was estimated that the velocity of the solar wind particles remained constant, and that electron density decayed with r^{-2}, and electron temperature with $r^{-1/3}$. With those assumptions, one can estimate that the thrust modulus decays with $r^{-7/6}$. That approximation allow us to characterize the thrust by measuring it from Earth (at 1AU from the Sun) at maximum voltage. The acceleration produced (thrust divided by spacecraft mass) is usually named $a_\oplus$.

It is also common practice to think of the acceleration produced by the Esail thrust (vector denoted as $\boldsymbol{a}$), rather than thrust itself. It is convenient because, normally, the motion is expressed in equations that involve accelerations, not forces, as can be seen and was remarked in (2.11).

Furthermore, typically the Esail acceleration is expressed in terms of the maximum acceleration at 1AU distance from the Sun, usually denoted a_c, accompanied with a power parameter named τ. This power parameter is often supposed binary, resulting in sections that consist of keplerian arcs and others that are traveled at the highest acceleration possible. There is a reason to assume this discontinuity, and it is explained in Chapter 3.2, but still, it is not mandatory, since thrust depends on the voltage of the tethers, and that can be set to any value between the operating range.

With those three notions, we obtain the expression of the initial Esail thrust model, shown in (2.14), which determines that our control parameters are τ and α.

$$\begin{aligned} a_r &= a_c \tau \cos\alpha \left(\frac{r_\oplus}{r}\right)^{7/6} \\ a_\theta &= a_c \tau \sin\alpha \left(\frac{r_\oplus}{r}\right)^{7/6} \end{aligned} \tag{2.14}$$

However, in the last years some studies have come up with better and more precise models, yet simple enough, to replicate the thrust produced by the Esail. Some authors use polynomial approximations of the parameters such as the variation of the modulus with respect to the inclination angle, also known as sail pitch angle α_n, since it no longer coincides with the thrust cone angle α, because the surface created by the charged tethers is no longer supposed planar, among other reasons ([27], [28]).

Another model, the one chosen for this project, is developed from a geometrical standpoint, and matches very precisely with the polynomial approximation [29]. Specifically, the dependence of the modulus with the attitude of the spacecraft is given by

$$\gamma = \frac{\sqrt{1+3\cos^2\alpha_n}}{2} \tag{2.15}$$

where γ is a nondimensional measure of thrust modulus, defined as

$$\gamma = \frac{a}{\tau a_c \left(\frac{r_\oplus}{r}\right)} \tag{2.16}$$

The relation between the thrust cone angle and the sail cone angle is given by

$$\cos\alpha = \frac{1+\cos^2\alpha_n}{\sqrt{1+3\cos^2\alpha_n}} \tag{2.17}$$

Thus, our thrust model has two degrees of freedom: thrust modulus and its direction (direction only provides one degree of freedom due to the 2D simplification). Since α and α_n are closely related by (2.17), our control parameters can be either $\{\tau, \alpha\}$ or $\{\tau, \alpha_n\}$. We opt for the latter since a specific α_n unequivocally determines α.

There have also been simulations conducted that showed that the dependence of thrust modulus with respect to the distance from the Sun is more correctly estimated with a decay of r^{-1}, rather than $r^{-7/6}$ [8].

With all these new approximations, the thrust model is now represented in (2.18), using τ and α_n as the control parameters.

$$\begin{aligned} a_r &= \tau \frac{a_c}{2} \left(\frac{r_\oplus}{r}\right) \left(1+\cos^2\alpha_n\right) \\ a_\theta &= \tau \frac{a_c}{2} \left(\frac{r_\oplus}{r}\right) \cos\alpha_n \sin\alpha_n \end{aligned} \tag{2.18}$$

A concept visualization of thrust model in (2.18) is presented in figure 2.2.

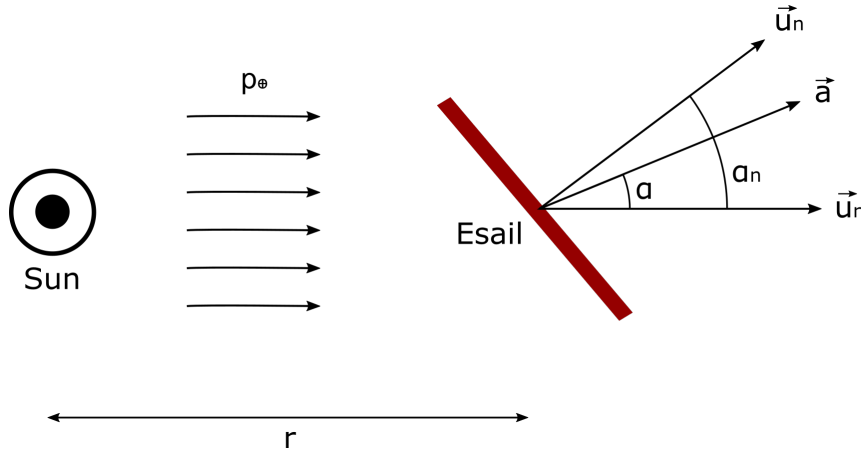

Figure 2.2 Conceptual Esail thrust model illustration.

Equations 2.15 show that thrust modulus, in fact, depends on the sail pitch angle α_n (and consequently on α too). A geometrical representation of the variation of γ as well as α with α_n can be seen in figure 2.3. In figure 2.4 an illustration of how thrust vector modulus and cone angle vary with respect to the pitch angle of the Esail is presented. In that representation, vectors' length is proportional to thrust modulus.

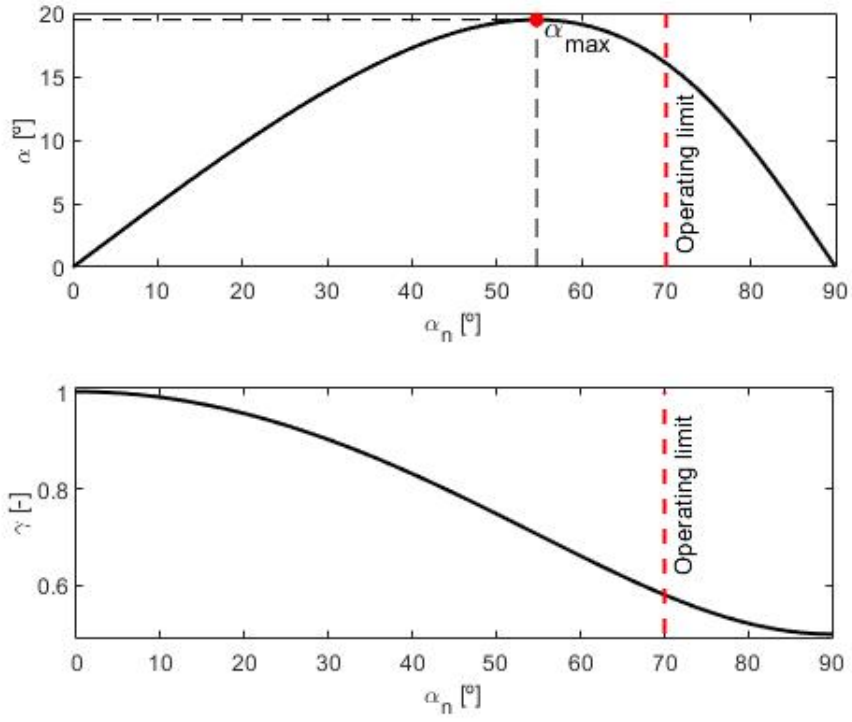

Figure 2.3 Variation with respect to α_n of α (top) and γ (bottom).

With this model, the thrust cone angle presents a maximum value, as figure 2.3 shows. We can compute for which value of the sail pitch angle this occurs, resulting in

$$\alpha_n|_{\alpha=\alpha_{max}} = \arccos\left(\frac{1}{\sqrt{3}}\right) \qquad \alpha_{max} = \arctan\left(\frac{1}{2\sqrt{2}}\right) \tag{2.19}$$

It is also interesting to compute the sail pitch angle for which tangential acceleration is maximum, since it is ultimately a_θ that can change the angular momentum of the osculating orbit, as stated at the start of the

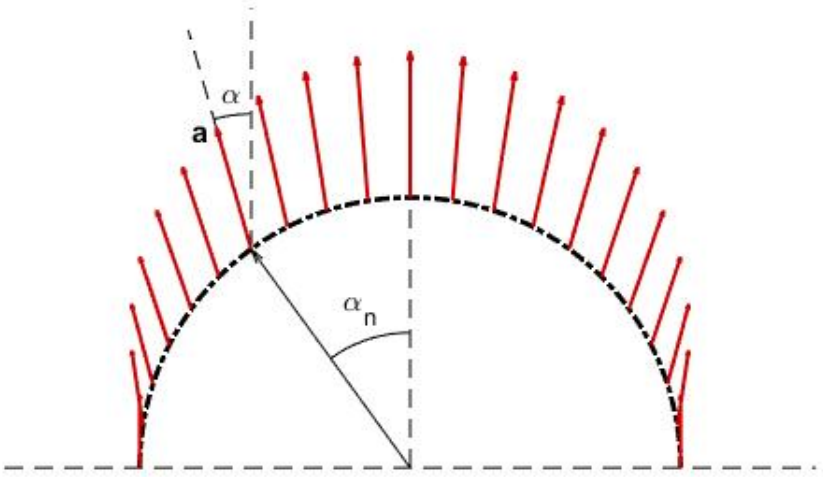

Figure 2.4 Conceptual representation of thrust variation depending on sail pitch angle.

chapter. These values are

$$\alpha_n|_{a_\theta = a_{\theta_{max}}} = 45^\circ \qquad \gamma = \sqrt{\frac{5}{8}}, \qquad \gamma_{\theta_{max}} = \frac{1}{4} \tag{2.20}$$

Here, γ_θ represents the component of γ that goes in the tangential direction (equivalent to nondimensionalizing a_θ as was done with a in (2.16).

By introducing (2.18) in (2.11) accordingly, we obtain the motion of the spacecraft given that the only forces acting on it are the gravitational attraction of the Sun and the Esail thrust. These final laws of motion are

$$\begin{aligned}
\dot{r} &= v_r \\
\dot{\theta} &= \frac{v_\theta}{r} \\
\dot{v_r} &= \frac{v_\theta^2}{r} - \frac{\mu}{r^2} + \tau \frac{a_c}{2} \left(\frac{r_\oplus}{r}\right) \left(1 + \cos^2 \alpha_n\right) \\
\dot{v_\theta} &= -\frac{v_r v_\theta}{r} + \tau \frac{a_c}{2} \left(\frac{r_\oplus}{r}\right) \cos \alpha_n \sin \alpha_n
\end{aligned} \tag{2.21}$$

A linear dependence between τ and the time derivative of velocities is observed, fact that becomes important later on.

2.2.2 Practical limitations of the Esail

We have determined the model we are going to use to approximate the thrust produced by the Esail, and we have also defined the control parameters τ and α_n, but, as it can probably be guessed, not all the values are compatible, since there exists a variety of practical and physical limitations that we have to take into account.

We have assumed that thrust is independent of the spacecraft velocity. This is not exactly physically correct, since thrust produced by the Esail comes from decelerating protons from the solar wind, and in that transfer

of momentum the relative velocity between the spacecraft and the solar wind should be considered. But, since the Earth averages 30 km/s (less in the case of Jupiter) and the solar wind about 400 km/s, we can assume that the difference of velocities is sufficiently high to ignore this phenomenon [6]. Because of this, a maximum velocity is imposed for the spacecraft in the next sections, though in practice it is not relevant since the spacecraft hardly ever travels faster than the Earth in missions to outer planets, which are the ones that are studied.

Apart from that, there is also a limitation in the maximum sail pitch angle that the Esail can reach. More simulations and studies are being conducted in this regard, since it is a complex calculation, but the current results approximate this value in $\alpha_{n_{max}} = 60 - 70^{\circ}$.

Lastly, there are also limitations on how much thrust the Esail can produce at a given distance from the Sun. There exists a voltage of saturation V approximately given by the value such that eV surpasses the kinetic energy of the solar wind protons, that is about 1keV, ignoring initially its dependence with the distance from the Sun. That means that, given a distance from the Sun, and assuming that the grid voltage is high enough, one can calculate the maximum thrust that can be produced by the Esail. Initially, various simulations were run, taking into account that the electron gun may not be as effective as theoretically, since there would be electrons along the Esail trapped by the wires potential, and that reduces the voltage difference, resulting in a lesser flux momentum extraction [24]. However, a series of more recent simulations studied the effect of the electron orbit chaotisation caused by the spacecraft body, which leaded to a much faster release of the trapped electrons in the structure, resulting in an increase in thrust of about 500% [10].

There is also a study that proposes a mass budget model, in order to estimate these characteristic accelerations [30]. It uses the results of thrust produced by a tether per unit of length obtained in [10] to model a real spacecraft, with sensors, scientific equipment, etc. By estimating the total mass of the spacecraft and establishing the number of tethers and their length, one can compute the maximum acceleration (at 1AU) a_c that the Esail can produce. This characteristic acceleration can typically range from 0.1 mm/s^2 to 6 mm/s^2. Usually, a value of 1 mm/s^2 is utilized in orbit determining investigations.

For this project a conservative value of $a_c = 0.6$ mm/s^2 is used. It is less than the typical 1 mm/s^2, but this accounts for a major payload mass of the spacecraft. Since we are planning missions as far as to Jupiter, the scientific equipment that the spacecraft carries becomes prominent. Given that the thrust produced by the Esail remains constant, an increment in the spacecraft total mass translates into a decrease in the characteristic acceleration.

2.3 Solar wind uncertainty

The Esail extracts momentum from solar wind energy flux. Specifically, it uses long thin wires electrically charged to repel protons from the solar wind. That repulsion, by the principle of action and reaction, induces a thrust force in the Esail. But there exists a saturation value from which an increase in voltage does not produce more thrust. Hence, the maximum characteristic acceleration of our spacecraft is dependent on the intensity of the solar wind. An approximation of that dependence when we are not far from 1 AU distance from the Sun is equation 2.22.

$$\frac{dF}{dz} = 0.18 \max\left(0, V_0 - V_1\right) \sqrt{\varepsilon_0 p_{\oplus}} \tag{2.22}$$

where dF/dz is the thrust generated per tether and unit of length, V_0 corresponds the tether voltage in kV, V_1 the solar wind electric potential in kV, ε_0 is the vacuum permittivity and $p_{\oplus}$ denotes the dynamic pressure of the Sun at 1 AU distance from it, defined in equation 2.23.

$$p_{\oplus} = m_p n_{\oplus} u_{\oplus}^2 \tag{2.23}$$

here m_p represents the mass of the proton (in kg), $n_{\oplus}$ the local solar wind number density at 1AU (in cm^{-3}) and $u_{\oplus}$ the velocity of the solar wind at 1 AU (in km/s) [29]. This dynamic pressure of the Sun at 1 AU is simply called dynamic pressure from now on.

We can then see that the force produced by the Esail is proportional to the square root of the dynamic pressure of solar wind. The value of $p_\oplus$ influences the maximum thrust that can be produced by the Esail.

2.3.1 High variability of solar wind

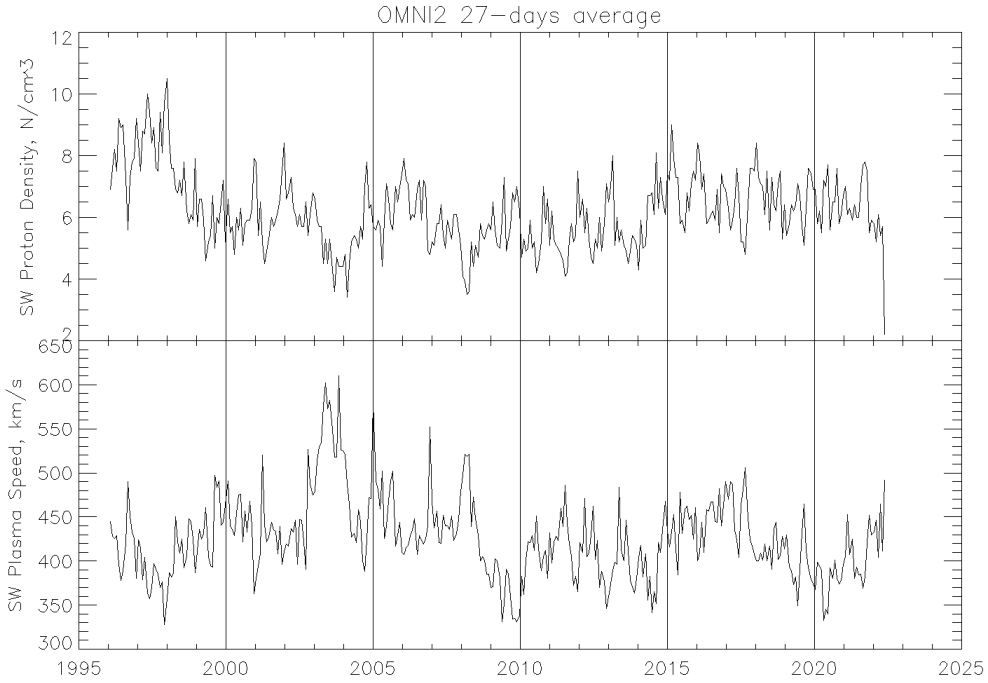

Figure 2.5 Evolution with time of proton density and speed on solar wind. Data extracted from NASA.

Predicting the dynamic pressure of the Sun is highly difficult. Its intrinsic chaotic and turbulent processes happening in its interior make the fluctuations of solar wind greatly noticeable. In figure 2.5, fluctuations with respect to time of proton density and speed on solar wind, averaged each 27 days, can be observed. These data are gathered from the NASA OMNIWeb Data Explorer.

Using the definition of dynamic pressure and applying some statistics, we can obtain the probability density function of the dynamic pressure $p_\oplus$. This distribution can be observed in figure 2.6.

In figure 2.6, the mean dynamic pressure value can be estimated, resulting approximately $\overline{p_\oplus} \approx 2$ nPa, value which we use for the next chapters. Its standard deviation is $\sigma_{p_\oplus} \approx 1.56$ nPa.

This significant fluctuation of solar wind dynamic pressure becomes relevant later on, since it affects considerably the trajectory that the spacecraft ultimately follows. That represents the intrinsic challenge of all kinds of solar sail propulsion systems, the high variability of the propulsive force, compared to the well defined thrust at every instant of, for example, ion thrusters.

2.3.2 Modeling the solar dynamic pressure

As it can be seen in figure 2.6, the solar dynamic pressure probability density function resembles a gamma distribution, with its steep start for small values on the left side of the chart and its long tail on the right side. A gamma distribution Probability Density Function (PDF) is of the form of (2.24), particularized for the dynamic pressure.

$$f(p_\oplus) = \frac{\beta^{-\alpha}}{\Gamma(\alpha)} p_\oplus^{\alpha-1} \exp(-p_\oplus/\beta) \tag{2.24}$$

where α is the shape parameter and β the scale parameter. Knowing that the dynamic pressure mean value is approximately 2 nPa (and that $\overline{p_\oplus} = \alpha \cdot \beta$), and standard deviation is approximately 1.56 nPa (given

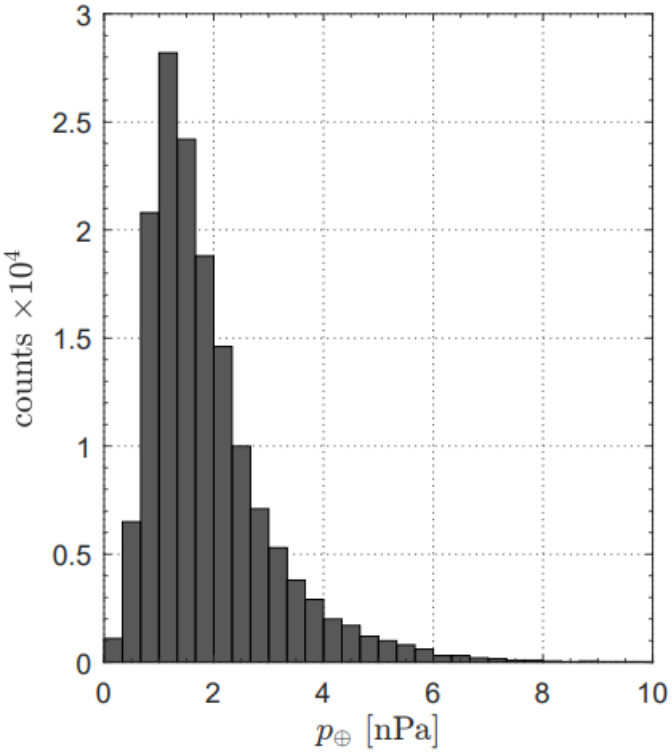

Figure 2.6 Probability density function of $p_{\oplus}$. Image taken from [2] and data extracted from NASA.

$\sigma_{p_{\oplus}} = \sqrt{\alpha}\beta$) we can look for the values of α and β that best approximate the probability density function. According to [2] and following mean and standard deviation formulas, these values end up being approximately $\alpha = 1.6437$ and $\beta = 1.2168$. A comparison between real measurements in figure 2.6 and the Gamma PDF approximation in equation 2.24 can be seen in figure 2.7.

Our PDF is a good approximation, although it is not perfect. Statistical parameters such as skewness and kurtosis of the distribution vary significantly, as table 2.3 shows. Some studies regarding how these fluctuations impact on solar wind trajectories have refined this PDF function to best resemble real data [3]. However, for the sake of simplicity, we opt for the Gamma PDF approximation in (2.24) here.

Table 2.3 Statistical properties differences between real NASA gathered data and Gamma PDF approximation.

Source	OMNIWeb Database	Gamma PDF
$\overline{p_{\oplus}}$ [nPa]	2.00	2.00
$\sigma_{p_{\oplus}}$ [nPa]	1.56	1.56
kurtosis	33.13	3.65
skewness	4.09	1.56

2.4 Neglecting other forces

One of our hypotheses for this project is that the only forces considered for the dynamic equations of our spacecraft are gravitational attraction of the Sun and Esail thrust. Logically, in real world missions these are not the only forces acting on the spacecraft. The gravitational influence of other planets is the most prominent perturbation that is being neglected here. However, this simplification is supported by various reasons.

Comparing the strength of gravitational forces, one can easily observe that the attraction produced from the Sun is orders of magnitude bigger than the one produced by any other planet in almost every region of

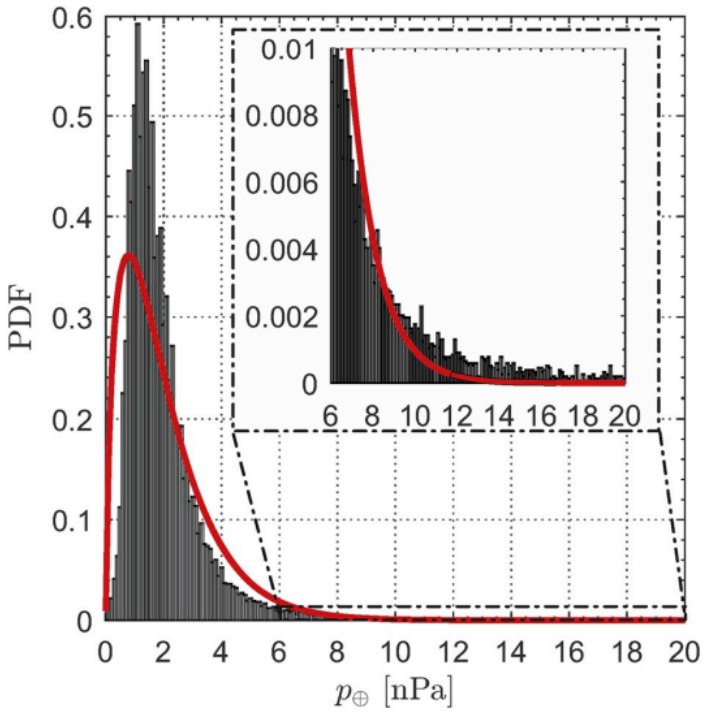

Figure 2.7 Gamma distribution approximation of $p_\oplus$ (red line) compared with real data gathered from NASA (bars). Image taken from [3].

space. Looking at equation 2.6, we can see that the intensity of the attraction is directly proportional to the Standard Gravitational Parameter. In table 2.4 are presented the Standard Gravitational Parameters of all planets in the Solar System, and also the Sun. The latter one is various orders of magnitude bigger than the rest.

As equation 2.6 shows, the gravitational force intensity also depends on the distance to the body, and a study can be conducted about the regions of space where a body exerts more gravitational force than the other. When one of the two bodies is much massive than the other, this region can be approximated to be a sphere centered in the smaller one, called the Sphere Of Influence (SOI), first addressed by Pierre Simon de Laplace (1749 - 1827). The radius of this sphere can be approximated as equation 2.25 shows.

$$r_{SOI} \approx a \left(\frac{m}{M}\right)^{2/5} \tag{2.25}$$

where a is the semi-major axis of the smaller object's orbit around the more massive body, m is the mass of the lighter body and M the mass of the larger one. The radii of the planet's spheres of influence with the Sun as the massive body is tabulated in 2.4.

In this project we study optimal trajectories and control strategies to achieve rendezvous with planets, and our spatial stopping criteria to consider the arrival to the planet is precisely reaching its sphere of influence. That means that, throughout all the flight, Sun force is stronger than the planets', thus validating our hypothesis.

Table 2.4 Standard Gravitational Parameters of planets of the Solar System and the Sun and radii of spheres of influence.

Planet	☿	♀	⊕	♂	⚳	♃	♁	♆	☉
μ [km^{3}s^{-2}]	$2.2{\cdot}10^4$	$3.2{\cdot}10^5$	$4.0{\cdot}10^5$	$4.3{\cdot}10^4$	$1.3{\cdot}10^8$	$3.8{\cdot}10^7$	$5.8\cdot10^6$	$6.8{\cdot}10^6$	$1.3{\cdot}10^{11}$
r_{SOI}[km]	$1.2{\cdot}10^5$	$6.2{\cdot}10^5$	$9.3{\cdot}10^5$	$5.8{\cdot}10^5$	$4.8{\cdot}10^7$	$5.5{\cdot}10^7$	$5.2{\cdot}10^7$	$8.6{\cdot}10^7$	-

Recalling that this project aims to be a preliminary study on Esail optimal orbits finding and control strategies, this simplification is good enough for a first approximation, given that we are also assuming planet

orbits to be coplanar and circular.

Furthermore, these planet forces are not perturbations per say. Their trajectories are determined, and given launch date, one can predict the magnitude and direction of these forces in an arbitrary point. Because of that, these forces are not truly as much as a problem as the solar wind uncertainty is, and their addition can be considered as future work.

For all the reasons considered, this project assumes only the effects of solar gravitational attraction and Esail thrust, leaving any other possible phenomena inclusion as future work.

3 Optimal mission planning

In this chapter, the optimal orbit control problem is tackled. Our goal is to find adequate functions for our control parameters such that some kind of optimal law is satisfied, given the limitations and particularities of our continuous thrust spacecraft, along with the necessary restrictions to fulfill obligatory requirements.

In particular, our goal in this chapter is to find time-optimal transfer orbits, that is, find the necessary control parameters distribution as functions of time that lead to the fastest transfer orbit that takes the spacecraft from one point to another, fulfilling some extra constraints in velocity. All of this initially excluding solar wind variability, therefore assuming a nominal solar dynamic pressure of $p_{\oplus} = 2$ nPa.

As representative common missions, we focus our attention on the transfer orbit missions between the Earth and Jupiter, and the Earth and Mars. Our goal is to reach these planets at the necessary velocity to keep orbiting the Sun at that distance in a circular orbit, just as the planet does (in other words, arrive with the least velocity possible with respect to the planet).

3.1 Optimal Control Problem formulation

Our goal in this section is to find the optimal transfer orbit between the Earth and both Mars and Jupiter with the limitations of our thrust model. As previously mentioned, we define the optimal orbit to be the one that requires the least time to complete, which is to say, our goal is to minimize the total transfer time.

3.1.1 Problem hypotheses

To solve this, we recall a series of simplifications established in Chapters 2.1.2 and 2.4 that make the problem manageable. Therefore, we assume the next hypotheses:

- **Coplanar orbits**. The orbits of the planets are supposed coplanar, that is, all of them are contained in the ecliptic plane of the Solar System.
- **Circular orbits**. The orbits of the planets are supposed circular and concentric, with the Sun in the center of them.
- **Freedom in launch date choosing**. The launch date of the mission is free to choose, ensuring that the spacecraft meets the arrival planet when it reaches its orbit.
- **No Sun perturbations**. To find the optimal transfer orbit, solar perturbations are neglected. It is a matter of the next section to include them and study closed-loop control strategies.
- **Only Sun attraction and Esail thrust**. Only these forces are taken into account. Others such as gravitational attraction of planets are neglected.

3.1.2 Defining our optimal control problem

In mathematics, optimal control theory is a branch of mathematical optimization whose goal is to find a control over a period of time for a dynamical system such that a particular objective function (or cost function)

is optimized. Our optimal orbit finding problem falls in this field of mathematics. These problems are usually denoted as an Optimal Control Problem (OCP).

The general formulation of the continuous problem is stated as follows [31]. We want to minimize some arbitrary cost function J, generically defined as in equation 3.1.

$$J\left[\boldsymbol{x}(\cdot),\boldsymbol{u}(\cdot),t_0,t_f\right] = \varphi\left[\boldsymbol{x}(t_0),t_0,\boldsymbol{x}(t_f),t_f\right] + \int_{t_0}^{t_f} \mathscr{L}\left[\boldsymbol{x}(t),\boldsymbol{u}(t),t\right] \mathrm{d}t \tag{3.1}$$

If our cost function only has the first term φ, it is said that it is expressed in the Mayer form. If it only consists of the second, integral term, the problem is referred as a Lagrange problem. If it contains both terms it is said to be in Bolza form. In fact, by adding an extra state variable to the problem we can express every cost function in the Mayer form, although it is not always desirable from a convergence point of view. The problem is subject to the state equations

$$\dot{\boldsymbol{x}}(t) = \boldsymbol{f}\left[\boldsymbol{x}(t),\boldsymbol{u}(t),t\right] \tag{3.2}$$

and also to a series of path constraints

$$\boldsymbol{h}\left[\boldsymbol{x}(t),\boldsymbol{u}(t),t\right] \leqslant 0 \tag{3.3}$$

and boundary conditions

$$\boldsymbol{g}\left[\boldsymbol{x}(t_0),t_0,\boldsymbol{x}(t_f),t_f\right] = 0 \tag{3.4}$$

Here the bold notation means that the variable is a vector. In our problem, our state variables are $\boldsymbol{x}$ are $\{r, \theta, v_r, v_\theta\}$ and our control parameters $\boldsymbol{u}$ are $\{\tau, \alpha_n\}$. The functions $\boldsymbol{f}$, $\boldsymbol{h}$, $\boldsymbol{g}$ are in bold because each of them refers to numerous equations that represent all the restrictions.

We now particularize this general formulation to our specific problem. We are seeking a minimum-time trajectory, so our cost function is simply defined as

$$J(t_0,t_f) = t_f - t_0 \tag{3.5}$$

Our dynamic or state equations are defined in (2.21). We recall them here:

$$\begin{aligned}
\dot{r} &= v_r \\
\dot{\theta} &= \frac{v_\theta}{r} \\
\dot{v_r} &= \frac{v_\theta^2}{r} - \frac{\mu}{r^2} + \tau \frac{a_c}{2}\left(\frac{r_\oplus}{r}\right)\left(1+\cos^2\alpha_n\right) \\
\dot{v_\theta} &= -\frac{v_r v_\theta}{r} + \tau \frac{a_c}{2}\left(\frac{r_\oplus}{r}\right)\cos\alpha_n \sin\alpha_n
\end{aligned} \tag{3.6}$$

We have three different path constraints: the boundary values of our control parameters, and a maximum velocity constraint (explained in Chapter 2.2.2). These constraints are defined in (3.7).

$$\begin{aligned}
0 \leqslant \tau(t) &\leqslant 1 \\
-\alpha_n^{max} \leqslant \alpha_n(t) &\leqslant \alpha_n^{max} \\
v_r^2(t) + v_\theta^2(t) &\leqslant v_{max}^2
\end{aligned} \tag{3.7}$$

Lastly, given that the spacecraft leaves the Earth with zero excess velocity, and that we want it to reach the corresponding planet with its same velocity, those imply a series of conditions in the initial and final values of speed presented in (3.8).

$$\begin{aligned} r(t_0) &= r_\oplus \\ \theta(t_0) &= 0 \\ v_r(t_0) &= 0 \\ v_\theta(t_0) &= v_\oplus \\ r(t_f) &= r_i \\ v_r(t_f) &= 0 \\ v_\theta(t_f) &= v_i \end{aligned} \tag{3.8}$$

Here, $i = \mathrm{♂}, \mathrm{♃}$, depending on whether we are referring to Mars or Jupiter. The velocity of the planets can be easily calculated as $v_{\theta_i} = \sqrt{\mu_\odot / r_i}$.

Note that in (3.7) we refer to a maximum velocity v_{max} not yet defined. That fact is to take into account the phenomena of going at a non-negligible speed compared to the solar wind velocity, scenario that makes our thrust model lose accuracy. In reality, the velocity of the Earth is hardly ever surpassed, as it is demonstrated further on, so this restriction is not considered.

There is also an extra constraint in the initial conditions: $\theta(t_0) = 0$. θ could actually be any value, it is only used to specify an initial condition of the spacecraft, but since this problem has rotational symmetry, the specific value is not relevant, hence its value of 0 for simplicity sake. The reason why θ does not appear in the final boundary constraints is because we are able to choose launch date, as stated in Chapter 3.1.1. That fact, combined with the rotational symmetry property, let us choose the phase angle needed to meet the corresponding planet when we reach its orbit. Therefore, θ_f is not a restriction.

There are a couple of more observations that have to be made. The first one is that, for simplicity sake, we opt to use astronomical units. This set of units is defined such that the mean distance from the Earth to the Sun equals 1 Astronomical Unit (AU), and the mean velocity of the Earth equals 1 Units of Velocity (UV). Given those two premises, it is easy to see that the Standard Gravitational Parameter of the Sun equals to $\mu_\odot = 1$ AU UV^2, and we can also compute the rest of unit conversions:

$$\begin{aligned} &1 \text{ AU} = 149.598 \cdot 10^6 \text{ km} \\ &1 \text{ UV} = 29.7847 \text{ km/s} \\ &1 \text{ UT} = 58.1324 \text{ days} \\ &1 \text{ UA} = 5.9301 \text{ mm/s}^2 \end{aligned} \tag{3.9}$$

With Units of Time (UT) and Units of Acceleration (UA).

In Chapter 2.2.2 we mentioned the use of a characteristic acceleration of $a_c = 0.6$ mm/s^2. Actually, in this chapter, we utilize 60% of it, 0.36 mm/s^2. In simple terms, this control margin is left to be able to deal with solar perturbations later on in the next chapter. This margin is then validated there, we take it as a given for now. In astronomical units, the value of the characteristic acceleration is $a_c = 0.0607$ UA.

We can also consider leaving some kind of margin in the sail pitch angle. Being the boundary value $\pm 70^\circ$, we may want to limit its value here to $\pm 60^\circ$. However, if we look at the evolution of thrust modulus and cone angle in figure 2.3, we can see that there is no particular reason for the Esail to opt for values of α_n much bigger than $\alpha_n|_{\alpha=\alpha_{max}} \approx 55^\circ$, since that now means reducing thrust modulus and cone angle. In fact, maximum tangential acceleration, for example, is given for $\alpha_n|_{a_\theta = a_{\theta_{max}}} = 45^\circ$, as stated in equation 2.20. Given those reasons, no control margin is left here for the sail pitch angle.

Additionally, without loss of generality, we assume the initial time to be $t_0 = 0$. That means our cost function is now $J = t_f$, being t_f, logically, an unknown parameter. To increase the robustness of the problem, we add an extra condition that states that the final time must be positive ($t_f \geqslant 0$). After all these considerations, our final OCP formulation is presented in (3.10).

$$\min_{\tau,\alpha_n} \quad t_f$$

subject to

$$\begin{aligned}
\dot{r} &= v_r \\
\dot{\theta} &= \frac{v_\theta}{r} \\
\dot{v_r} &= \frac{v_\theta^2}{r} - \frac{\mu}{r^2} + \tau \frac{a_c}{2}\left(\frac{r_\oplus}{r}\right)\left(1+\cos^2\alpha_n\right) \\
\dot{v_\theta} &= -\frac{v_r v_\theta}{r} + \tau \frac{a_c}{2}\left(\frac{r_\oplus}{r}\right)\cos\alpha_n \sin\alpha_n
\end{aligned}$$

$$\begin{aligned}
0 \leqslant \tau(t) &\leqslant 1 \\
-\alpha_n^{max} \leqslant \alpha_n(t) &\leqslant \alpha_n^{max} \qquad t \in \left[0, t_f\right]
\end{aligned} \tag{3.10}$$

$$\begin{aligned}
r(0) &= r_\oplus \\
\theta(0) &= 0 \\
v_r(0) &= 0 \\
v_\theta(0) &= v_\oplus \\
r\left(t_f\right) &= r_i \\
v_r\left(t_f\right) &= 0 \\
v_\theta\left(t_f\right) &= v_i
\end{aligned}$$

$$t_f \geqslant 0$$

Where $a_c = 0.0607$ UA, $\alpha_n^{max} = 70^\circ$, μ = 1 AU UV^2, $r_\oplus = 1$ AU, $r_{♂} = 1.5237$ AU, $r_{♃} = 5.2043$ AU, $v_{♂} = 0.8101$ UV, $v_{♃} = 0.4383$ UV.

Lastly, we discuss some considerations about the nature of this problem. Historically, time-optimal problems have always been difficult to solve due to instabilities produced by the non-fixed in time boundary final conditions, among other reasons. Furthermore, our restrictions are non-convex and extremely non-linear, and that means that there possibly exist multiple local solutions to our problem. That makes our solution distinctly sensitive to the initial guess. Depending on it, and on the algorithm used, our problem can end up being infeasible, or in different local optima. For these reasons, finding a global-optimum of the problem is an extremely difficult task. Our goal is not to find this global solution, but rather a local one that, in practice, is close enough to the global.

We first study the optimal solution of the problem using indirect methods, which let us impose optimality conditions prior to numerically tackling it. This approach reveals certain behaviours that the optimal solution must follow, and serves as a way to ease the task of numerically solving it later by giving useful information about active/inactive restrictions and initial guesses. However, the proper numerical calculation is made using a direct transcription method that let us convert our problem into a Non Linear Programming (NLP) problem. Broadly speaking, it is often said that indirect approaches are about optimizing, and then discretizing, while direct approaches first discretize the problem in time intervals, to then solve for the now finite set of unknowns using some kind of optimization algorithm.

3.2 Indirect approaches for OCPs

The aim of this section is to study the problem from what is called an indirect approach, so we can make conclusions about how our optimal solution looks like, specially the optimal laws for our control parameters. However, solving the Two Point Boundary Value Problem (TPBVP) that is later posed is beyond the

scope of the project, although some references, where equivalent problems are tackled in this way, are included.

A way of solving OCPs is trying to find a solution to the closed system of necessary conditions that need to be satisfied for the solution to be optimal. Normally, this is achieved by expanding the state variables to the costate space. An analogous way to think of them is as Lagrange multipliers associated with the state equations. Since we have four state variables $\{r, \theta, v_r, v_\theta\}$, we now also have four costate variables $\{\lambda_r, \lambda_\theta, \lambda_{v_r}, \lambda_{v_\theta}\}$, that satisfy the Euler-Lagrange equations

$$\dot{\lambda}_i = -\frac{\partial H}{\partial i} \tag{3.11}$$

With $i = r, \theta, v_r, v_\theta$ depending on the state variable we refer to. Denoting the set of state variables $\boldsymbol{x}$, the set of costate variables $\boldsymbol{\lambda}$ and the set of control parameters $\boldsymbol{u}$, we now have eight equations expressed in 3.12.

$$\begin{aligned} \dot{\boldsymbol{x}} &= \boldsymbol{f}(\boldsymbol{x}, \boldsymbol{u}, t) \\ \dot{\boldsymbol{\lambda}} &= \boldsymbol{g}(\boldsymbol{x}, \boldsymbol{u}, \boldsymbol{\lambda}, t) \end{aligned} \tag{3.12}$$

In equation 3.11, H denotes the Hamiltonian of the system, defined generically as

$$H = \mathscr{L} + \boldsymbol{\lambda}^{\mathsf{T}} \boldsymbol{f} \tag{3.13}$$

where $\mathscr{L}$ refers to the integrand in the cost function integral term in 3.1. Note that $H = H(\boldsymbol{x}, \boldsymbol{u}, \boldsymbol{\lambda}, t)$, hence dependences in (3.12).

The set of equations in (3.12) can be closed if we manage to find an optimal law of the form $\boldsymbol{u} = \boldsymbol{u}(\boldsymbol{x}, \boldsymbol{\lambda}, t)$, because then we have eight equations for eight unknown variables (we are first assuming that arrival time is fixed, this degree of freedom is tackled later). The way to do this is by using Pontryagin's Minimum Principle Pontryagin's Minimum Principle (PMP), that establishes a necessary condition (although not sufficient) that the control parameters $\boldsymbol{u}$ have to follow for the solution to be optimal. Even if it is not a sufficient solution, it often points towards the right direction, and it is common practice to so. Once we find a solution, we can check if it satisfies Hamilton-Jacobi-Bellman equation (HJB equation) to ensure its optimality. PMP states that, if we want to minimize a cost function J, then control parameters must be chosen such that the Hamiltonian is minimized at every instant of time, in other words $\partial H / \partial \boldsymbol{u} = 0 \quad \forall t \in [t_0, t_f]$, given that we then check that it is indeed a minimum and not a maximum or saddle point. With these equations, we can obtain the optimal control law of the form $\boldsymbol{u} = \boldsymbol{u}(\boldsymbol{x}, \boldsymbol{\lambda}, t)$, therefore closing our system, that is now in the following form

$$\begin{aligned} \dot{\boldsymbol{x}} &= \boldsymbol{f}(\boldsymbol{x}, \boldsymbol{u}, t) \\ \dot{\boldsymbol{\lambda}} &= \boldsymbol{g}(\boldsymbol{x}, \boldsymbol{u}, \boldsymbol{\lambda}, t) \\ \boldsymbol{u} &= \boldsymbol{u}(\boldsymbol{x}, \boldsymbol{\lambda}, t) \end{aligned} \tag{3.14}$$

In (3.14), $\dot{\boldsymbol{\lambda}}$ and $\dot{\boldsymbol{x}}$ depend on $\boldsymbol{u}$, but since $\boldsymbol{u} = \boldsymbol{u}(\boldsymbol{x}, \boldsymbol{\lambda}, t)$, we can write

$$\begin{aligned} \dot{\boldsymbol{x}} &= \boldsymbol{f}(\boldsymbol{x}, \boldsymbol{\lambda}, t) \\ \dot{\boldsymbol{\lambda}} &= \boldsymbol{g}(\boldsymbol{x}, \boldsymbol{\lambda}, t) \end{aligned} \tag{3.15}$$

thus closing our system. For these eight equations we need eight boundary values. Seven of them, shown in (3.16), have already been mentioned before.

$$\begin{aligned} r(0) &= r_\oplus \\ \theta(0) &= 0 \\ v_r(0) &= 0 \\ v_\theta(0) &= v_\oplus \\ r(t_f) &= r_i \\ v_r(t_f) &= 0 \\ v_\theta(t_f) &= v_i \end{aligned} \tag{3.16}$$

The last restriction is related to the fact that the angle θ_f is free to choose. In terms of costate variables, this is represented as $\lambda_\theta\left(t_f\right)=0$.

For our particular problem, the cost function is $J=t_f$, that means that $\varphi=t_f$ and $\mathscr{L}=0$. Consequently, our Hamiltonian is defined as equation 3.17 shows.

$$H=\lambda_r v_r+\lambda_\theta\frac{v_\theta}{r}+\lambda_{v_r}\left(\frac{v_\theta^2}{r}-\frac{\mu}{r^2}\right)-\lambda_{v_\theta}\frac{v_r v_\theta}{r}+\tau\frac{a_c}{2}\left(\frac{r_\oplus}{r}\right)\left[\lambda_{v_r}\left(1+\cos^2\alpha_n\right)+\lambda_{v_\theta}\cos\alpha_n\sin\alpha_n\right] \tag{3.17}$$

Given the Hamiltonian, we can now compute the Euler-Lagrange differential equations. These are shown in 3.18.

$$\begin{aligned}
\dot{\lambda_r}&=\frac{\lambda_\theta v_\theta}{r^2}+\lambda_{v_r}\left(\frac{v_\theta^2}{r^2}-\frac{2\mu}{r^3}\right)-\lambda_{v_\theta}\frac{v_r v_\theta}{r^2}+\frac{\tau a_c}{2r}\left(\frac{r_\oplus}{r}\right)\left[\lambda_{v_r}\left(1+\cos^2\alpha_n\right)+\lambda_{v_\theta}\cos\alpha_n\sin\alpha_n\right]\\
\dot{\lambda_\theta}&=0\\
\dot{\lambda_{v_r}}&=-\lambda_r+\frac{\lambda_{v_\theta}v_\theta}{r}\\
\dot{\lambda_{v_\theta}}&=-\frac{\lambda_\theta}{r}-\frac{2\lambda_{v_r}v_\theta}{r}+\frac{\lambda_{v_\theta}v_r}{r}
\end{aligned} \tag{3.18}$$

We now find the optimal control law to maximize the Hamiltonian at every instant of time by differentiating it with respect to α_n and τ. We first differentiate with respect to the sail pitch angle, obtaining

$$-\lambda_{v_r}\sin\left(2\alpha_n\right)+\lambda_{v_\theta}\cos\left(2\alpha_n\right)=0 \tag{3.19}$$

equation that has two solutions for α_n

$$\begin{aligned}
\alpha_{n_1}&=\frac{1}{2}\arctan 2\left(\lambda_{v_\theta},\lambda_{v_r}\right)\\
\alpha_{n_2}&=\frac{1}{2}\arctan 2\left(-\lambda_{v_\theta},-\lambda_{v_r}\right)
\end{aligned} \tag{3.20}$$

where $\arctan 2\left(\cdot,\cdot\right)$ represents the two-variable arctangent function. Note that there are two solutions for this equation, we have to check which of them yields a minimum value of the Hamiltonian. Using the second order derivative, we obtain that $\left.\frac{\partial^2 H}{\partial\alpha_n^2}\right|_{\alpha_n=\alpha_{n_1}}<0$, while $\left.\frac{\partial^2 H}{\partial\alpha_n^2}\right|_{\alpha_n=\alpha_{n_2}}>0$. Consequently, to minimize the Hamiltonian we opt for $\alpha_n=\alpha_{n_2}$. But there is also an extra constraint, we need to remember that the sail pitch angle has a maximum value α_n^{max} that must not be surpassed. Consequently, the final definition of the optimal sail pitch angle is given by

$$\alpha_n^\star=\begin{cases}\alpha_n & \text{if} \quad |\alpha_n|\leqslant\alpha_n^{max}\\ \alpha_n^{max}\cdot\operatorname{sign}\left(\alpha_n\right) & \text{if} \quad |\alpha_n|>\alpha_n^{max}\end{cases} \tag{3.21}$$

In figure 3.1, a visual graph of the Hamiltonian term that depends on α_n, along with the representation of optimal value $\alpha_n^\star$ for example values of λ_{v_r} and λ_{v_θ} can be observed. The graphical function represented is: $\tilde{H}$, defined in (3.22), for $\lambda_{v_r}=3$ and $\lambda_{v_\theta}=0.5$.

$$\tilde{H}=\lambda_{v_r}\left(1+\cos^2\alpha_n\right)+\lambda_{v_\theta}\cos\alpha_n\sin\alpha_n \tag{3.22}$$

In terms of the dependence of the Hamiltonian with the control parameter τ, we can see that its relation is linear. That means that the derivative of the Hamiltonian with respect to τ, $\frac{\partial H}{\partial\tau}$ does not depend on τ $\left(\frac{\partial H}{\partial\tau}=\frac{a_c}{2}\left(\frac{r_\oplus}{r}\right)\tilde{H}\right)$. That means that no local maximum or minimum can be encountered in this regard. So, rather than that, we recall Pontryagin's Minimum Principle, which states that our goal is to minimize the Hamiltonian at every instant of time. Consequently, the best possible strategy to do that is to minimize τ when $\tilde{H}>0$ and maximize it when $\tilde{H}<0$. Therefore, given that $\tau\in[0,1]$, the optimal control law for it is represented as

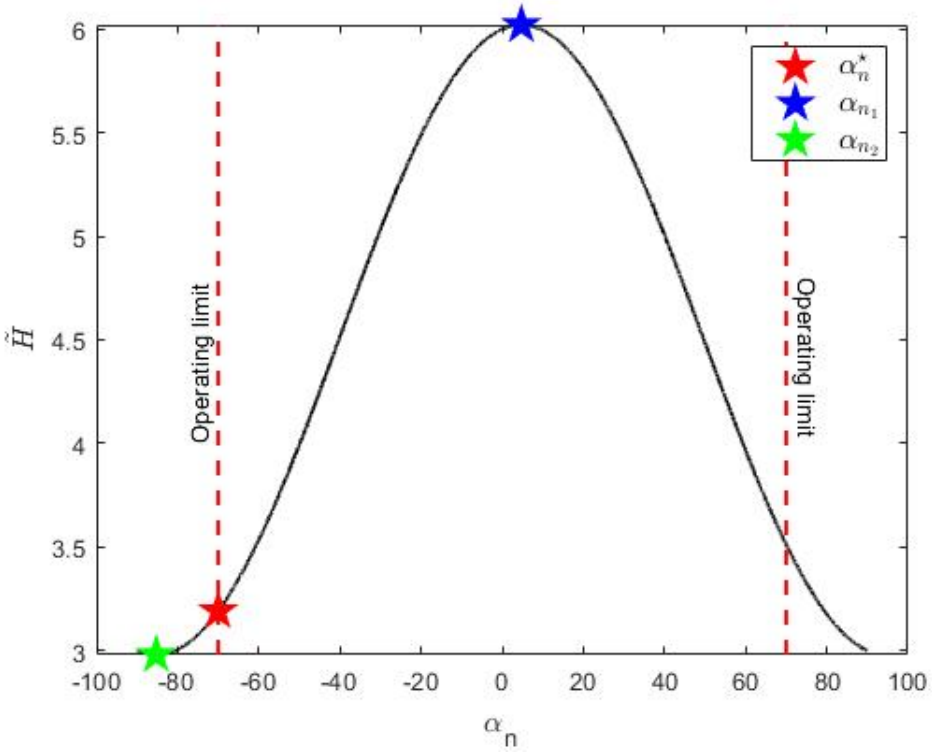

Figure 3.1 Representation of α_{n_1}, α_{n_2}, $\alpha_n^\star$ and its impact on the Hamiltonian.

$$\tau^\star = \begin{cases} 0 & \text{if} \quad \tilde{H} > 0 \\ 1 & \text{if} \quad \tilde{H} \leqslant 0 \end{cases} \tag{3.23}$$

In (3.21) and (3.23), the notation $\cdot^\star$ simply means that we are not referring to a generic feasible optimal law, but to the optimal.

There is an interesting study that can be conducted, and it is related to the boundaries of τ. We can try to solve, in terms of α_n^{max} for which values of λ_{v_r} and λ_{v_θ} τ switches between 0 and 1. The first step is to determine for which region $|\alpha_n| > \alpha_n^{max}$. That region is shown for a particular α_n^{max} of 70° in figure 3.2. As it can be seen, the region is the surface between two lines of slopes $\pm\tan(\pi - 2\alpha_n^{max})$.

We can now study the values where $\tilde{H} = 0$, since those will be the boundary values where τ switches. This boundary depends on α_n^{max}, as one could expect. When $\alpha_n^\star$ is not saturated, that boundary does not depend on α_n^{max}, but when it is, it does. Again, for a value of α_n^{max} of 70°, both boundaries, that end up being lines, are represented in figure 3.3. The slopes are $\pm 2\sqrt{2}$ and $\pm\dfrac{3+\cos(\alpha_n^{max})}{\sin(\alpha_n^{max})}$ for the unsaturated and saturated cases respectively. For both cases, the domain in which $\tau^\star = 0$ is the remaining region to the right of the straight lines. As one could expect, the saturation boundary leaves less space in which $\tau^\star = 1$.

As we can observe from the example in which $\alpha_n^{max} = 70^\circ$, the region of values of λ_{v_r} and λ_{v_θ} for which the sail pitch angle is saturated (figure 3.2) is contained in both saturation and no-saturation regions in which $\tau = 0$ (figure 3.3). So, effectively, for this value of α_n^{max} there is no interference between both, and the boundary region is defined as $\lambda_{v_\theta} = \pm 2\sqrt{2}\lambda_{v_r}, \lambda_{v_r} \geqslant 0$ for all values of λ_{v_r} and λ_{v_θ}. It can be proven that this decoupling is true for all values $\alpha_n^{max} \in \left[\arccos\left(1/\sqrt{3}\right), \pi\right]$. Coupling happens for values $\alpha_n^{max} < \arccos\left(1/\sqrt{3}\right)$, however, we do not consider those scenarios, since, as it was seen in Chapter 2.2.2, we suppose that our Esail has a maximum sail pitch angle of 70°.

All this study concludes that, for our value of $\alpha_n^{max} = 70^\circ$, saturation never happens, and so we can define

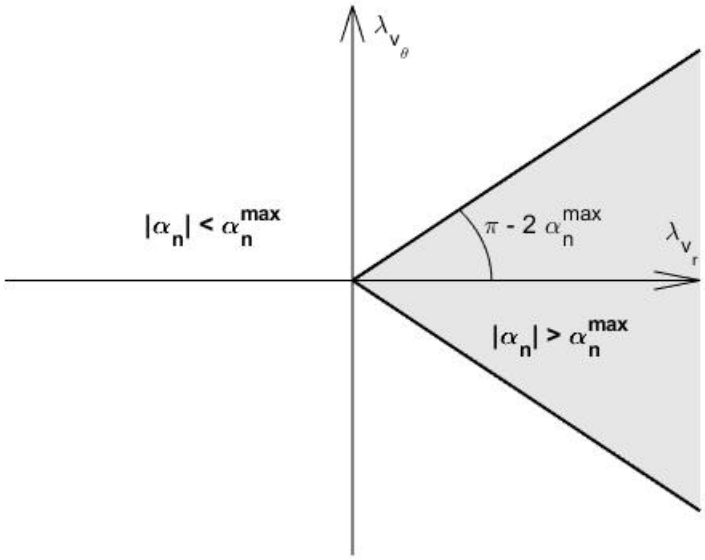

Figure 3.2 Saturation region of α_n in terms of λ_{v_r} and λ_{v_θ}.

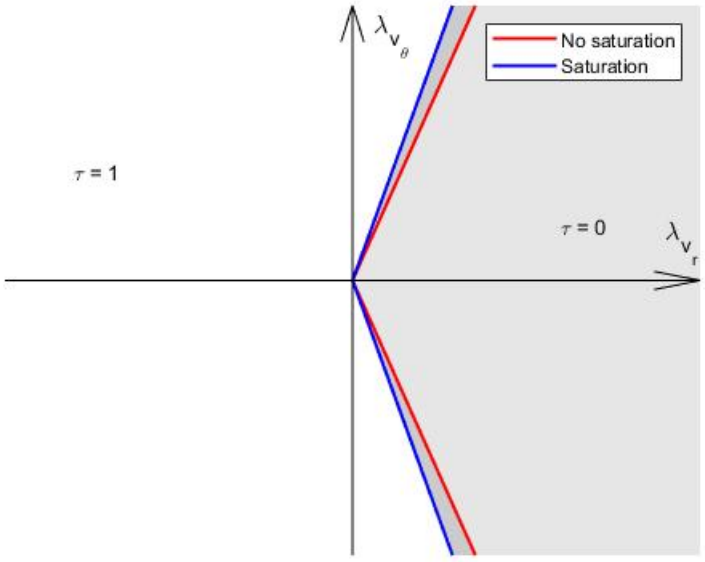

Figure 3.3 Visual representation of τ boundary in terms of λ_{v_r} and λ_{v_θ}.

our optimal sail pitch angle and thrust lever control laws as in (3.24). Now that our sail pitch angle is not limited, thus our control law for it is equivalent to Lawden's Primer Vector control law [32].

$$\begin{aligned} \alpha_n^\star &= \frac{1}{2}\arctan 2\left(-\lambda_{v_\theta}, -\lambda_{v_r}\right) \\ \tau^\star &= \begin{cases} 0 & \text{if} \quad \lambda_{v_r}^2 > \lambda_{v_\theta}^2/8 \\ 1 & \text{if} \quad \lambda_{v_r}^2 \leqslant \lambda_{v_\theta}^2/8 \end{cases} \end{aligned} \tag{3.24}$$

Doing some algebra, it is not hard to show that $\lambda_{v_r}^2 > \lambda_{v_\theta}^2/8$ can be expressed in terms of $\alpha_n^\star$ as $|\alpha_n^\star| > \arccos\left(1/\sqrt{3}\right)$, precisely the value of maximum thrust cone angle mentioned in Chapter 2.2.1. We can the express the optimal laws for control parameters as

$$\begin{aligned} \alpha_n^\star &= \frac{1}{2}\arctan 2\left(-\lambda_{v_\theta}, -\lambda_{v_r}\right) \\ \tau^\star &= \begin{cases} 0 & \text{if} \quad |\alpha_n^\star| > \arccos\left(1/\sqrt{3}\right) \\ 1 & \text{if} \quad |\alpha_n^\star| \leqslant \arccos\left(1/\sqrt{3}\right) \end{cases} \end{aligned} \tag{3.25}$$

This represents an example of why indirect approaches are helpful in many cases. They reveal information, certain laws that an optimal solution must follow. In Chapter 2.2.1, where the thrust model for the Esail was presented, it was remarked the apparent lack of interest in opting for higher values of α_n than $\arccos\left(1/\sqrt{3}\right)$. However, it was only an observation. Now, with the aid of indirect approaches, we have in fact confirmed that an optimal solution never uses angles higher than that, since at that moment they enter the region of $\tau = 0$, and thus the value of α_n does not have any effect in the solution.

There is one aspect previously disregarded that needs to be addressed, and that is that the final time t_f is unknown. Consequently, we have an extra unknown and one more equation is needed to solve the system. Note that t_f, unlike any variable of $\boldsymbol{x}$ or $\boldsymbol{\lambda}$, is a constant, in the sense that it logically does not depend on time. Thus, an algebraic equation is needed, rather than a differential equation with its corresponding initial condition. This equation is given by the transversality condition [31], defined as

$$\left[\frac{\partial \varphi}{\partial t} + H\right]_{t=t_f} = 0 \tag{3.26}$$

For our case, as $\varphi = t_f$, this condition implies that $H\left(t_f\right) = -1$. We have then transformed the OCP to a Two Point Boundary Value Problem (TPBVP), with a set of differential equations, and boundary conditions set in t_0 and t_f. It is interesting to notice that we have defined our objective function to be $\varphi = t_f$ and $\mathscr{L} = 0$, in the form of (3.1). But we could also have defined J as $\varphi = 0$ and $\mathscr{L} = 1$, since $\int_0^{t_f} 1\,\mathrm{d}t = t_f$. In that case, the new Hamiltonian is now $\hat{H} = 1 + H$. However, since 1 is constant, with this new Hamiltonian the Euler-Lagrange equations do not change, and moreover, since $\varphi = 0$ now, the transversality condition in equation 3.26 is now $\hat{H}\left(t_f\right) = 0$, so the condition $H\left(t_f\right) = -1$ holds. Therefore, as expected, all the equations stay the same regardless of the way we define our cost function, since these definitions are equivalent.

Summing all this up, the problem in its entirety is expressed in (3.27).

$$
\begin{aligned}
\dot{r} &= v_r \\
\dot{\theta} &= \frac{v_\theta}{r} \\
\dot{v_r} &= \frac{v_\theta^2}{r} - \frac{\mu}{r^2} + \tau^\star \frac{a_c}{2}\left(\frac{r_\oplus}{r}\right)\left(1+\cos^2\alpha_n^\star\right) \\
\dot{v_\theta} &= -\frac{v_r v_\theta}{r} + \tau^\star \frac{a_c}{2}\left(\frac{r_\oplus}{r}\right)\cos\alpha_n^\star \sin\alpha_n^\star \\
\dot{\lambda_r} &= \frac{\lambda_\theta v_\theta}{r^2} + \lambda_{v_r}\left(\frac{v_\theta^2}{r^2} - \frac{2\mu}{r^3}\right) - \lambda_{v_\theta}\frac{v_r v_\theta}{r^2} + \frac{\tau^\star a_c}{2r}\left(\frac{r_\oplus}{r}\right)\left[\lambda_{v_r}\left(1+\cos^2\alpha_n^\star\right) + \lambda_{v_\theta}\cos\alpha_n^\star\sin\alpha_n^\star\right] \\
\dot{\lambda_\theta} &= 0 \\
\dot{\lambda_{v_r}} &= -\lambda_r + \frac{\lambda_{v_\theta} v_\theta}{r} \\
\dot{\lambda_{v_\theta}} &= -\frac{\lambda_\theta}{r} - \frac{2\lambda_{v_r} v_\theta}{r} + \frac{\lambda_{v_\theta} v_r}{r} \\
r(0) &= r_\oplus \\
\theta(0) &= 0 \\
v_r(0) &= 0 \\
v_\theta(0) &= v_\oplus \\
r(t_f) &= r_i \\
\lambda_\theta(t_f) &= 0 \\
v_r(t_f) &= 0 \\
v_\theta(t_f) &= v_i \\
H(t_f) &= -1
\end{aligned}
\tag{3.27}
$$

where $\{\tau^\star, \alpha_n^\star\}$ are given by (3.25).

The benefits of developing this indirect approach is that we can now infer how the optimal solution looks like. Specially, we have learned that α_n does not surpass $\approx 55^\circ$, and thus, it does not saturate at any point of the orbit. But most importantly, we discovered that the control strategy of τ is of the type bang-bang, due to its linear relation with the Hamiltonian. That explains, as mentioned in Chapter 2.2.1, why τ is often defined as an on/off switch parameter, with "on" meaning maximum thrust and "off" to account for coasting arcs. This on/off switch is considered instantaneous, so we are assuming that we have inertialess actuators that can act instantaneously. In reality, this is obviously not true, but the time scales are so different that, effectively, comparing to years (duration of typical orbit transfers [26]), a typical settling time for attitude control in the order of minutes [21] is, for all effects, instantaneous.

In the next section, we determine (local) optimal transfer orbits between the Earth and Mars/Jupiter. We have to check for the bang-bang structure in τ in the solutions obtained. Finding it does not mean that our solution is globally optimal, since local minima can present similar behaviour, but not finding it is enough to guarantee that the solution is not optimal.

3.3 Direct approaches for OCPs

In this section we develop a formulation of the problem that lets us solve it using Non Linear Programming (NLP) optimization algorithms. Then, we solve our OCP problem using this approach, and analyze the solutions obtained. The reason this method is used to find a solution instead of the indirect TPBVP developed above is because direct methods tend to have a greater region of convergence [33], thus it is easier to obtain a feasible initial guess that leads to a solution. In fact, if one wants to solve an OCP with an indirect approach, some authors first estimate a solution using direct methods, and even then use genetic algorithms to make a first estimation of adjoint variables [17], to make the TPBVP converge.

3.3.1 Transforming our OCP to a NLP problem. Direct Transcription

If we want to solve our OCP by a direct approach, it is mandatory that we transform it to the form of a problem that can be solved by a NLP optimization algorithm. To do this, it is necessary to know the standard formulation of NLP problems.

We first need to have a finite set of variables,. Therefore, a discretization of the problem is needed. Defining our set of unknown variables as $\boldsymbol{y} = [y_1, y_2, ..., y_M]^\intercal$, the generic NLP problem is normally formulated as an optimization problem in which we want to minimize a scalar objective function F as

$$\min_{\boldsymbol{y}} \quad F(\boldsymbol{y}) \tag{3.28}$$

These variables are subject to a set of inequality constraints and bounds represented as

$$\text{subject to} \quad \begin{cases} \boldsymbol{c}_L \leqslant \boldsymbol{c}(\boldsymbol{y}) \leqslant \boldsymbol{c}_U \\ \boldsymbol{y}_L \leqslant \boldsymbol{y} \leqslant \boldsymbol{y}_U \end{cases} \tag{3.29}$$

Equality path constraints and variable bounds can be included by making lower and upper limit accordingly ($c_{L_i} = c_{U_i}$ or $y_{L_j} = y_{U_j}$). We can see that this formulation is quite similar to the OPC, with key differences. The first one is that it deals with a finite set of unknown, and the other is that it does not leave room to include differential equations, since we are no longer working in a continuum.

To adapt our OCP to this formulation, we must discretize time in a number of intervals

$$\boldsymbol{t} = \left[0 = t_0, t_1, ..., t_N = t_f\right]^\intercal, \quad \text{where} \quad t_{k+1} = t_k + h, \quad \forall k \in [0, N-1] \tag{3.30}$$

In (3.30), h is given by $h = t_f/N$. Note that we have here made a uniform discretization of the time domain. This is a totally logical approach, since we do not know anything of the problem solution yet, other than that possibly thrust parameter τ has a bang-bang behaviour. Using a uniform time partition approach is common in trajectory optimization related problems [34]. Some projects go beyond that and once they have solved the problem they use the solution to refine the time mesh and rerun the NLP algorithm again, with the aim of obtaining a more precise solution [35]. In this project we stick to this uniform distribution for time discretization. Refining mesh in posterior iterations is proposed as future work.

Given that now we have a finite number of time instants, our set of unknowns has also become finite. At each instance of time k of the N+1 total count, we have four state variables $\boldsymbol{x}_k$. Also, for simplicity, we choose the parameter controls to be constant functions in between each time interval, therefore, we have two control variables $\boldsymbol{u}$ at every interval of the N total count. There are other options, for example, we could have defined $\boldsymbol{u}$ at every instant of time, and define any value in between by linearly interpolating. In this particular problem, since final time is unknown, we have to add it to the vector of variables $\boldsymbol{y}$. So, in total, assuming that time is partitioned in N intervals, we have n_x state variables, n_u control parameters, and 1 unknown time variable, the total amount of unknowns in our NLP problem can be expressed as

$$n_T = n_x \cdot (N+1) + n_u \cdot N + 1 \tag{3.31}$$

For our problem, we are opting for a time partition of 500 intervals, amounting to a total of 3005 variables, a good compromise between precision and speed when it comes to solving the OCP.

For a discretized version of the OCP, we now have to transform the state differential equations in (2.21) into their algebraic finite differences equivalents. These new algebraic constraints are often called defect constraints. To do so, we must be able to approximate the next value of a state variable depending on previous values of $\boldsymbol{x}$ and $\boldsymbol{u}$, bu using some defined numerical integration method. For a classical Runge-Kutta method of order s, this relation can be expressed as $\boldsymbol{x}_{i+1} = \boldsymbol{x}_i + h\sum_{i=1}^{s} b_i \boldsymbol{k}_i$, better expressed as a defect constraint as

$$\boldsymbol{\zeta}_k = \boldsymbol{x}_{k+1} - \boldsymbol{x}_k - h\sum_{i=1}^{s} b_i \boldsymbol{k}_i \tag{3.32}$$

With b_i being coefficients and $\boldsymbol{k}_i$ midpoint state functions evaluations depending on the particular method scheme utilized. Since there are N time intervals, and n_x state variables, we have a total of $N = 500$, $n_x = 4$

resulting in $n_\zeta = 2000$ defect constraints.

The particular numerical integration method used in this project is the Classical Runge Kutta Fourth Order method, represented in table 3.1.

Table 3.1 Classic Runge Kutta scheme.

0				
1/2	1/2			
1/2	0	1/2		
1	0	0	1	
	1/6	1/3	1/3	1/6

Algebraically, this scheme can be represented by the equations in (3.33). Time-dependence is not necessary since none of the equations depends explicitly on time, and $\boldsymbol{u}_k$ does not change in those formulas since it has been chosen to remain constant in between each time interval.

$$\begin{aligned}
\boldsymbol{k}_{1_k} &= \boldsymbol{f}\left(\boldsymbol{x}_k, \boldsymbol{u}_k\right) \\
\boldsymbol{k}_{2_k} &= \boldsymbol{f}\left(\boldsymbol{x}_k + \frac{h}{2}\boldsymbol{k}_{1_k}, \boldsymbol{u}_k\right) \\
\boldsymbol{k}_{3_k} &= \boldsymbol{f}\left(\boldsymbol{x}_k + \frac{h}{2}\boldsymbol{k}_{2_k}, \boldsymbol{u}_k\right) \\
\boldsymbol{k}_{4_k} &= \boldsymbol{f}\left(\boldsymbol{x}_k + +h\boldsymbol{k}_{3_k}, \boldsymbol{u}_k\right) \\
\boldsymbol{x}_{k+1} &= \boldsymbol{x}_k + \frac{h}{6}\boldsymbol{k}_{1_k} + \frac{h}{3}\boldsymbol{k}_{2_k} + \frac{h}{3}\boldsymbol{k}_{3_k} + \frac{h}{6}\boldsymbol{k}_{4_k}
\end{aligned} \tag{3.33}$$

This integration technique is good enough for our purposes in this project, since it represents a good compromise between accuracy and simplicity. However, for more advanced applications, there exist better integration methods, that compute extremely accurate approximations by adequately choosing the nodes and collocation points in each time interval [36].

A visual scheme of direct transcription is presented in figure 3.4 for the case in which there is only one state variable x and one control parameter u. In it, we can see how these variables are discretized in each given instant of time. For each instance k, a numerical integration technique (in our case a Classic Runge Kutta scheme) is utilized to approximate x_{k+1}. During that interval, u_k remains constant. It is now clearly visualized why for a given discretization in N time intervals, we have N+1 variables of x and N variables of u.

Apart from the equations already mentioned, we still have the inequality path constraints that account for the maximum and minimum value for τ and α_n, now defined for each interval. They are expressed as

$$\begin{aligned}
0 \leqslant &\tau_k \leqslant 1 \\
-\alpha_n^{max} \leqslant &\alpha_{n_k} \leqslant \alpha_n^{max}
\end{aligned} \qquad \forall k \in [0, N-1] \tag{3.34}$$

Our boundary conditions can also easily be transformed into their discrete version, as presented in

$$\begin{aligned}
r_0 &= r_\oplus \\
\theta_0 &= 0 \\
v_{r_0} &= 0 \\
v_{\theta_0} &= v_\oplus \\
r_N &= r_i \\
v_{r_N} &= 0 \\
v_{\theta_N} &= v_i
\end{aligned} \tag{3.35}$$

Where again, $i = \mathrm{♂}, ⅗$ depending whether we refer to Mars or Jupiter. There is also the final time positive constraint commented in Chapter 3.1.2, $t_f \geqslant 0$. We are now finally to describe the full problem in a NLP formulation:

$$
\begin{aligned}
&\min_{\boldsymbol{y}} \quad t_N \\
&\text{subject to} \quad \begin{cases} \boldsymbol{c}_L \leqslant \boldsymbol{c}(\boldsymbol{y}) \leqslant \boldsymbol{c}_U \\ \\ \boldsymbol{y}_L \leqslant \ \boldsymbol{y} \ \leqslant \boldsymbol{y}_U \end{cases} \\
&\text{where} \\
&\boldsymbol{y} = \left[r_0, \theta_0, v_{r_0}, v_{\theta_0}, r_1, \theta_1, v_{r_1}, v_{\theta_1}, ..., r_{N-1}, \theta_{N-1}, v_{r_{N-1}}, v_{\theta_{N-1}}, r_N, \theta_N, v_{r_N}, v_{\theta_N}, \tau_0, \alpha_{n_0}, ..., \tau_{N-1}, \alpha_{n_{N-1}}, t_N \right]^\intercal \\
&\boldsymbol{y}_L = [r_\oplus, 0\ , 0\ , v_\oplus\ , -, -\ , -\ , -\ , -\ , ...,\ -\ ,\ -\ ,\ -\ ,\ -\ , r_i\ , -\ ,\ 0\ , v_i, 0, -\alpha_n^{max}, ...,\ 0\ , -\alpha_n^{max},\ 0\ ]^\intercal \\
&\boldsymbol{y}_U = [r_\oplus, 0\ , 0\ , v_\oplus\ , -, -\ , -\ , -\ , -\ , ...,\ -\ ,\ -\ ,\ -\ ,\ -\ , r_i\ , -\ ,\ 0\ , v_i, 1, \alpha_n^{max}\ , ...,\ 1\ ,\ \alpha_n^{max}\ , -\ ]^\intercal \\
&\text{and} \\
&\boldsymbol{c}(\boldsymbol{y}) = \left[\zeta_0, \zeta_1, ..., \zeta_{N-1}, \zeta_N \right]^\intercal \\
&\boldsymbol{c}_L = [\ 0\ ,\ 0\ , ...,\ \ 0\ \ ,\ 0\ ]^\intercal \\
&\boldsymbol{c}_U = [\ 0\ ,\ 0\ , ...,\ \ 0\ \ ,\ 0\ ]^\intercal
\end{aligned}
\tag{3.36}
$$

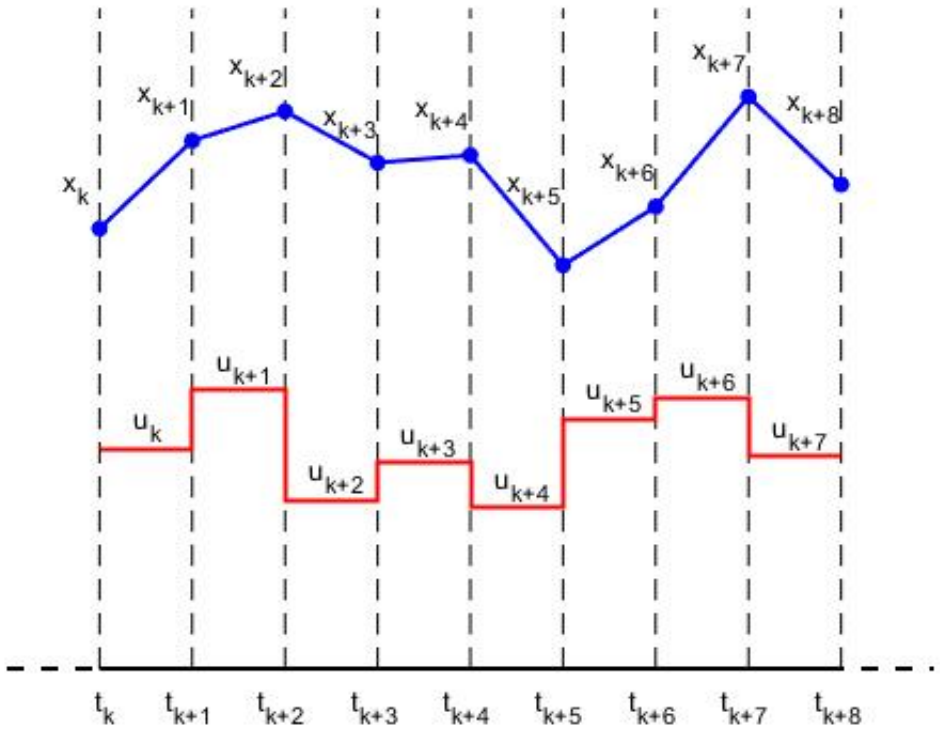

Figure 3.4 Visual representation of Direct Transcription of an Optimal Control Problem.

The notation $-$ in a term of a vector simply means that there is not such restriction. For example, in the position of t_N there is a $-$ in the upper bound because t_N is limited to be greater than 0, but nothing is said about its maximum value.

Having set up the problem in a NLP form, it is now time to use an optimization algorithm to solve it. We opt to use the *CasADi* Toolbox for MATLAB [37], since it lets us utilize the widely spread algorithm IPOPT (Interior Point OPTimizer), commonly used for large scale non linear optimization of continuous systems, and it also lets us define the problem in a more natural way.

IPOPT is a deterministic algorithm when it is dealing with convex constraints and a convex cost function in a convex domain. With those assumptions, the problem has only a local extremum (which logically coincides with the global), and IPOPT is able to find it rapidly. However, non-convex optimization is more challenging. There exist multiple local extrema, and it is not rare to end with an infeasible output from the algorithm since it is not able to find a solution if the initial guess is not close enough to it. Even with those limitations, IPOPT is able to come up with a solution in many cases, making it very versatile. It is said that for non-convex optimization, IPOPT is an heuristic algorithm, that sacrifices optimality, accuracy, precision, and/or completeness for speed. There is not a standardized procedure to ensure that the solution is a global extremum, and occasionally it becomes rather challenging to find it. One thing that can be done is to change the initial orbit guess several times, and see how that affects the result. If the optimal transfer time remains the same for a variety of different initial guesses, we can be confident that the solution is globally optimal. Otherwise, if the result changes, our best option is to choose the orbit that has less transfer time than the rest; even if we can not ensure that this result is the global minimum, it is probably not far from it.

Also, as mentioned in Chapter 3.2, a bang-bang structure is expected for the thrust lever parameter τ. This behaviour is common in problems of this type, specially if we are dealing with time-optimal solutions. We have seen the mathematical explanation of why the control law is of bang-bang type, however, there is an intuitive way to think of it. We can imagine a car that wants to travel a fixed distance in the least time possible, and starting and ending with zero velocity. The optimal and obvious strategy is to go full throttle since the start, and the release it fully and break hard at the instant necessary that makes the car reach that fixed distance with zero velocity. Consequently, the same rapidly changing bang-bang behaviour between maximum and minimum control values appears in this simple problem too, and its emergence seems natural.

3.3.2 Strengthening arrival conditions and varying characteristic acceleration

Prior to defining the optimal transfer orbits between Earth and Mars, and Earth and Jupiter, we first compute the time-optimal solution to Jupiter obtained ignoring the final velocity constraints. That is, we only care about reaching Jupiter's circular orbit as fast as possible, ignoring the arrival velocity. Solving the problem in various steps helps us to build intuition for what orbit to expect in the complete problem. The reason why we do these simulations with Jupiter first is because, being Jupiter further away from the Earth, it is easier to observe the phenomena that we want to emphasize. Moreover, Jupiter is a more demanding NLP problem, since the mission takes longer and is more sensible to changes in variables. Being able to solve these problems for the case of Jupiter prepares us for the next chapter.

In figure 3.5, the solution to the fastest orbit to Jupiter with no velocity constraints is presented, along with the evolution with time of state variables and control parameters. As expected, a bang-bang structure is encountered for τ. It is clearly visible in the time evolution of the variables that the best strategy to reach Jupiter as fast as possible is to coast when we are far from the Sun, so we can come again closer to it, and then go full throttle. This strategy may seem arbitrary at first, but it is taking advantage of a well known phenomenon in orbital mechanics, the Oberth effect. It states that, for a given increment of velocity Δv, the kinetic energy of the spacecraft increases more if it is traveling at a faster speed. In simple words, it is more productive to accelerate near massive bodies. That, joined to the fact that the Esail thrust is also greater near the Sun, constitute sufficient reasons to explain this behaviour. We reach Jupiter in less than seven years, a rather optimistic result, that will get worse as we add arrival velocity limitations.

An interesting remark is the evolution of the sail pitch angle α_n when we are in a coasting arc. As one can guess, this distribution does not really make a difference, since sines and cosines are then multiplied by

0 (thrust is off). The evolution that the algorithm calculates is then relatively arbitrary, and therefore it has been erased in figure 3.5, not showing α_n when we are in a coasting arc. During those periods, it may be beneficial to position the Esail perpendicular to the Sun, and try to gather as much solar energy as possible.

The next step is to add an extra constraint to our problem, arriving with zero radial velocity (tangent to the planet), even if our tangential velocity does not match the planet's speed. The new results are presented in figure 3.6.

Again, a bang-bang structure is found in thrust lever τ, as expected. We can see that the strategy followed now is not particularly different, the algorithm just finds the optimal intervals to coast in order to reach Jupiter as rapidly as possible, while still benefiting from the Oberth effect. We now reach Jupiter in roughly seven and a half years, definitely an increment with respect to the last example, but maybe not as big as expected. In a real scenario, even if we reach Jupiter with a tangent orbit, this transfer is not desirable, since the difference in velocities between the spacecraft and Jupiter is too large to make the spacecraft stay in a Jupiter centered orbit.

We solve one more problem now changing roles. We do not care now about reaching Jupiter in a tangential orbit, but rather with the same velocity. Therefore, the condition $v_{r_f}^2 + v_{\theta_f}^2 = v_{\mathcal{U}}^2$ is now imposed. The results of this problem are displayed in figure 3.7.

In this problem, considering the same arrival velocity modulus, we can again see Oberth effect and bang-bang structure in action. Flight time is now almost eight years, again, not really a noticeable change with respect to previous cases. As in the example above, even if we reach Jupiter with its same speed, this transfer orbit is not desirable. In practice, the arrival flight path angle is too large to make the spacecraft stay in any Jupiter centered orbit.

Lastly, we tackle the complete problem, reaching Jupiter with zero radial speed and its same tangential velocity, accomplishing a circular-circular rendezvous, as originally wanted. Results are presented in figure 3.8.

The complete problem differs significantly from the previous ones. Flight duration is now roughly fifteen years, a 200% increase with respect to the scenarios proposed above. The Oberth effect is not as exploited now, and coasting arc periods are significantly shorter. We can then argue that the complexity of the problem does not come from the condition of arriving with zero radial speed, nor arriving with the same speed modulus as the planet, but rather comes from combining these two criteria to satisfy the rendezvous arrival constraints. This is the reference trajectory that we use for Jupiter in the next chapter, where solar wind perturbations are introduced.

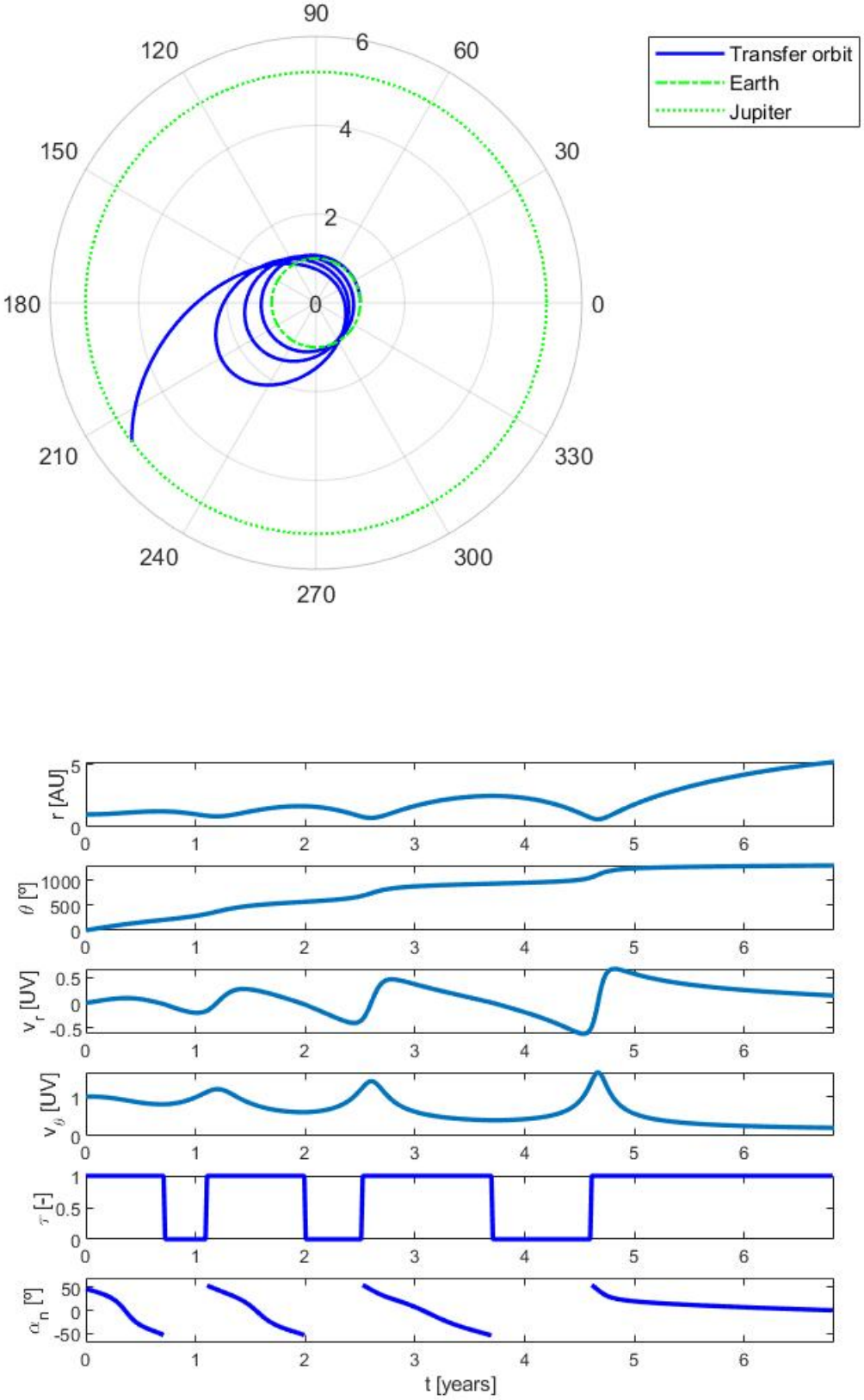

Figure 3.5 Trajectory and evolution of variables in a transfer orbit to Jupiter ignoring arrival velocity constraints for $a_c = 0.36$ mm/s^2.

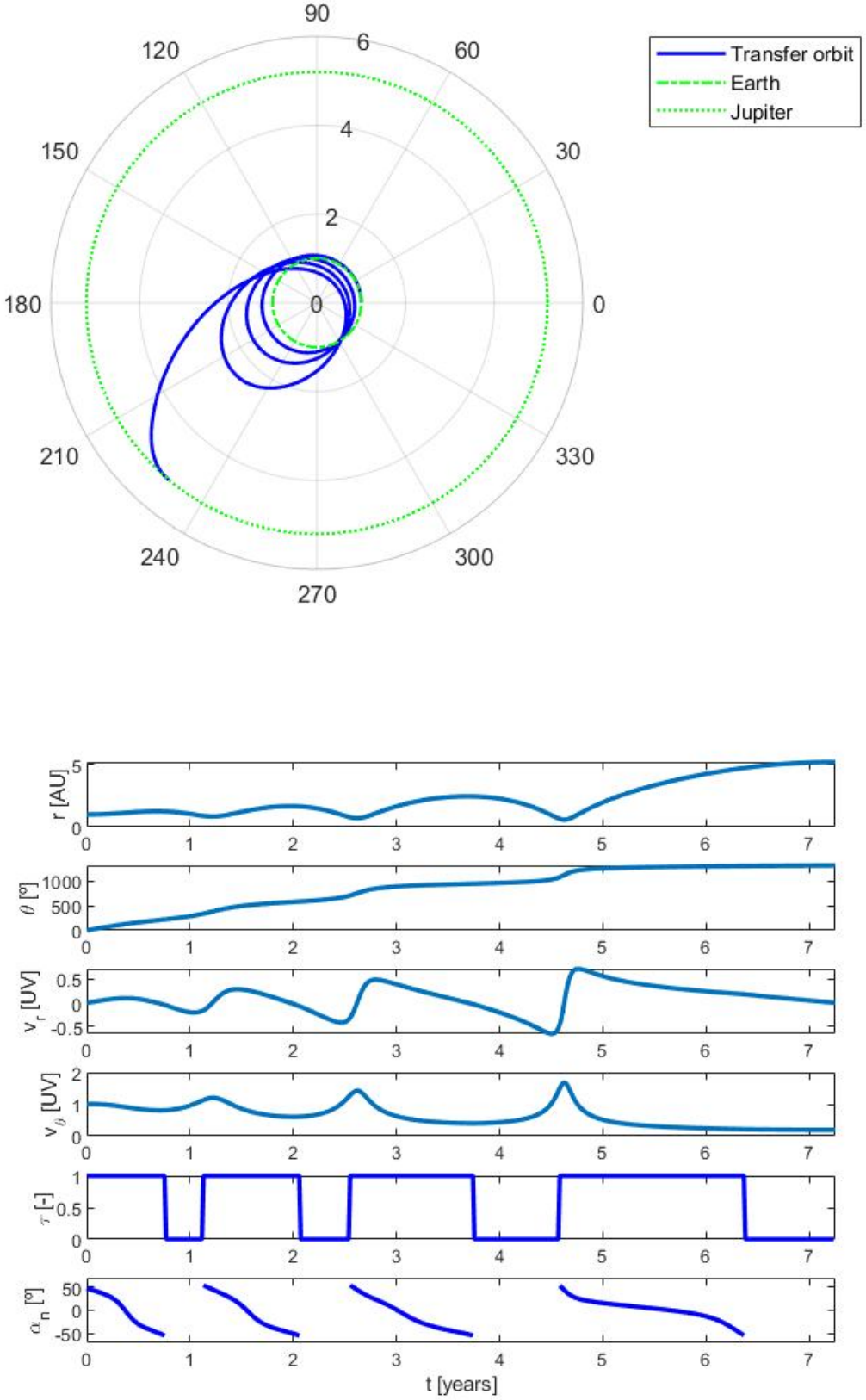

Figure 3.6 Trajectory and evolution of variables in a transfer orbit to Jupiter considering zero arrival radial velocity for $a_c = 0.36$ mm/s^2.

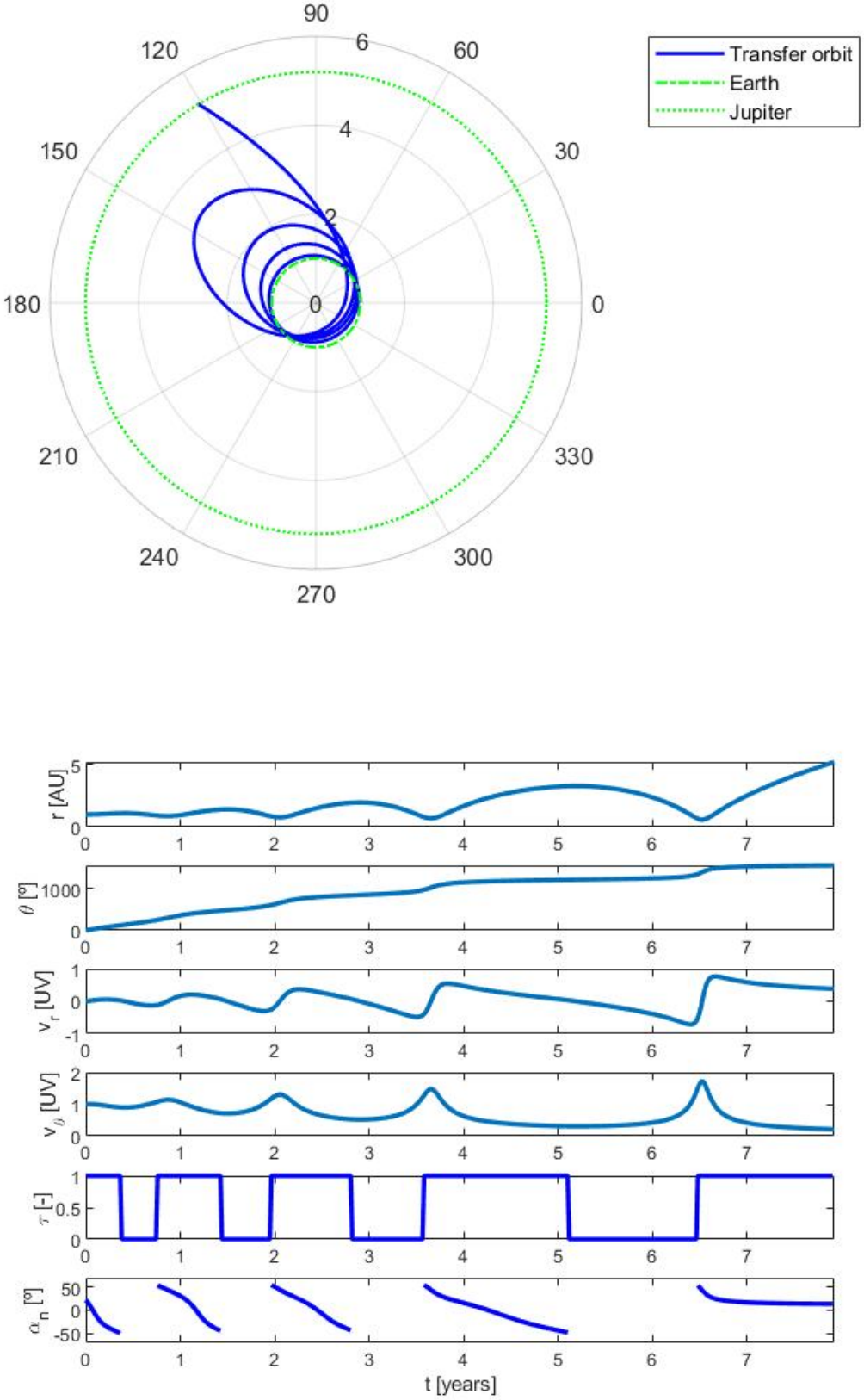

Figure 3.7 Trajectory and evolution of variables in a transfer orbit to Jupiter considering equal arrival velocity modulus for $a_c = 0.36$ mm/s^2.

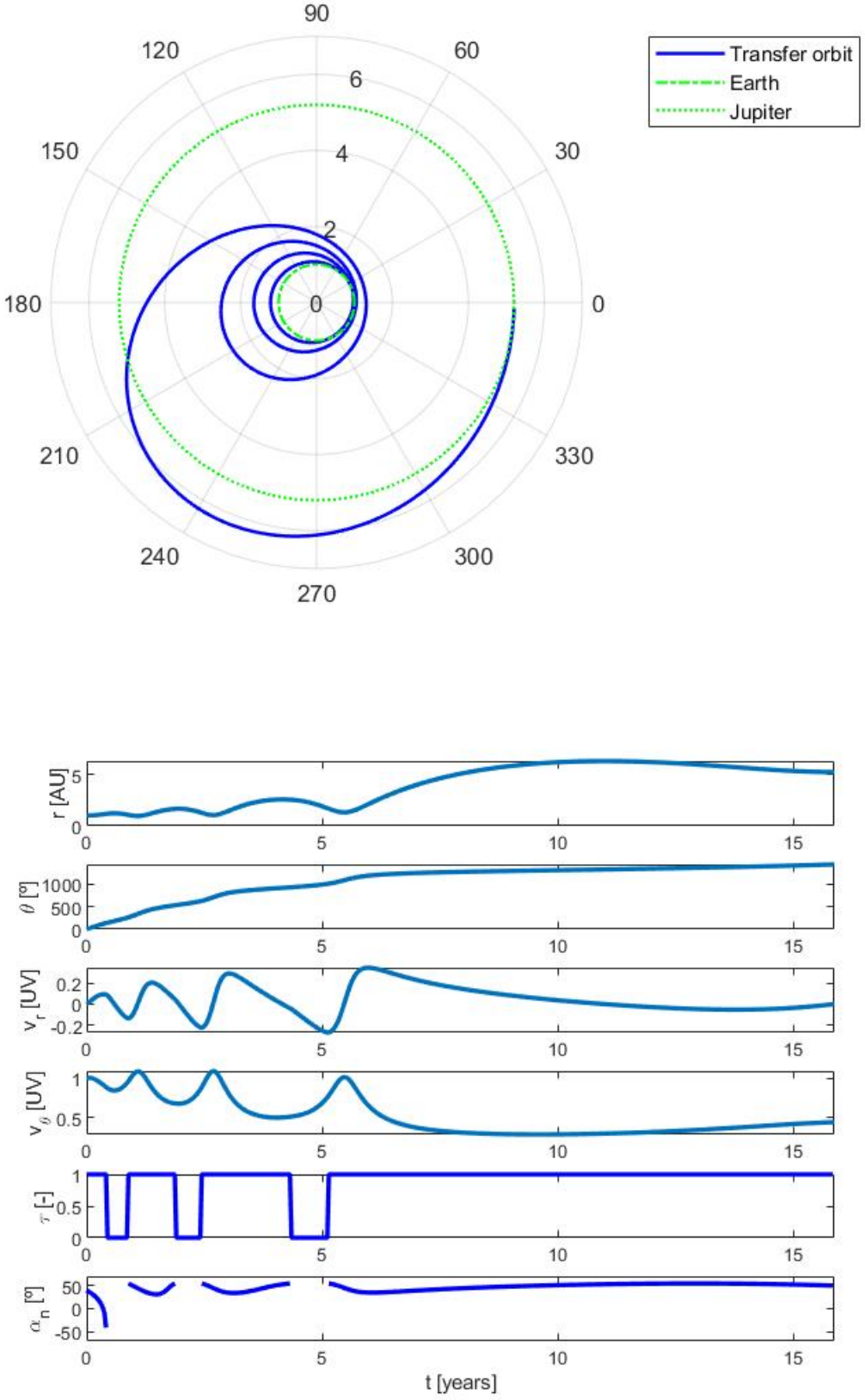

Figure 3.8 Trajectory and evolution of variables in a transfer orbit to Jupiter considering arrival rendezvous for $a_c = 0.36$ mm/s^2.

Next, we discuss the solution for a couple of different characteristic accelerations. All the four previous trajectories were computed with a characteristic acceleration of $a_c = 0.36$ mm/s^2. In figure 3.9, results for a characteristic acceleration of 0.1mm/s^2 are shown.

Now, since the propulsion capacity is substantially lower, the spacecraft has to complete several more revolutions until it is able to reach Jupiter. This problem is remarkably harder to solve than the previous ones, and that is due to the amount of loops the spacecraft makes around the Sun. It makes the problem much more sensible to the initial guess. Time has now been discretized in 1000 intervals instead of 500 to account for the much longer trajectory. Flight duration is now almost 50 years, considerably higher than in the last example. An Esail of these characteristics is not really applicable, this example is proposed only to develop intuition. The sudden discontinuities seen in τ probably are a result of the problem discretization, and with a finer mesh we can expect them to disappear, leaving thrust modulus constant and varying the orbit using exclusively the sail pitch angle. This is common in low-thrust orbits, where flight time is so large that there is no room for coasting arcs.

One more example for a typical characteristic acceleration of $a_c = 1$ mm/s^2 is shown in figure 3.10. This resulting orbit differs from the others. We can clearly see that there are intervals in which the variation of the thrust lever is continuous, breaking the bang-bang control trend previously mentioned. This indicates us that the obtained solution must not be the global minimum, but rather a local one. Bang-bang control is not simply a behaviour we are expecting because of some intuition, it has been proven in Chapter 3.2 that, in order for the solution to be optimal, this control law needs to be followed. A reason of why IPOPT obtains this solution is not totally clear. Many different first guesses have been tested and all them converge to this one. It appears that this scenario is particularly sensitive to the initial guess, although having proven many of them shows that, even if we are not obtaining the global optimal solution, we are probably not far from it. For this case, one may try indirect approaches to come up with the global optimal solution, or at least a local one that exhibits bang-bang behaviour, which is a sign that the local solution obtained is not far from the global. We, however, do not worry about this phenomenon, since the acceleration we use for the reference orbit is, as mentioned $a_c = 0.36$ mm/s^2, corresponding to figure 3.8.

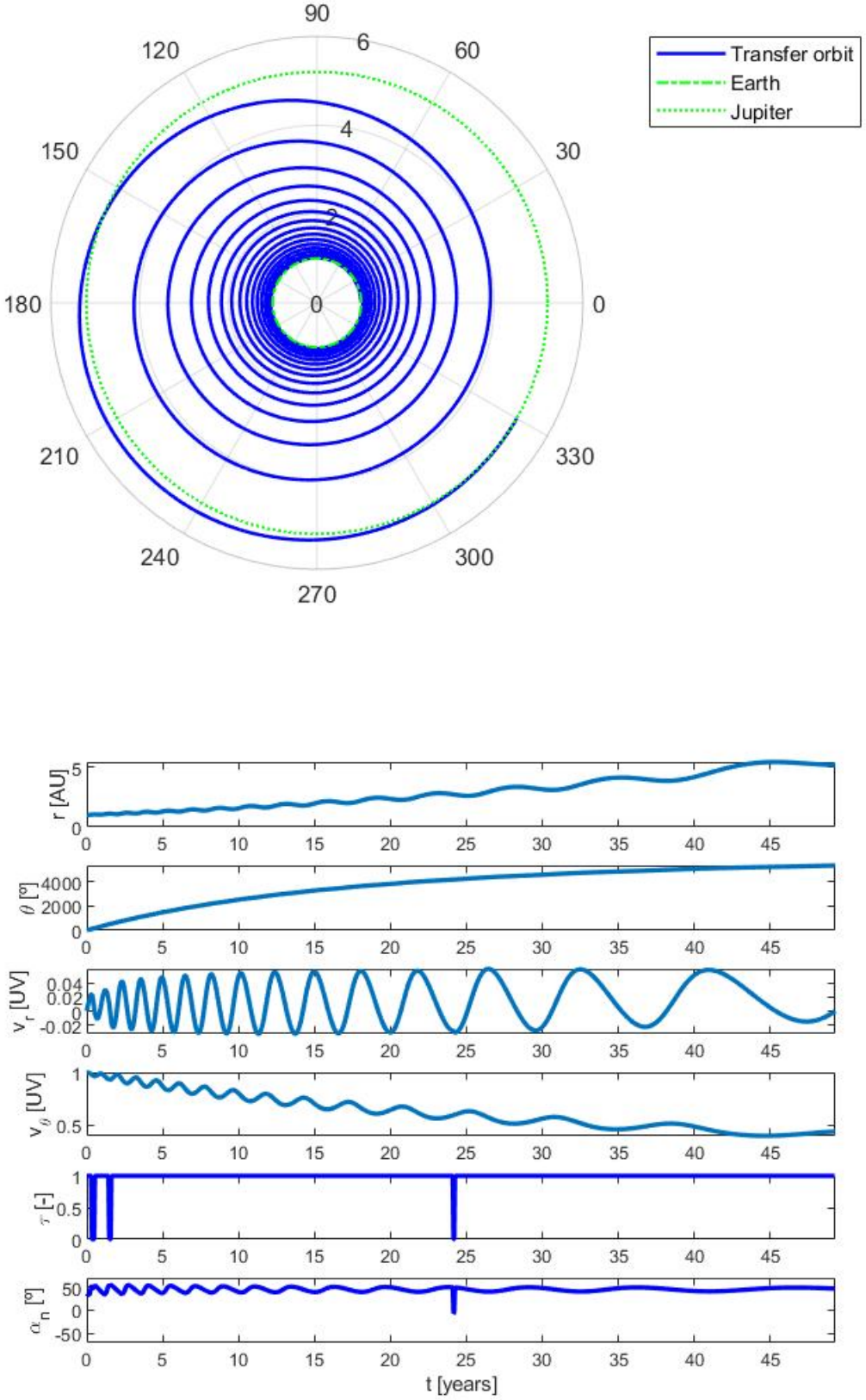

Figure 3.9 Trajectory and evolution of variables in a transfer orbit to Jupiter considering arrival rendezvous for $a_c = 0.1$ mm/s^2.

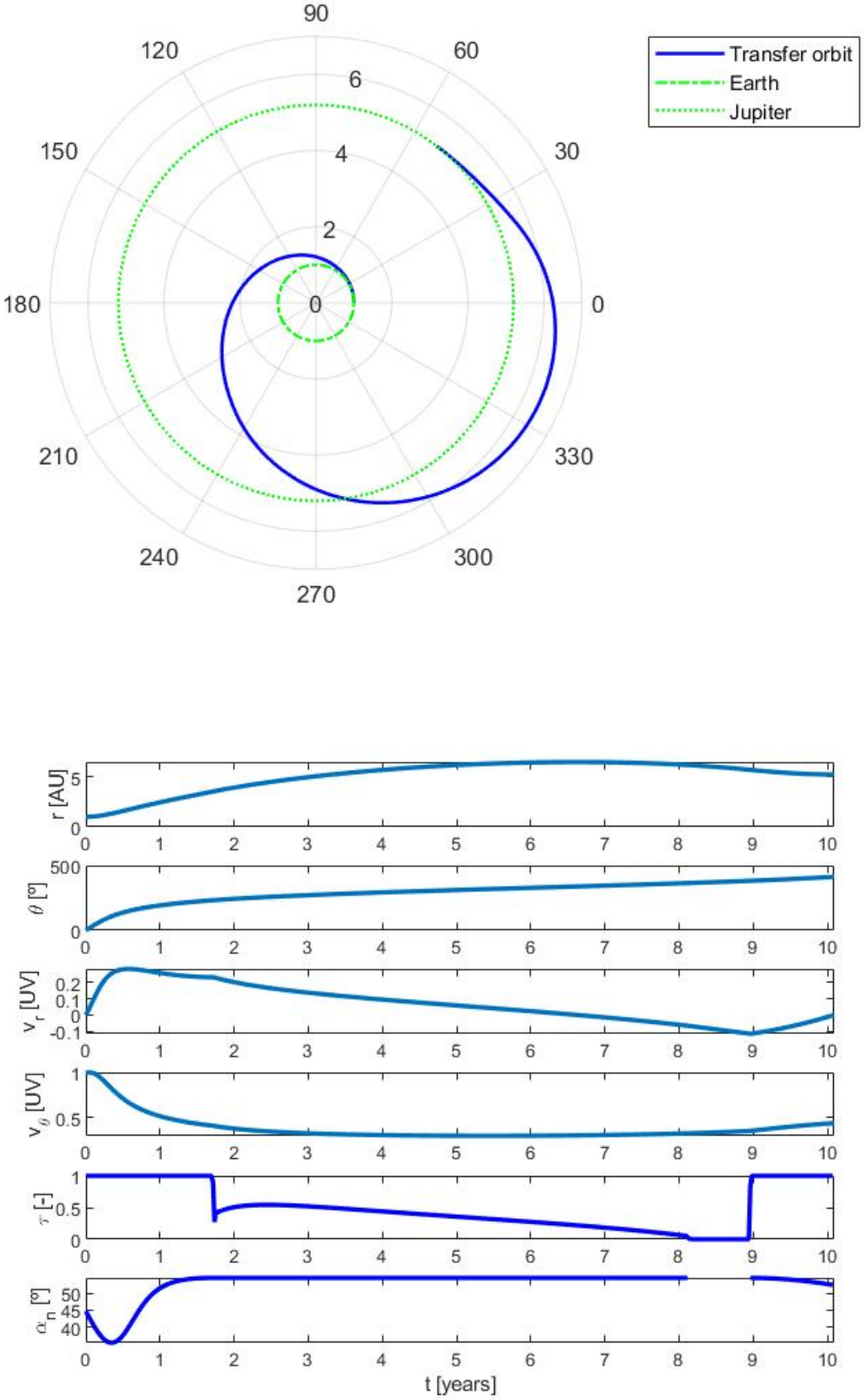

Figure 3.10 Trajectory and evolution of variables in a transfer orbit to Jupiter considering arrival rendezvous for $a_c = 1$ mm/s^2.

To test the truthfulness of our results, we compute the transfer orbit from the Earth to Mars with a characteristic acceleration of 1 mm/s^2 with rendezvous arrival conditions. The reason to do so is because Mars is a more typical mission target than Jupiter, and that fact, along with the usage of a characteristic acceleration of 1 mm/s^2, which, as mentioned in Chapter 2.2.2 is usually utilized, lets us check how much our values differ from the ones obtained by others. Missions to Jupiter or farther planets are not often studied because of their increasing complexity when it comes to solving for the time optimal transfer orbit. [17] is an exception, where they study possible orbits for outer solar system exploration. However, normally missions with closer orbits such as a rendezvous with Apophis [38] or 1998 KY26 [16] are more common.

The trajectory and time evolution of the variables can be seen in figure 3.11. We obtain a flight duration of 520 days. We can compare this value to the ones obtained in [39] and [38], although there are some subtle differences. In the first one, the thrust model, although very similar to the more recent one used here, slightly overestimates the value of γ for a given α_n, therefore, mildly better results are expected. In the second one, the same propulsive model as in this project is used, but it is only assumed that the orbits are coplanar, not circular. The initial angle of departure θ_0 is left as an extra unknown. Consequently, the program finds the best launch date, where the Earth and Mars are best positioned taking into account their eccentricity and phase angle. Due to this extra degree of freedom, we also expect flight time to be slightly lower. For clarity sake, we refer to [39] as *Old model*, and to [38] as *Non circular orbits*. The results are presented in table 3.2.

Table 3.2 Flight time comparison for a rendezvous mission to Mars with $a_c = 1$ mm/s^2.

Study	Old model	Non circular orbits	This project
Flight time [days]	500	470	520

Considering the differences explained above between both studies and our scenario, the results are surprisingly similar. Both studies show slightly better results than ours, but that, at least partly, is due to the hypotheses there considered. That means that we can be confident about our resolution method, since it yields realistic results.

One last thing to notice is that, as predicted in Chapter 2.2.1, the sail pitch angle never surpasses $\alpha_n = \arccos\left(\frac{1}{\sqrt{3}}\right) \approx 55^\circ$.

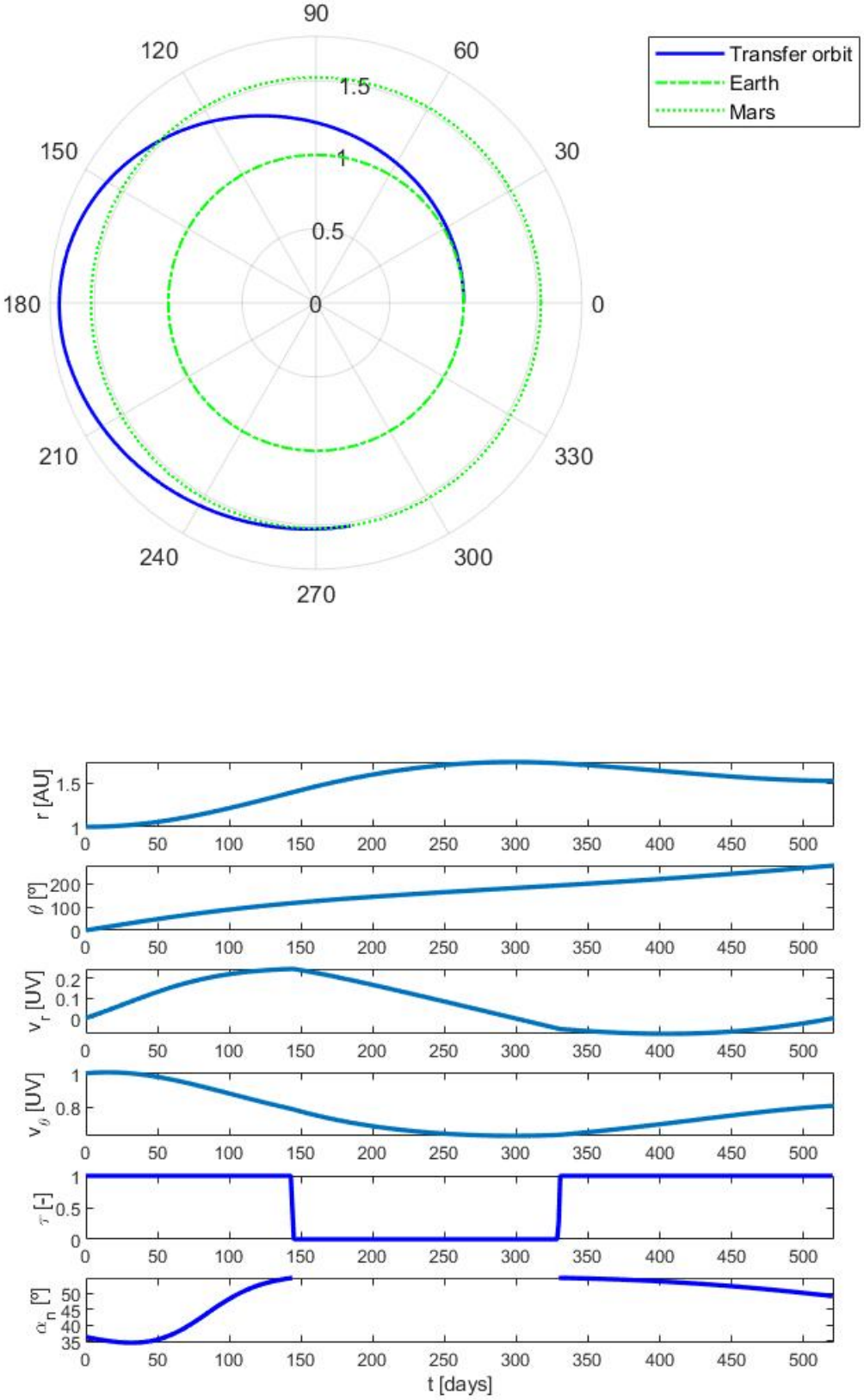

Figure 3.11 Trajectory and evolution of variables in a transfer orbit to Mars considering arrival rendezvous for $a_c = 1$ mm/s^2.

3.3.3 Optimal transfer for Mars. Comparison with indirect methods

This section sets the reference trajectories used in the next chapter for the closed loop guidance strategy. The optimal transfer to Jupiter is already presented in figure 3.8, lasting slightly more than fifteen years. The trajectory used as reference for the Earth-Mars transfer is shown in figure 3.12, lasting for roughly 1000 days or ~ 2.7 years, and presenting only one coasting arc.

In this section we also present a comparison between this solution obtained using direct transcriptions with respect to the solution obtained by solving the TPBVP using MATLAB's function `bvp4c`, which solves the boundary problem by implementing the three-stage Lobatto IIIa formula. These results using the indirect approach have been obtained in the final stages of the project, and therefore are not the ones used for the guidance strategies in the next Chapter. However, it is still interesting to show them, as they provide a way to compare the solution performance between different methods.

As it was stated at the start of this chapter, indirect approaches are known for being harder to solve. They require an exceptionally good first guess, which must be near to the final solution, otherwise the algorithm does not converge. The challenge is that, even if we know how the solution looks like given that we have obtained it from direct methods, the evolution of the costate variables is still unknown. However, we can still obtain some information about them. From (3.27), looking at the differential equation and final condition of λ_θ, we can clearly infer that the time evolution of this multiplier is $\lambda_\theta(t) = 0$. Moreover, we can see in figure 3.12 that α_n starts being approximately 35°. Recalling the optimal control laws in (3.25), we can deduce that the initial values of λ_{v_r} and λ_{v_θ} must follow the equation $\lambda_{v_\theta}(0)/\lambda_{v_r}(0) \approx -3$, with $\lambda_{v_\theta}(0) < 0$ and $\lambda_{v_r}(0) > 0$. Knowing this information, we are left with two degrees of freedom in the choice of the multipliers' initial values:

$$\begin{aligned} \lambda_r(t) &= p \\ \lambda_\theta(t) &= 0 \\ \lambda_{v_r}(t) &= q \\ \lambda_{v_\theta}(t) &= -3q \end{aligned} \tag{3.37}$$

where $p \in \mathbb{R}$ and $q \in \mathbb{R}^+$. To estimate these initial values, a manual shooting method approach has been used, varying the values of p and q until a solution that looks similar to the obtained using direct transcription is found. Then, these costate initial values are introduced as constant functions for the initial guess of `bvp4c`, achieving convergence and thus, the solution using an indirect approach, which differs slightly from the one previously obtained. For the indirect approach, time domain has also been uniformly discretized in 500 intervals.

The comparison of the solutions obtained between these two methods is shown in figure 3.13. We can see that the recently obtained solution using an indirect approach is 2% faster, confirming that our direct method solution was a local minimum instead of a global, as predicted. Nothing truly guarantees us that the solution obtained via indirect methods is the global optimum, but the fact that these two solutions are so close to each other is a strong argument to support that the global solution must not be considerably faster than these. In both trajectories, the coasting arc is initiated approximately at the same time, with the difference that with the indirect approach the sail pitch angle goes all the way down to its minimum value, and regains control of the spacecraft later, thus having a longer coasting arc. The evolution of the sail pitch angle after the coasting arc is similar in both trajectories, oscillating around the value of $\alpha_n = 45^\circ$, which is the one that yields maximum tangential acceleration as seen in Chapter 2.2.1.

There are different approaches to try to find the global optimum, although none of them is deterministic. Downhill Simplex, Genetic Algorithms or Simulated Annealing are examples of methods used for this purpose [40]. Moreover, there exist some functions combining various local minima, sharp variations and discontinuous derivatives used to test these methods. These are known as test functions [41]. The implementation of indirect methods for the rest of the trajectories presented, as well as the inclusion of these global approaches, are proposed as future work, to further reduce the mission flight time.

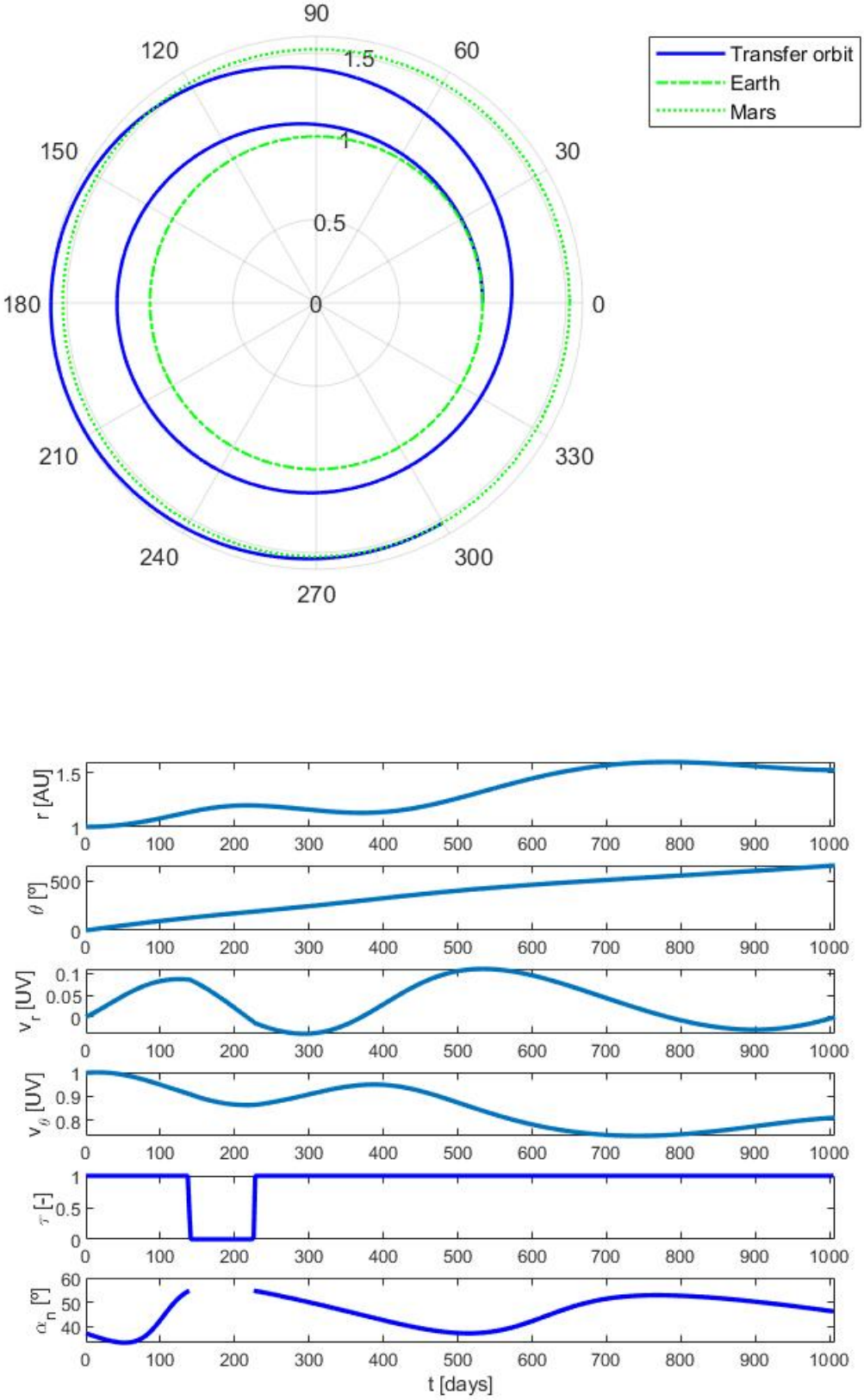

Figure 3.12 Trajectory and evolution of variables in a transfer orbit to Mars considering arrival rendezvous for $a_c = 0.36$ mm/s^2.

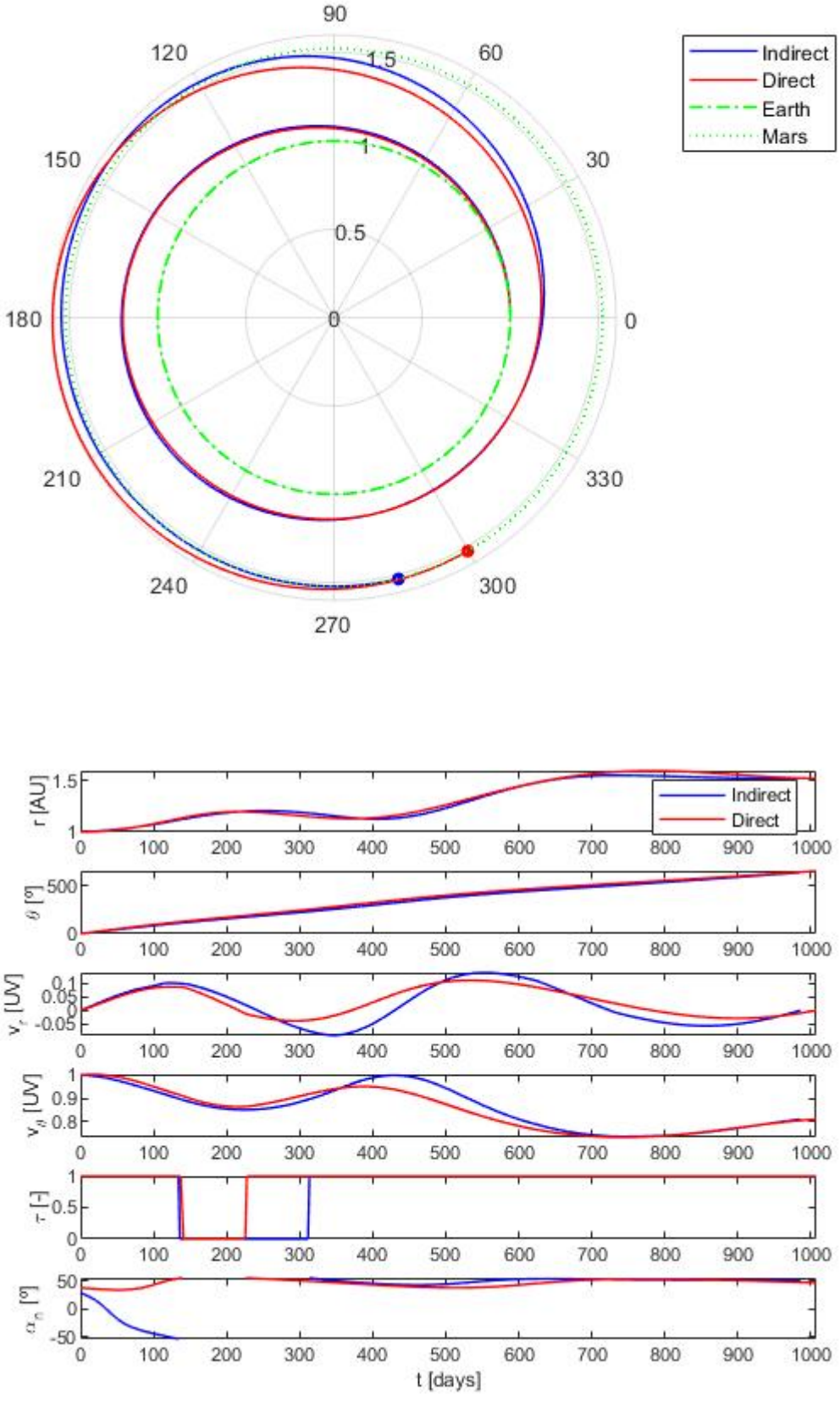

Figure 3.13 Trajectory and evolution of variables comparison between direct and indirect methods in a transfer orbit to Mars considering arrival rendezvous for $a_c = 0.36$ mm/s^2.

3.3.4 Parametric study of flight times

In this section we conduct a parametric study to obtain a general idea of the flight time dependence with the characteristic acceleration a_c and the distance to which we want to accomplish a circular-circular rendezvous. With previous thrust models, where α_n and α were supposed equal, it was interesting to also study the time dependence with the maximum pitch angle. However, with the new thrust model, the maximum α_n is estimated to be around 70°, even if, as already mentioned, there is no particular reason to go beyond $\approx 55^\circ$, and it has also been observed in the simulations made. Consequently, this study has not consider possible variations in α_n^{max}.

The values used for the characteristic acceleration and for the final orbit radius, as well as time results are visually presented in figure 3.14.

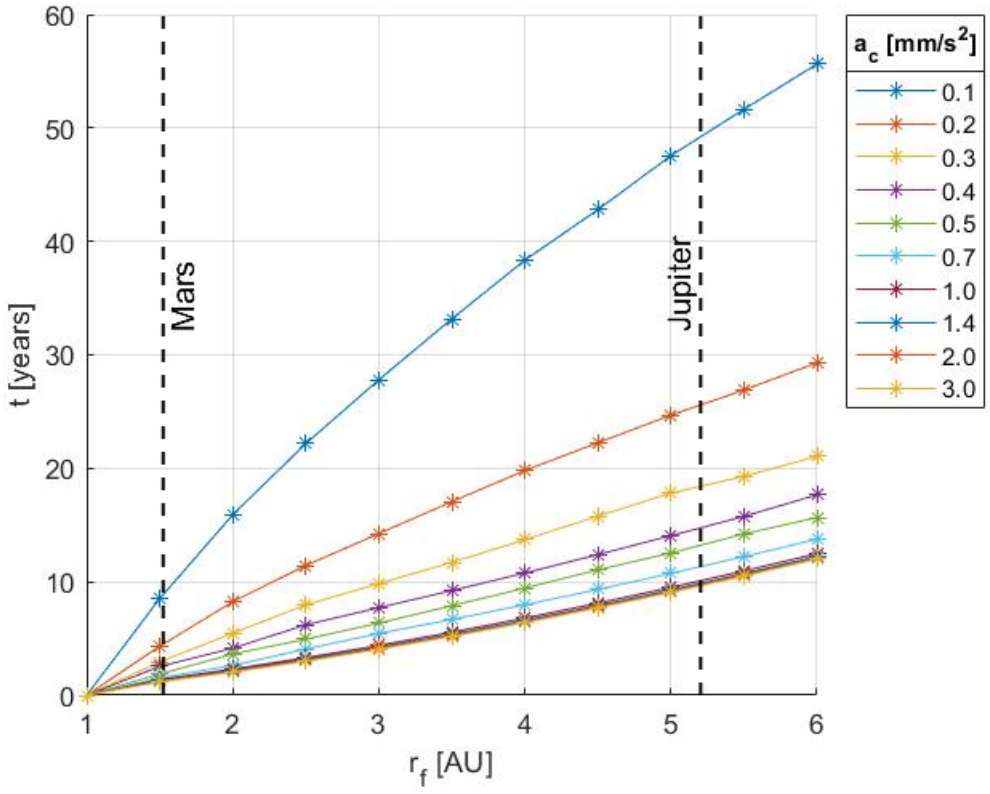

Figure 3.14 Parametric study of Esails flight time for different characteristic accelerations and final distances for circular-circular rendezvous.

It is interesting to observe that the evolution of flight time with respect to the final orbit radius is approximately linear, and the effect of a_c is principally noticeable in the slope of those linear approximations. This linear behaviour is more noticeable when r_f is big, since for smaller values coasting arcs become more relevant than propulsive capacity. Moreover, asymptotic behaviour is clearly observed when characteristic acceleration is increased. This is principally due to the limitation in thrust cone angle, which, as seen in Chapter 2.2.1, can not be 20° or greater. That, combined with the arrival velocity constraints for a circular-circular rendezvous encounter, makes the spacecraft go through long coasting arcs in order for it to reach its target correctly.

A zoomed version of the parametric plot for higher values of a_c is included in figure 3.15. The closeness of these solutions is surprising. Tripling characteristic acceleration a_c from 1 to 3 mm/s^2 leads to only a 4% decrease in flight time. Therefore, we can confidently say that opting for characteristic accelerations larger than 1 mm/s^2 is not really helpful, since that implies a significant increment in the spacecraft thrust

system complexity, along with a decrease in payload, while only benefiting from a 4% flight duration reduction.

The opposite observation can also be made. For lower values of thrust, it is indeed convenient to try and adapt the spacecraft to increase this value. We can see that doubling the value from 0.1 to 0.2 mm/s^2 translates into a flight duration reduction of about 50%. Unlike the previous example, increasing thrust is now probably preferable.

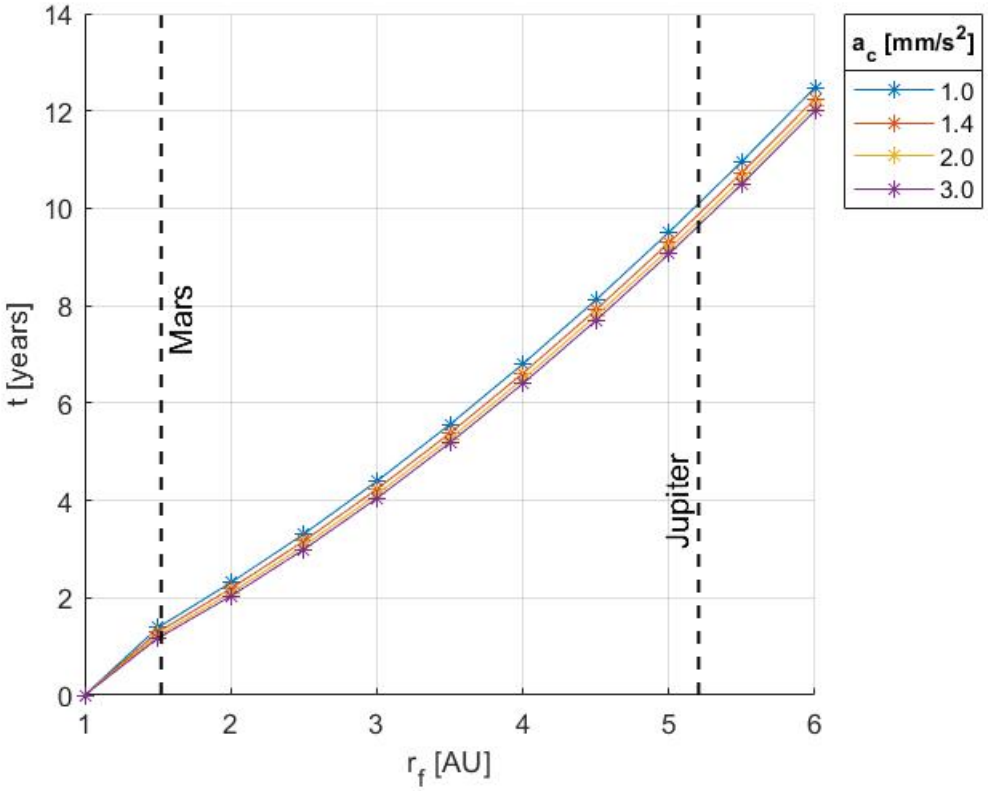

Figure 3.15 Zoomed version of the parametric study for higher values of characteristic acceleration.

In both figures, Jupiter and Mars radii are also displayed, making it possible to see how much time it would take the spacecraft to reach them for different values of characteristic accelerations.

4 Guidance strategies considering solar wind uncertainties

In this chapter, Sun variability is now introduced. Our goal is to come up with an strategy that allow us to reach the particular target desired, even with solar wind fluctuations happening. To do so, some concepts are presented first, such as margin control or saturation values. Then, we implement a series of guidance strategies, including Linear Quadratic Regulator (LQR) control and Model Predictive Control (MPC), with shrinking and receding horizons. Then, simulations are conducted and presented, allowing us to compare the methods.

4.1 The effect of solar wind perturbations and stiffness of the problem

Solar wind perturbations are the practical difficulty to deal with when working with Electric Solar Wind Sails. Its high variability makes it hard to be able to control the spacecraft in a specific way at any time. It limits maximum thrust and makes the presence of closed loop control almost mandatory. In this section we remark some considerations on how these fluctuations affect the Esail orbit.

4.1.1 Different characteristic times between mission and control parameters. Saturation problem

It has been seen in the previous chapter that flight times in missions to Mars and Jupiter are in the scale of years of duration. However, it has also been shown that the variation of the control parameters τ and α_n (and, ultimately, tether grid voltage V_0) are in the scale of minutes. The conclusion we can extract from here is that it can be assumed that variations of τ and α_n, in the scale of mission time, can effectively be considered instantaneous.

That allows us to simplify the behaviour of the Esail acceleration $\boldsymbol{a}$. Recalling (2.22), we can see that thrust per unit of length (and consequently characteristic acceleration) is directly proportional to the tether voltage V_0, and also directly proportional to the square root of the solar dynamic pressure $p_\oplus$. This equation, combined with the fact that voltage can effectively vary instantaneously, makes it possible for the characteristic acceleration a_c to remain constant, even with solar wind fluctuations. The idea is that, if $p_\oplus$ increases, we make V_0 decrease in such a way that a_c remains constant. The opposite also holds: if $p_\oplus$ diminishes, we can rise V_0 accordingly to maintain a_c stable.

But there is an exception, voltage saturation. As stated in Chapter 2.2.2, there exists a saturation value for V_0 approximately given by the value such that eV_0 surpasses the kinetic energy of the solar wind protons. Going for a higher voltage does not translate anymore in a higher characteristic acceleration. That means that, if solar wind pressure decays too much, we are not able to mitigate those effects, and our characteristic acceleration necessarily decreases. let us define $\tilde{a_c}$ as the value of characteristic acceleration at saturation voltage at 1 AU distance from the Sun. If we suppose solar wind nominal, then $\tilde{a_c} = a_c$, but things change when solar wind varies. As mentioned above, characteristic acceleration is directly proportional to the square

root of dynamic pressure. Then, given that we know voltage stays on its saturation value, we can express the real characteristic acceleration including solar wind uncertainty as

$$\tilde{a_c} = a_c \sqrt{\frac{p_\oplus}{\overline{p_\oplus}}} \tag{4.1}$$

We can see that, if dynamic pressure happens to be higher, $\tilde{a_c}$ increases. Intuitively we can imagine the solar wind having more energy, and thus the Esail extracts more from it. The opposite also occurs, if solar wind pressure decreases, $\tilde{a_c}$ diminishes accordingly.

It is important to notice that the notion of thrust lever τ does not make much sense anymore, since it was created as a way to simplify the output values to 0 and 1 instead of 0 and a_c, but a_c is not constant anymore, thus redefining τ each time and only seeing outputs of 0 and 1 does not give us information about real values of thrust and solar wind uncertainty. For this reason, we no longer use τ as a control parameter, but κ instead, defined as in equation 4.2, and denoted Esail acceleration parameter.

$$\kappa = \tau \tilde{a_c} = \tau a_c \sqrt{\frac{p_\oplus}{\overline{p_\oplus}}} \tag{4.2}$$

With this new definition of control parameters, the state equations are now.

$$\begin{aligned}
\dot{r} &= v_r \\
\dot{\theta} &= \frac{v_\theta}{r} \\
\dot{v_r} &= \frac{v_\theta^2}{r} - \frac{\mu}{r^2} + \frac{\kappa}{2}\left(\frac{r_\oplus}{r}\right)\left(1+\cos^2\alpha_n\right) \\
\dot{v_\theta} &= -\frac{v_r v_\theta}{r} + \frac{\kappa}{2}\left(\frac{r_\oplus}{r}\right)\cos\alpha_n \sin\alpha_n
\end{aligned} \tag{4.3}$$

The minimum value of κ is logically 0, while the maximum is $\kappa^{max} = a_c \sqrt{\frac{p_\oplus}{\overline{p_\oplus}}}$. Here, a_c and $\overline{p_\oplus}$ are constant, but $p_\oplus$ varies following the gamma distribution discussed in Chapter 2.3.2. Therefore, technically, we would have to update κ^{max} at every instant of time to account for solar wind variations. Note that, in the nominal case, the maximum value of κ is $\kappa_{nom}^{max} = a_{c_{nom}}$, and, in our case, $a_{c_{nom}} = 0.6\, a_c$.

4.1.2 Problem stiffness due to limited maneuvering capability

In this chapter, solar wind perturbations are introduced. As a consequence, it is inevitable that the spacecraft will often encounter itself in a different position from where it should be according to the nominal trajectory. The capability of our feedback strategy to deal with this error depends on the maneuvering capabilities of the Esail, on the closed loop algorithm used, on the size of the error and on the control margin left. In this section we center our attention on the first mentioned, maneuvering capability.

An increase in characteristic acceleration logically means more maneuvering capability and thus, more robustness against dynamic pressure variation. However, as it has been observed in section 3.3.4, going higher than 1 mm/s^2 does not translate into a noticeable difference in flight time reduction, which is a way to measure the spacecraft performance. One key problem is actually in thrust cone angle; even if we set sail pitch angle to give us maximum thrust cone angle, it results in less than 20°, as shown in Chapter 2.2.1. That means that our angular region of feasible thrust direction is only $\sim$ 11 % from the total (40° from 360°). To put that in perspective, let us say we want to travel to Jupiter, and assume we have as much thrust modulus as desired. Even with those assumptions, we would still need to limit our thrust, since it is not an option to arrive to Jupiter with a large excess of radial velocity, due to the fact that we can not aim thrust vector towards the Sun, and therefore we would miss our target.

Furthermore, there is the restriction of the arrival true anomaly angle. In Chapter 3, we assumed that launch date was free to choose, and that allowed us to disregard the condition of $\theta\left(t_f\right) = \theta_{planet}\left(t_f\right)$, since we could select the departure date to be the one that provided us the adequate phase angle between the planets. This is not a degree of freedom anymore in closed loop control. When we are already in orbit, and want to recalculate the optimal orbit to our target because we have been displaced from the original due to dynamic

pressure variations, we have already departed, and therefore initial time is no longer a free variable. To account for this new restriction, we have to add extra constraints to our problem. We may want to reach the planet at exactly the time proposed by the nominal orbit, and with the corresponding θ that was initially calculated. A problem of this type should be solved with the next constraints:

$$\begin{aligned} t_f &= t_f^{nom} \\ \theta_f &= \theta_f^{nom} \end{aligned} \tag{4.4}$$

We may, otherwise, not fix the final time, but we logically want the planet to be there when we reach its orbit. In that case, we would need to add the constraint shown in (4.5), where n_p stands for the angular velocity of the target planet.

$$\theta_f = \theta_f^{nom} + n_p \left(t_f - t_f^{nom} \right) \tag{4.5}$$

These limitations mean that, ideally, we would need to have a high control of our tangential speed (and thus, angular position) to adapt for possible changes and accomplish our mission. However, reality is quite different. We can recall from Chapter 2.2.1 that maximum tangential acceleration is obtained with $\alpha_n = 45^\circ$, and, for our characteristic acceleration $a_c = 0.36$ mm/s^2 = 0.0607 UA, our maximum value is $a_\theta^{max} = 0.0152 \left(\frac{r_\oplus}{r} \right)$ UA, for a generic distance r. At the same time, we can compute the velocity of a circular orbit at a distance r from the Sun as $v_\theta = \left(\frac{r_\oplus}{r} \right)^{1/2}$ UV. Since we are planning missions to Jupiter at ~ 5.2 AU and Mars at ~ 1.5 AU, we establish for these calculations a mean generic value of $r = 1.5$ AU. For that distance to the Sun, we have a velocity of $v_\theta = 0.816$ UV, while the maximum tangential acceleration that the Esail can produce is $a_\theta^{max} \approx 0.0101$ UA. If we wanted, for example, to reduce tangential velocity of our spacecraft a 5%, that would mean that, at maximum tangential thrust (we assume for simplicity that the spacecraft stays in a circular orbit, even if it is not true, it is sufficient to prove maneuvering limitations), it would take the spacecraft 8.1 UT (1.3 years) to do so, while it would only take a radius increment of 11% to do the same thing if we opted for increasing the circular orbit radius.

These are simplified calculations and are only meant for intuition purposes. The conclusion we can extract from here is that, if the spacecraft happens to be closer to the Sun than it should be compared to the nominal orbit at some instant of time (and it can happen if a period with really low dynamic pressure occurs), it is very difficult for the Esail to counteract this increment in tangential velocity, which effectively creates a mismatch in angle θ, and it can often lead to a mission failure, skipping our desired target (Mars or Jupiter), given that conditions (4.4) or (4.5) can not be satisfied.

So, in conclusion, the spacecraft has an extremely limited maneuvering capability. In successful missions presented later, it can be see that, if a period with reduced radius compared to the nominal orbit happens, then another in which the radius is larger occurs later, so that both effects counteract each other, making it possible to reach the desired target successfully. If that period of lesser radius than desired occurs too late, or too abruptly, there may not be any way to fix it.

The extremely relevant presence of the Sun is obviously of importance in spacecrafts with others types of propulsion too. The difference is that those thrust systems are accurately characterized, and therefore their uncertainties are considerably lower, making it substantially more improbable for the spacecraft to deviate that much from the nominal orbit.

4.1.3 Setting a control margin

Setting a control margin to account for uncertainties is a typical practice in closed loop control problems. The idea is that, assuming that control parameters have a saturation value, we first calculate a nominal solution ignoring perturbations and further limiting our control parameters, only to then tackle the real solution with an extra margin of control that can take care of undesired behaviour due to the presence of perturbations.

This is not the first time that this idea is mentioned. In Chapter 3 we mentioned that, even if our maximum value of characteristic acceleration is $a_c = 0.6$ mm/s^2, we use the 60% of it for the calculation of the nominal orbit. This number is not chosen at random, it has a reason. The idea is that, if we use limited acceleration for our nominal orbit, then in the real problem it is less probable that the solar wind dynamic pressure becomes

so low that not even maximum voltage can make up for its effect to maintain the desired thrust. The higher a control margin we leave, the more improbable a saturation problem becomes. Of course this increment in control margin is at the expense of higher flight times, since the spacecraft's maximum characteristic acceleration is constant, and leaving more control margin means decreasing the value of a_c used for the nominal orbit. Consequently, we need to find a trade-off between these two issues. Low control margins mean faster missions but with a higher failure rate, and high control margins mean exactly the opposite.

A reasonable strategy to deal with these solar wind perturbations is as follows.

- If, for a given dynamic pressure $p_\oplus$, saturation voltage is able to compensate its effect, and therefore $\kappa^{max} > \kappa^{max}_{nom}$, we set V_0 to make $\kappa = \kappa_{nom}$ and follow the nominal trajectory.
- If $p_\oplus$ becomes so low that, even with saturation voltage, $\kappa^{max} < \kappa^{max}_{nom}$, then we set $\kappa = \kappa^{max}$ during that time interval, and then recalculate a new optimal orbit, since we are now displaced from the original one. This arc at maximum available thrust is often called deviation arc.

This strategy is suggested in [38]. For the nominal orbit, a maximum tether voltage of 25 kV is utilized, while for the real orbit that voltage is increased to 80 kV (value at which voltage saturation becomes prevalent). That means that they are setting a control margin of 69%. As suggested before, there is not visible evidence of benefit from setting control margin in the sail pitch angle, since the spacecraft never approaches its limit value. That assumption matches with what is seen in this report, since it does not set a sail pitch angle margin neither.

The problem with this strategy is that there is no guarantee that a feasible new orbit, after a deviation arc, can be computed. One could argue that, if the problem is subject to (4.5), there has to exist a solution undoubtedly, since final time is not fixed. Theoretically, having infinite time, there must exist not one but multiple solutions in which the spacecraft is able to reach its target, and we would obviously prefer the fastest one. However, even if those solutions exist, they have proven to be extremely difficult to find, at least with the direct transcription method utilized in this project. Therefore, for feasibility reasons, we first study solutions with fixed time, i.e. following restrictions in (4.4), although Model Predictive Control (MPC) related strategies are later presented for unfixed final time, but they are no longer time-optimal solutions.

Since there are no guarantees that a new solution can be computed after being considerably displaced from the nominal orbit due to a really low dynamic pressure interval, we must avoid these intervals as much as possible, and that is made possible by setting some control margin. Knowing the probabilistic distribution of $p_\oplus$, a study can be conducted to determine the probability of κ^{max} being lower than κ^{max}_{nom} in terms of the control margin left. The results of that study can be seen in figure 4.1. If we do not set a control margin in the nominal orbit calculation, and extract a random value of dynamic pressure from the gamma distribution, the probability of κ^{max} being smaller than κ^{max}_{nom} is $\sim$ 60 %, interestingly, it is greater than 50%, due to the positive skewness of the distribution. If we set a control margin of 20%, that probability is reduced to $\sim$ 40 %, and setting a margin of 40%, the probability drops to 20%. Up to this point, the graph follows a linear trend in which a 10% increase in control margin diminishes a 10% the probability of $\kappa^{max} < \kappa^{max}_{nom}$. If we keep increasing the control margin, that linear trend is broken, and a 10% increase in control margin does not imply anymore a 10% decrease in probability, but less instead. Because of that, a good compromise value for control margin is 40%, the one represented in the figure, giving us a 20% probability of saturating each time a new value of dynamic pressure is obtained. Thus, this value is used for the next calculations.

4.2 LQR control

4.2.1 Introduction to the Linear Quadratic Regulator

LQR stands for Linear Quadratic Regulator. It is an strategy used to tackle an optimal control problem in which state variables are governed by linear differential equations, and the cost function is defined in a quadratic form [42]. However, our state differential equations are highly nonlinear, so the way to proceed is to use Taylor first order approximations, and evaluate them in the corresponding instances as the problem advances. Our goal is to follow the nominal orbit, so, once the state functions are linearized, we evaluate them for the corresponding values of $\boldsymbol{x}$ and $\boldsymbol{u}$ from the nominal orbit at each instance of time. We refer to

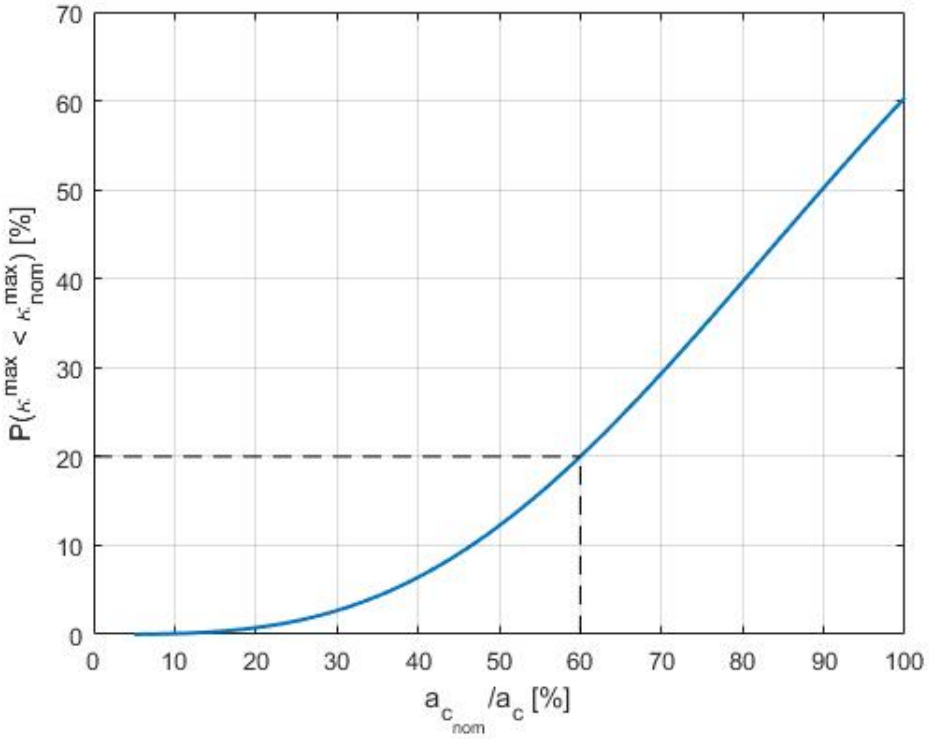

Figure 4.1 Probability of entering in a deviation arc as a function of control margin.

these values of the nominal orbit as reference values, and denote them as $\boldsymbol{x}^\star$ and $\boldsymbol{u}^\star$. Therefore, since we want to minimize our error with respect to the reference strategy at every instant of time, it is easy to see that with this formulation, final time is fixed, coinciding with the obtained in the nominal orbit calculation.

There are two types of LQR problems, with infinite and finite horizon. The first one is used when there is no particular limitation in time, hence its name. The system has to go from one state to another constant state of reference, and the time it takes and resources it spends depend on some parameters later introduced. On the other side, finite horizon is used when we want to impose some final boundary conditions at a determined time. It is often used when matrix $\boldsymbol{A}$ and $\boldsymbol{B}$ are time-dependent. When we talk about LQR control to tackle our closed loop control problem, we refer to the latter, which is often used in spacecraft control systems, for both trajectory following and attitude control [43]. It can be also implemented in other aerospace applications, such as trajectory following for space launch vehicles subject to perturbations [44].

Our first aim is to transform our state equations from $\dot{\boldsymbol{x}} = \boldsymbol{f}(\boldsymbol{x}, \boldsymbol{u}, t)$ to a linear approximation. Given that we start from a reference point in the nominal trajectory, we can compute how small changes in state variables and control parameters as $\delta\dot{\boldsymbol{x}} = \boldsymbol{A}\,\delta\boldsymbol{x} + \boldsymbol{B}\,\delta\boldsymbol{u}$, where $\boldsymbol{A}$ and $\boldsymbol{B}$ are matrices determined by Taylor first approximations. Note that $\boldsymbol{A}$ and $\boldsymbol{B}$ can be time-dependent, in fact, they are in our problem. Even if time does not appear explicitly, the variables $\boldsymbol{x}(t)$ and $\boldsymbol{u}(t)$ are time-dependent. These matrices can be computed as

$$\boldsymbol{A}(t) = \begin{bmatrix} \frac{\partial \dot{r}}{\partial r} & \frac{\partial \dot{r}}{\partial \theta} & \frac{\partial \dot{r}}{\partial v_r} & \frac{\partial \dot{r}}{\partial v_\theta} \\ \frac{\partial \dot{\theta}}{\partial r} & \frac{\partial \dot{\theta}}{\partial \theta} & \frac{\partial \dot{\theta}}{\partial v_r} & \frac{\partial \dot{\theta}}{\partial v_\theta} \\ \frac{\partial \dot{v}_r}{\partial r} & \frac{\partial \dot{v}_r}{\partial \theta} & \frac{\partial \dot{v}_r}{\partial v_r} & \frac{\partial \dot{v}_r}{\partial v_\theta} \\ \frac{\partial \dot{v}_\theta}{\partial r} & \frac{\partial \dot{v}_\theta}{\partial \theta} & \frac{\partial \dot{v}_\theta}{\partial v_r} & \frac{\partial \dot{v}_\theta}{\partial v_\theta} \end{bmatrix}_\star, \qquad \boldsymbol{B}(t) = \begin{bmatrix} \frac{\partial \dot{r}}{\partial \kappa} & \frac{\partial \dot{r}}{\partial \alpha_n} \\ \frac{\partial \dot{\theta}}{\partial \kappa} & \frac{\partial \dot{\theta}}{\partial \alpha_n} \\ \frac{\partial \dot{v}_r}{\partial \kappa} & \frac{\partial \dot{v}_r}{\partial \alpha_n} \\ \frac{\partial \dot{v}_\theta}{\partial \kappa} & \frac{\partial \dot{v}_\theta}{\partial \alpha_n} \end{bmatrix}_\star \tag{4.6}$$

Note that, as previously stated, we are now utilizing κ instead of τ as the thrust control parameter. Thus, the functions we are going to linearize are the ones in (4.3), resulting in matrices $\boldsymbol{A}$ and $\boldsymbol{B}$ shown next

$$\boldsymbol{A}(t) = \begin{bmatrix} 0 & 0 & 1 & 0 \\ -\frac{v_\theta^\star}{r^{\star 2}} & 0 & 0 & \frac{1}{r^\star} \\ -\frac{v_\theta^{\star 2}}{r^{\star 2}} + \frac{2\mu}{r^{\star 3}} - \frac{\kappa^\star}{2r^\star}\left(\frac{r_\oplus}{r^\star}\right)\left(1+\cos^2\alpha_n^\star\right) & 0 & 0 & \frac{2v_\theta^\star}{r^\star} \\ \frac{v_r^\star v_\theta^\star}{r^{\star 2}} - \frac{\kappa^\star}{2r^\star}\left(\frac{r_\oplus}{r^\star}\right)\cos\alpha_n^\star \sin\alpha_n^\star & 0 & -\frac{v_\theta^\star}{r^\star} & -\frac{v_r^\star}{r^\star} \end{bmatrix} \tag{4.7}$$

$$\boldsymbol{B}(t) = \begin{bmatrix} 0 & 0 \\ 0 & 0 \\ \frac{1}{4}\left(\frac{r_\oplus}{r^\star}\right)\left[3+\cos 2\alpha_n^\star\right] & -\frac{\kappa^\star}{2}\left(\frac{r_\oplus}{r^\star}\right)\sin 2\alpha_n^\star \\ \frac{1}{4}\left(\frac{r_\oplus}{r^\star}\right)\sin 2\alpha_n^\star & \frac{\kappa^\star}{2}\left(\frac{r_\oplus}{r^\star}\right)\cos 2\alpha_n^\star \end{bmatrix} \tag{4.8}$$

We also have to define a cost function that we want to optimize. In this case, the adequate quantity to minimize is the error between our current path and the nominal previously calculated, since our goal is to follow it. Therefore, we define the variables $\delta\boldsymbol{x} = \boldsymbol{x} - \boldsymbol{x}^\star$ and $\delta\boldsymbol{u} = \boldsymbol{u} - \boldsymbol{u}^\star$, which are the state variables and control parameters errors with respect to the nominal trajectory.

The result for this optimization problem is well known, as LQR is a basic optimal control solution widely used in many applications. Given that our cost function is defined as in (4.9), it can be proven that the control law that minimizes J is in the form of $\delta\boldsymbol{u} = \boldsymbol{K}(t)\,\delta\boldsymbol{x}$.

$$J = \int_0^{t_f} \left[\delta\boldsymbol{x}^\intercal(t)\,\boldsymbol{Q}(t)\,\delta\boldsymbol{x}(t) + \delta\boldsymbol{u}^\intercal(t)\,\boldsymbol{R}(t)\,\delta\boldsymbol{u}(t)\right]\mathrm{d}t + \delta\boldsymbol{x}^\intercal\left(t_f\right)\boldsymbol{Q}_{end}\delta\boldsymbol{x}\left(t_f\right) \tag{4.9}$$

Where $\boldsymbol{Q}(t)$, $\boldsymbol{R}(t)$ and $\boldsymbol{Q}_{end}$ are weighting matrices. $\boldsymbol{Q}(t)$ and $\boldsymbol{Q}_{end}$ must be definite positive matrices, while $\boldsymbol{R}(t)$ must be semidefinite positive. There is an additional condition known as controllability of the system [45], that is not strictly necessary for finite horizon LQR, but avoids many problems. For our model, that condition is met. For simplicity, and as a common procedure in these types of problems, even if J in equation 4.9 is designed for time-depending matrices $\boldsymbol{Q}$ and $\boldsymbol{R}$, we assume they are constant. Moreover, we set $\boldsymbol{Q}$, $\boldsymbol{R}$ and $\boldsymbol{Q}_{end}$ to be diagonal. For our case of four state variables and two control parameters, these matrices have the following structure

$$\boldsymbol{Q} = \begin{bmatrix} Q_r & 0 & 0 & 0 \\ 0 & Q_\theta & 0 & 0 \\ 0 & 0 & Q_{v_r} & 0 \\ 0 & 0 & 0 & Q_{v_\theta} \end{bmatrix}, \qquad \boldsymbol{R} = \begin{bmatrix} R_\kappa & 0 \\ 0 & R_{\alpha_n} \end{bmatrix}, \qquad \boldsymbol{Q}_{end} = \begin{bmatrix} Q_{end_r} & 0 & 0 & 0 \\ 0 & Q_{end_\theta} & 0 & 0 \\ 0 & 0 & Q_{end_{v_r}} & 0 \\ 0 & 0 & 0 & Q_{end_{v_\theta}} \end{bmatrix} \tag{4.10}$$

The matrix $\boldsymbol{K}(t)$ mentioned above can be computed from

$$\boldsymbol{K}(t) = -\boldsymbol{R}^{-1}\boldsymbol{B}^\intercal(t)\,\boldsymbol{P}(t) \tag{4.11}$$

Where $\boldsymbol{P}(t)$ is obtained from solving the usually called *Riccati differential equation*, defined as

$$-\dot{\boldsymbol{P}} = \boldsymbol{A}^{\top}\boldsymbol{P} + \boldsymbol{P}\boldsymbol{A} - \boldsymbol{P}\boldsymbol{B}\boldsymbol{R}^{-1}\boldsymbol{B}^{\top}\boldsymbol{P} + \boldsymbol{Q}, \qquad \boldsymbol{P}\left(t_f\right) = \boldsymbol{Q}_{end} \tag{4.12}$$

Note that, since $\boldsymbol{A}$ and $\boldsymbol{B}$ are evaluated at the nominal orbit, their value is known at every instance of time, and that $\boldsymbol{Q}$, $\boldsymbol{R}$ and $\boldsymbol{Q}_{end}$ are previously defined and thus, known. Moreover, t_f is also known, since it coincides with the one obtained for the nominal orbit. That implies that, even if $\boldsymbol{P}$ depends on time, we can calculate its value at the start of the route (all the necessary information is known) and store it, not being influenced by solar wind variability or other kinds of perturbations. A differential equation with a final condition can be solved with a change of variable such as $\tilde{t} = t_f - t$, for which it becomes a first order differential equation with an initial condition ($\boldsymbol{P}(\tilde{t} = 0) = \boldsymbol{Q}_{end}$), instead of one given at the final instant. After solving the equation, we can reverse this change of variable to find the solution.

A simple block diagram of the LQR closed loop control strategy is presented in figure 4.2, where $\boldsymbol{u}'$ refers to the control parameter's value prior to implementing saturation. As expected, there is a saturation block to limit values of thrust lever greater than κ^{max} and sail pitch angles greater than 70° (we saw in previous chapters that there is no point on going higher than $\approx 55^{\circ}$, but LQR does not "know" that, it is working with a linearized system and an excess can occur). This saturation block depends on the value of the dynamic pressure, which changes with time.

The way to approach the problem of uncertainty in $p_{\oplus}$ is by establishing a fixed time interval in which the value of $p_{\oplus}$ is assumed to be constant, and update it each time the interval ends and another starts. The decision of how long these intervals should be is not trivial. On one hand, larger intervals are preferable for reducing the computational cost of the program. However, it is also less realistic, and it can even produce undesired instabilities. Remembering that we calculated the nominal orbit with the mean of the dynamic pressure distribution, and also set control margin, the closed loop control problem with perturbations should be solvable as long as $p_{\oplus}$ does not deviate significantly from its nominal value. The problem is that, with larger (and therefore fewer) time intervals, a longer period with low dynamic pressure can happen, to the point where the problem becomes irrevocably infeasible. With shorter time intervals, it becomes less probable that the spacecraft stays in a low dynamic pressure situation for that long, thus increasing the probabilities of success.

On the other hand, short time intervals raise the computational cost (and time) significantly, and they can even disagree with physical behaviour of the Sun. Ultimately, every physical transformation is continuous, and therefore, Sun fluctuations can not occur in an arbitrarily short period of time. However, even if that is true, observations indicate that these fluctuations can happen in hours which, compared to the years a mission takes to complete, is an extremely short period of time.

One good compromise value for Jupiter is to carry out 50 dynamic pressure recalculations during the mission. Given that flight duration is around 16 years, that is the equivalent to saying that dynamic pressure is updated each four months approximately. It is a middle value that provides good accuracy while maintaining reasonable computational times. We also have to remember that our whole problem is divided into 500 segments, so doing 50 recalculations leaves each interval with 10 discretization points. If we wanted to have shorter $p_{\oplus}$ recalculations time intervals, we would aso have to increase the intervals in which the problem is discretized, further increasing computational cost. For Mars, we have a mission flight time of approximately 3 years, and we establish 20 dynamic pressure recalculation intervals, consequently, each interval takes about two months to complete. For Mars, there are $500/20 = 25$ discretization points in each constant $p_{\oplus}$ interval. To implement this closed loop control strategy we use *Simulink*, which integrates the system with a variable step size to fulfill some tolerance requirements. Therefore, it does not make much sense to talk about discretization points in constant $p_{\oplus}$ intervals, although it becomes more relevant in the strategies presented in the next sections.

The principal problem with using LQR control as our strategy is the use of a linear approximation of state equations for the feedback loop, which is only accurate for rather small deviations from the nominal path. This is usually not a problem since, given that step size is small enough, the system can not really go far from the nominal state, since in each iteration the LQR corrects this deviation and points the system into the correct direction. But there is a limitation that we have not taken into account, and that is saturation. There

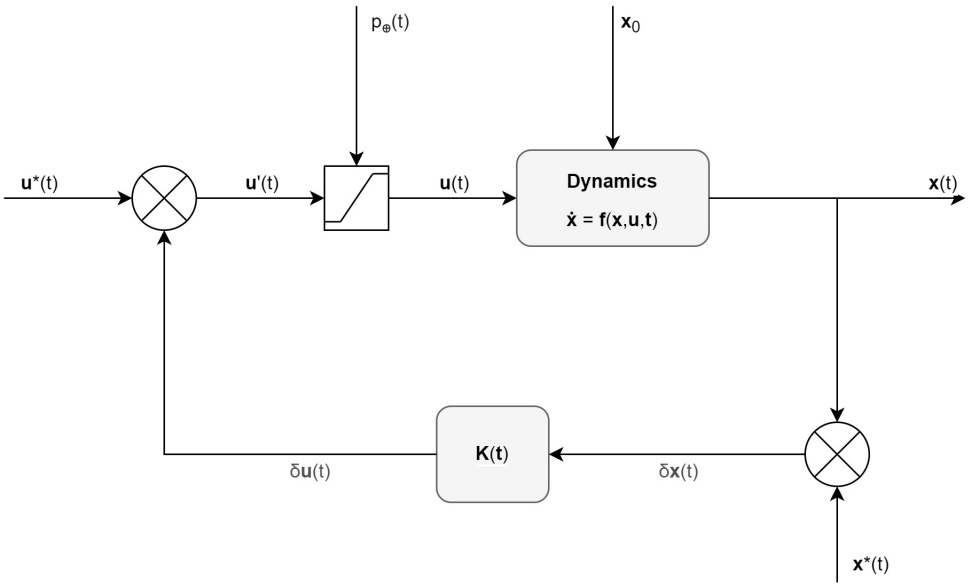

Figure 4.2 Block diagram for the LQR closed loop control strategy.

may be an instant in which, due to low dynamic pressure, or to a considerable error in position, the LQR estimates a correction value of κ higher than saturation. Because of that, after that iteration, the spacecraft may not be any nearer from the nominal trajectory, or it could even be farther. This situation can aggravate since, in addition to that, linear approximations are worse the farther we are from the nominal state. All this can end up in a total mission failure, with an orbit completely different from the nominal.

4.2.2 First strategy. Identity weighting matrices

The task now is to assign the best possible values to the components of the weighting matrices $\boldsymbol{Q}$, $\boldsymbol{R}$ and $\boldsymbol{Q}_{end}$ to reduce the probability of mission failure. Since we are working with uncertain variables, such as $p_{\oplus}$, the only way to extract conclusions is to do multiple simulations and statistically analyse the results. This strategy is known as the Monte Carlo method. We are working with the astronomical units system, which implies that all our variables are in the order of units (except θ, that rises to the order of tens for Jupiter, and κ, that stands around 0.05 UA). Because of this, starting with unit diagonal matrices such as shown in equation 4.13 appears to be a reasonable option.

$$\boldsymbol{Q} = \begin{bmatrix} 1 & 0 & 0 & 0 \\ 0 & 1 & 0 & 0 \\ 0 & 0 & 1 & 0 \\ 0 & 0 & 0 & 1 \end{bmatrix}, \qquad \boldsymbol{R} = \begin{bmatrix} 1 & 0 \\ 0 & 1 \end{bmatrix}, \qquad \boldsymbol{Q}_{end} = \begin{bmatrix} 1 & 0 & 0 & 0 \\ 0 & 1 & 0 & 0 \\ 0 & 0 & 1 & 0 \\ 0 & 0 & 0 & 1 \end{bmatrix} \tag{4.13}$$

We now define some parameters used to compare the effectiveness of different strategies. The first obvious fact to analyse is success rate, where success is achieved when the spacecraft reaches the planet with a distance smaller than its sphere of influence's radius. We can also keep a record of the missions that have been a total failure, defining total failure as ending up farther than 10 times the sphere of influence radius in the case of Jupiter, and farther than 50 times the sphere of influence radius for Mars (we adapt the definition of total failure for each planet because Jupiter's sphere of influence is almost 100 times bigger than Mars's). We also compute the mean distance $\overline{d}$ of all the 100 simulations and its standard deviation σ_d, conducting these studies for both Jupiter and Mars. The results for unit diagonal weighting matrices are shown in table 4.1, expressing success rate and total failure rate as percentages.

Table 4.1 Performance of Finite Horizon LQR for Jupiter and Mars with unit diagonal weighting matrices. The value $\overline{d}$ denotes the arrival distance to the planet and σ_d its standard deviation.

Planet	Success [%]	Total failure [%]	$\overline{d}$ [AU]	σ_d [AU]	r_{SOI} [AU]
♃	50	21	1.9014	3.1830	0.3222
♂	13	2	0.0536	0.0662	0.0039

Analysing the results in table 4.1, we see a surprisingly low success rate in both missions to Jupiter and Mars of 50% and 13% respectively. It is interesting to note that mission failure has occurred way more frequently in missions to Jupiter. That result agrees with the fact that a mission to Jupiter is more numerically challenging because of its considerably longer duration. The reason why it has had more total failures is because its increased flight time makes a control failure of LQR due to saturation more probable. However, Jupiter has also had way more accomplished missions than Mars,and that is because its larger sphere of influence's radius. Histograms of arriving distances, where the width of each bar is equal to the sphere of influence radius, can be observed in figure 4.3, for both simulations to Jupiter and Mars. We can observe that, even if Mars has had few successful missions, there are plenty of them that have ended up very near, in contrast with what can be seen in Jupiter.

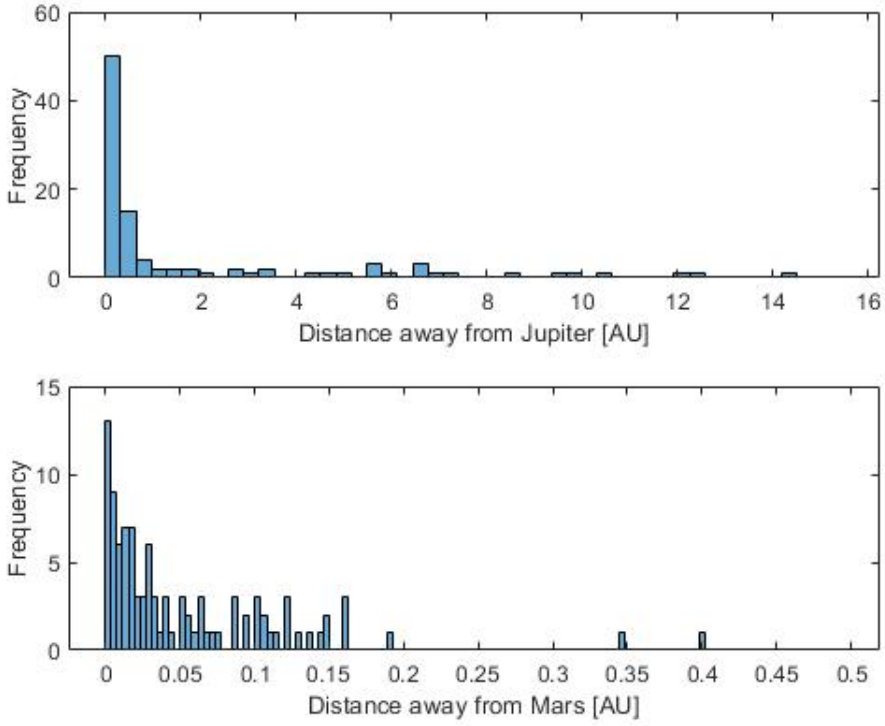

Figure 4.3 Histograms of arrival distance values for simulations to Jupiter (top) and Mars (bottom) with Finite Horizon LQR with unit diagonal weighting matrices.

In figure 4.4, trajectory and evolution of variables is shown for a successful mission, and in figure 4.5 for a total failure. The corresponding images for Mars missions can be found in Appendix B. It is interesting to notice in figures 4.4 and 4.5 the variability of κ. When thrust saturation value decays below the nominal, the LQR controller has to react to bring the spacecraft back to the nominal orbit. If it is able to do so, then the mission ends up being successful, otherwise it can vary from a decent result to a total failure. Knowing this, and observing that thrust lever is the most changing value, it is next presented a new reasonable weighting configuration. It is also interesting to note that the spacecraft follows the nominal sail pitch angle value almost perfectly, which indicates that α_n is not the problem that leads to failed missions, but rather only κ is.

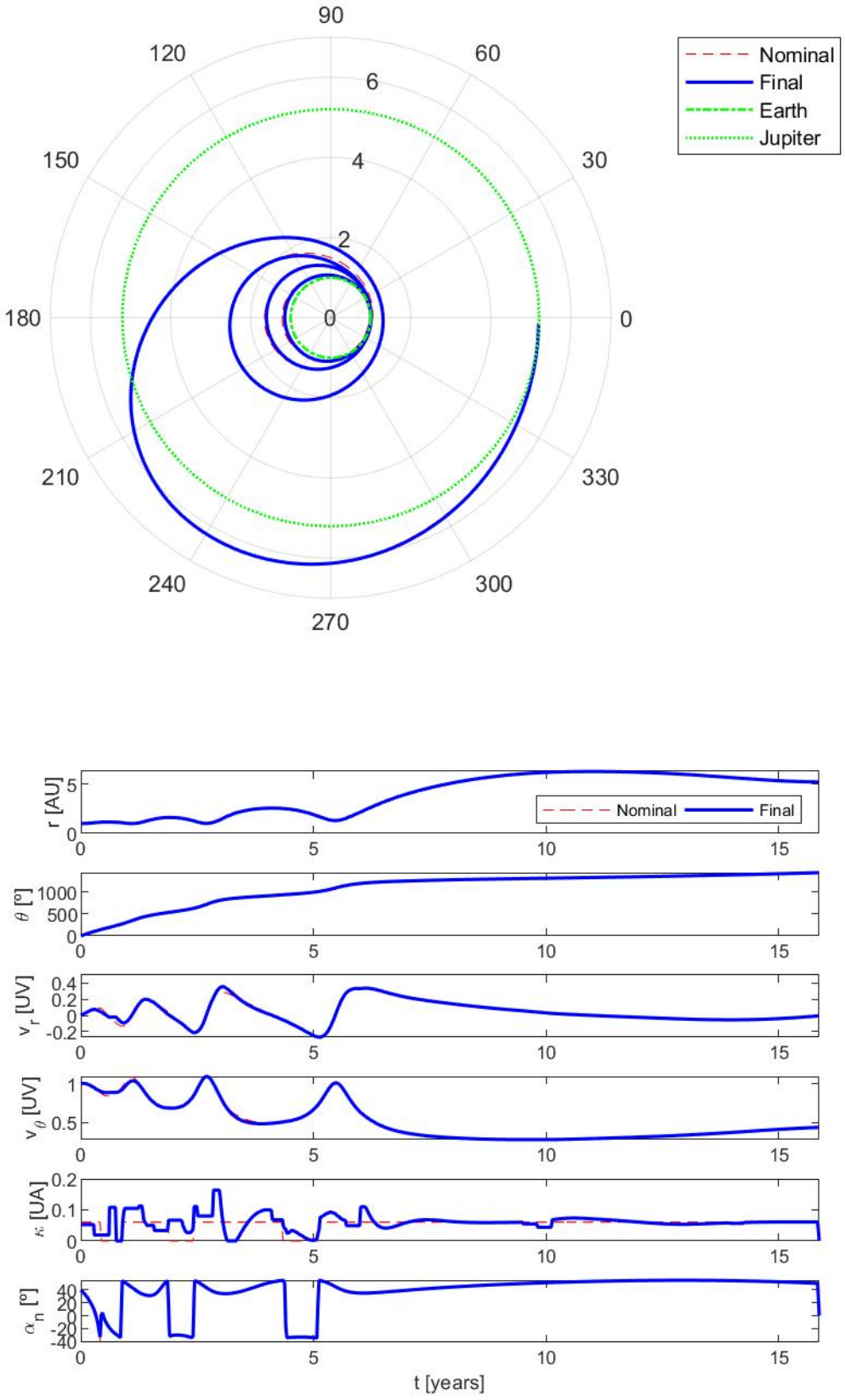

Figure 4.4 Trajectory and evolution of state and control variables in a successful mission to Jupiter using Finite Horizon LQR with unit diagonal weighting matrices.

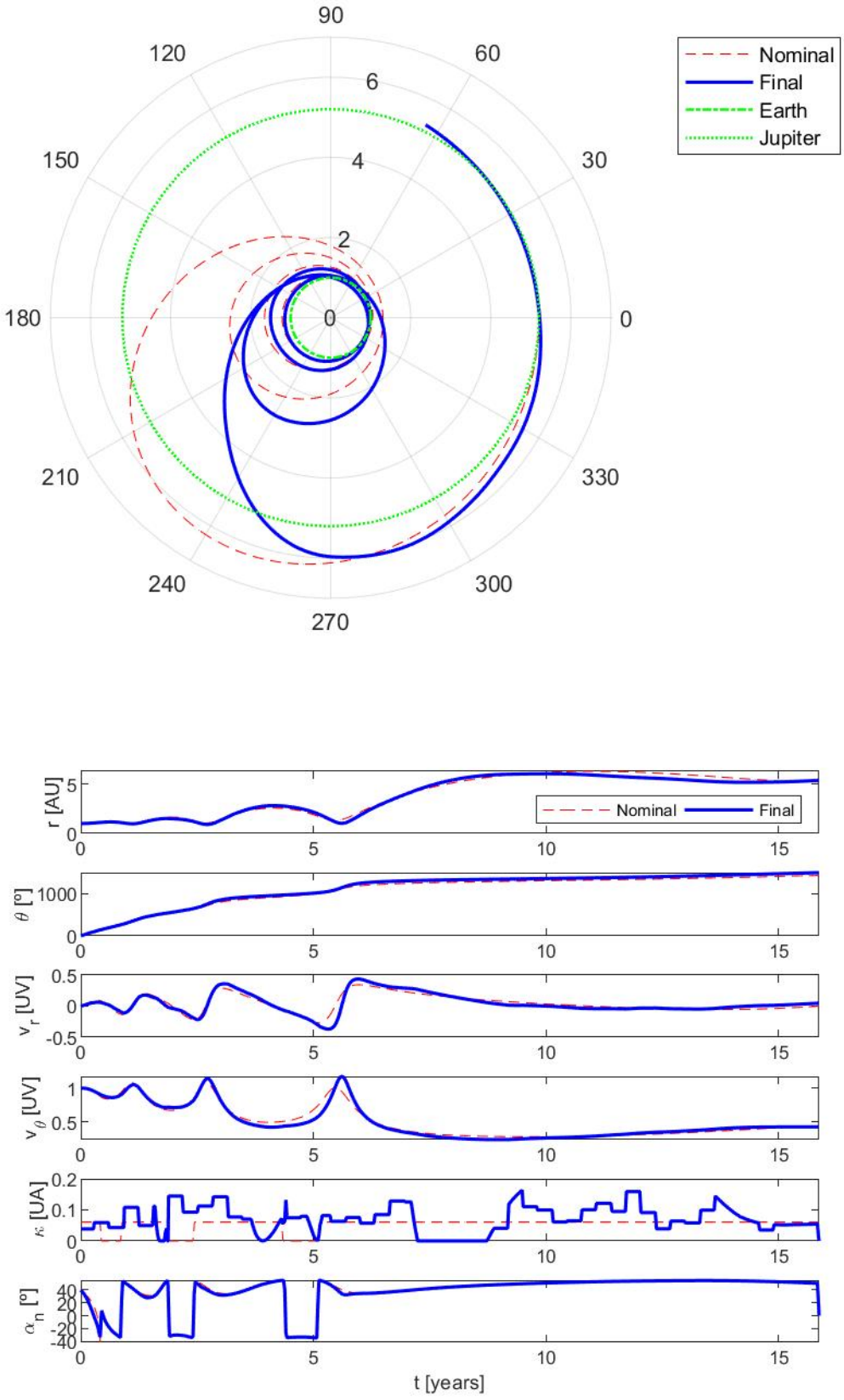

Figure 4.5 Trajectory and evolution of state and control variables in an unsuccessful mission to Jupiter using Finite Horizon LQR with unit diagonal weighting matrices.

4.2.3 Second strategy. Prioritizing thrust lever error

We have previously mentioned that κ value is around 0.05 UA. That may imply that, given our cost function expression in (4.9), LQR control may opt to optimize other variables rather than thrust lever. That is because, if the mean value of thrust lever is smaller, for example, than the mean value of the distance to the Sun r, then it is very likely that $\delta\kappa < \delta r$ (actually, these values do not have the same physical dimensions, but weighting matrices take care of that), since they measure absolute errors, not relative. Therefore, for equal weights, it is better to optimize δr, since $\delta r Q_r \delta r > \delta\kappa R_\kappa \delta\kappa$, because a decrease in δr reduces the cost function more than a decrease of the same percentage in $\delta\kappa$. However, we do not always want to do that. Thrust lever is a crucial parameter in our problem, and by assuring that nominal path is followed with a small deviation of κ from its nominal value, we theoretically reduce the possibility of a mission failure happening. We can give it a weight of $R_\kappa = 20$. That way, thrust lever weighted error is the same size as errors from other variables. Therefore, we now conduct a new study with a modified $\boldsymbol{R}$ weight matrix, as follows

$$\boldsymbol{Q} = \begin{bmatrix} 1 & 0 & 0 & 0 \\ 0 & 1 & 0 & 0 \\ 0 & 0 & 1 & 0 \\ 0 & 0 & 0 & 1 \end{bmatrix}, \qquad \boldsymbol{R} = \begin{bmatrix} 20 & 0 \\ 0 & 1 \end{bmatrix}, \qquad \boldsymbol{Q}_{end} = \begin{bmatrix} 1 & 0 & 0 & 0 \\ 0 & 1 & 0 & 0 \\ 0 & 0 & 1 & 0 \\ 0 & 0 & 0 & 1 \end{bmatrix} \tag{4.14}$$

Performance parameters of LQR strategy with these new weighting functions are shown in table 4.2 and histograms of the arrival distance away from the planet of all the simulations conducted can be seen in figure 4.6.

Table 4.2 Performance of Finite Horizon LQR for Jupiter and Mars prioritizing thrust lever error in weighting matrices. The value $\overline{d}$ denotes the arrival distance to the planet and σ_d its standard deviation.

Planet	Success [%]	Total failure [%]	$\overline{d}$ [AU]	σ_d [AU]	r_{SOI} [AU]
♃	25	11	1.4921	2.1658	0.3222
♂	2	19	0.1183	0.1084	0.0039

These results are undoubtedly worse than the ones obtained with the initial weighting scheme. It has diminished both Jupiter and Mars successes, although it has improved the spacecraft's behaviour in missions to Jupiter that suffer from a specially high solar wind variability, which is reflected in the reduction in the percentage of total failures and the mean distance $\overline{d}$. However, that is not the case for Mars missions, in which the spacecraft finds it now more difficult to approach Mars, and ends up further from it on average. The increase in the mean distance and its standard deviation is noticeable. This is a good example of how counter-intuitive LQR can be; even if we raised R_κ to reduce the probability of κ drifting too much from the nominal value, it did the exact opposite. That is because, if we increase the importance of $\boldsymbol{u}$ in the cost function, we may are ignoring errors in $\boldsymbol{x}$ that can also be crucial to not incur in saturation.

Ideally, we would do a sweep between multiple configurations for the weighting matrices, doing many simulations more for each. With that approach, better results would be encountered, and we would probably find that the optimal LQR tuning is not the same depending on whether we consider Jupiter or Mars missions. However, this is extremely computationally expensive, and an extensive period of time would be needed. This is why we opt for the same tuning for both missions, and test a limited amount of configurations. The conclusion we can extract from this weighting change is that it is not worth it, since it diminishes both Mars and Jupiter successful missions. Thus, we maintain the initial control parameter weighting configuration.

4.2.4 Third strategy. Prioritizing arrival position error

As it can be seen from the data gathered in both simulations, there are many cases in which the mission is not a success nor a total failure. In fact, there are many solutions that end up being very near from the sphere of influence, although outside from it. That suggests that it could be a good idea to increase the weights from $\boldsymbol{Q}_{end}$ matrix, since that represents the error in the final conditions. By doing that, we force the LQR controller to prioritize the minimization of these arrival conditions. However, these weights can not be indefinitely large, since it is also important to not deviate much from the initial orbit during the mission, because we have

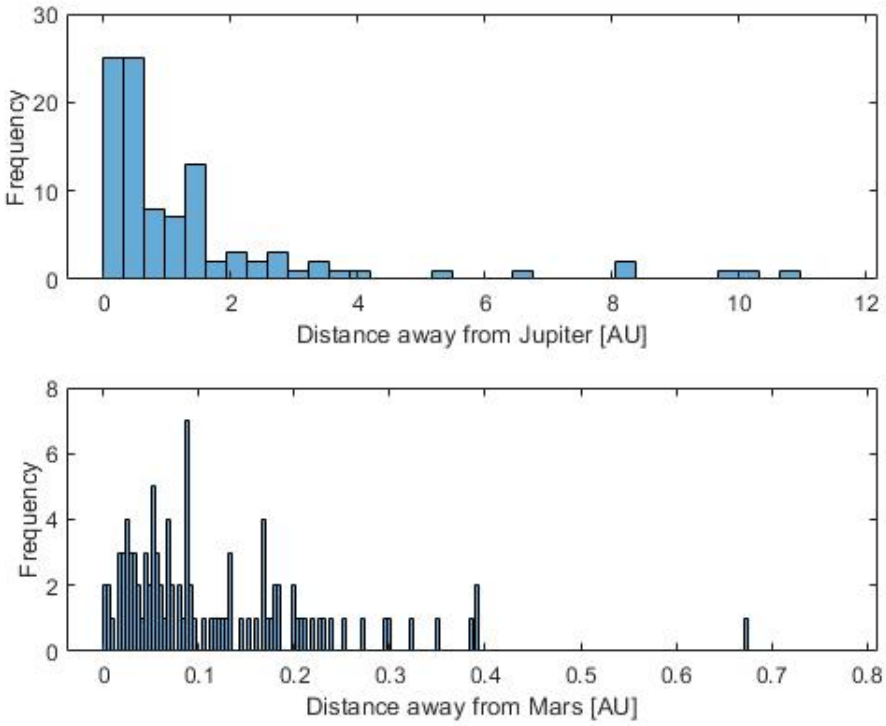

Figure 4.6 Histograms of arrival distance values for simulations to Jupiter (top) and Mars (bottom) with Finite Horizon LQR prioritizing thrust lever error in weighting matrices.

to avoid the saturation problems explained above. We may define now our weighting matrices as is shown in (4.15), where we have augmented the weighting value of the arrival radius and true anomaly. Velocities are left untouched because, even if that makes them differ a noticeable amount, high thrust complementary systems can take care of that. Furthermore, the range of velocity values with which we can reach the planet in the given amount of time, while tracking the reference orbit, is not especially large. These new results are shown in table 4.3, and the corresponding histograms can be seen in figure 4.7.

$$\boldsymbol{Q} = \begin{bmatrix} 1 & 0 & 0 & 0 \\ 0 & 1 & 0 & 0 \\ 0 & 0 & 1 & 0 \\ 0 & 0 & 0 & 1 \end{bmatrix}, \qquad \boldsymbol{R} = \begin{bmatrix} 1 & 0 \\ 0 & 1 \end{bmatrix}, \qquad \boldsymbol{Q}_{end} = \begin{bmatrix} 10 & 0 & 0 & 0 \\ 0 & 10 & 0 & 0 \\ 0 & 0 & 1 & 0 \\ 0 & 0 & 0 & 1 \end{bmatrix} \tag{4.15}$$

Table 4.3 Performance of Finite Horizon LQR for Jupiter and Mars prioritizing final conditions errors in weighting matrices. The value $\overline{d}$ denotes the arrival distance to the planet and σ_d its standard deviation.

Planet	Success [%]	Total failure [%]	$\overline{d}$ [AU]	σ_d [AU]	r_{SOI} [AU]
♃	51	26	2.5903	3.9674	0.3222
♂	9	8	0.0723	0.0849	0.0039

We can extract some interesting conclusions from table 4.3. For Mars missions, it is clear that imposing these major restrictions in arrival errors has been counterproductive. It has diminished successful missions and increased failures, with a rise in both mean distance and standard deviation. For Jupiter, results are not much better either. It has accomplished one more successful mission, but at the expense of increasing the number of failures by 5. Both mean distance and standard deviation have also increased. We can learn from these latter simulations that, if we opt for a LQR strategy, we have no real control over the accuracy in

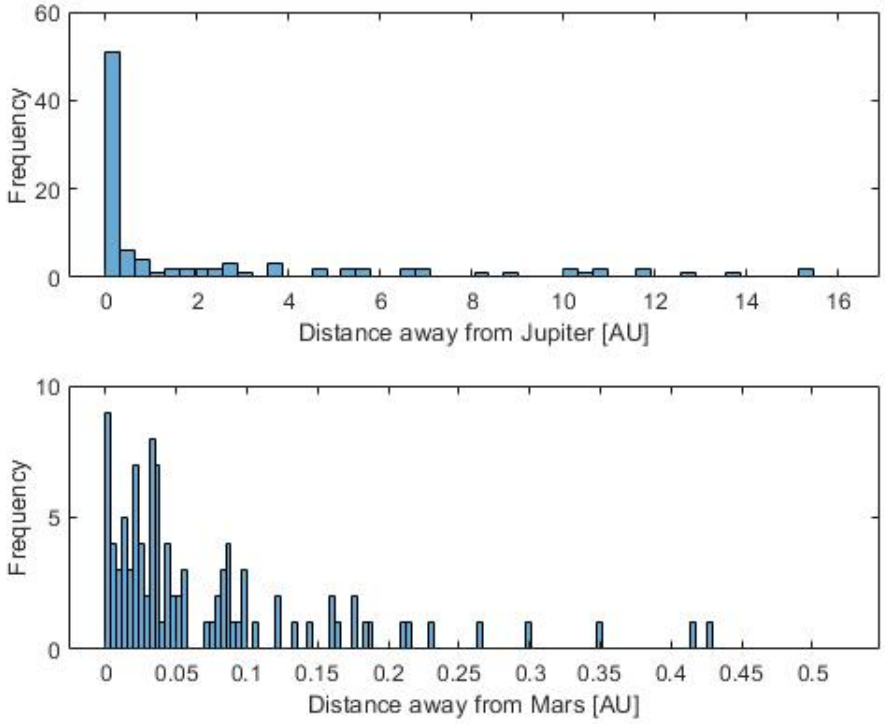

Figure 4.7 Histograms of arrival distance values for simulations to Jupiter (top) and Mars (bottom) with Finite Horizon LQR prioritizing final conditions errors in weighting matrices.

arrival conditions, since an aggressive LQR controller in this regard would also mean that the probability of entering in the saturation positive feedback loop is greater, ending up being counterproductive. This is a major drawback that encourages us to find a new strategy in which we can have more control over arrival conditions. In table 4.4, a table collecting all different LQR simulations results is shown, where − indicates that identity weighting matrices have been used, TL stands for thrust lever and AC for arrival conditions prioritizing strategies.

Table 4.4 Performance of different LQR Control Strategies grouped by planet. The value $\overline{d}$ denotes the arrival distance to the planet and σ_d its standard deviation.

Planet	Strategy	Success [%]	Total failure [%]	$\overline{d}$ [AU]	σ_d [AU]
♃	-	50	21	1.9014	3.1830
	TL	25	11	1.4921	2.1658
	AC	51	26	2.5903	3.9674
♂	-	13	2	0.0536	0.0662
	TL	2	19	0.1183	0.1084
	AC	9	8	0.0723	0.0849

4.2.5 Limitations of LQR Control Strategy

Having tested various sintonizations for our LQR controller, we can extract some conclusions of its behaviour. The first thing that can be highlighted is its gain, $\boldsymbol{K}$ which is, in fact, time-dependent, but its time variation is known since the start of the mission, and its future values are stored to be used when appropriate. This lack of updates of the gain matrix increases the stiffness of the controller, and thus raises the probability of a total failure happening. $\boldsymbol{K}$ is the optimal matrix if our reference are the nominal orbits from Chapter 3. But, due to solar wind perturbations, we may end up considerably far from that nominal path, decreasing LQR's reliability. One thing that could be done in this regard is to solve for the $\boldsymbol{P}$ matrix again in a series of points during the mission that are usually called waypoints [46], that could add some robustness to the system.

Other major drawback is the weak control we have on final conditions. We can try to minimize the arrival errors by increasing the components of $\boldsymbol{Q}_{end}$, but always knowing that this is a rather heuristic approach instead of deterministic. Furthermore, these values can not be raised indefinitely, since that would mean that other kind of errors are directly disregarded, and that could result in saturation problems leading to mission failure. In fact, this is exactly what has happened in our missions.

Lastly, the most critical aspect of using this strategy is that it is, up to some point, unstable. If we happen to get far enough from the nominal orbit, the linear approximation of LQR will not be realistic, resulting in incorrect estimations of control parameters, possibly entering saturation zone. That effectively is a positive feedback loop that can make the spacecraft miss its target catastrophically. To avoid excessive error that can lead to this scenario, one could include an integral term in the LQR formulation, to account for the total error in state variables and act to mitigate it [47]. This may cause even more saturation in the controller, which leads to a delay in LQR response, issue that may be treated by adding an *Anti Windup* strategy [48]. Both implementations are left as future work.

Having seen that LQR fails when the spacecraft recedes a considerable amount from the nominal trajectory, we may want to consider a strategy that recalculates new optimal trajectories during flight, to tackle this misalignment problem.

4.3 Shrinking Horizon Model Predictive Control Strategy

In this chapter we think of another strategy that can lead to better results. The key idea here is that, once we are in flight, when an interval of time has passed, we can solve a NLP problem again to recalculate a new optimal orbit, as [38] suggests. In this new problem, time t_f and arrival angle $\theta\left(t_f\right)$ are fixed, as Equation 4.4 shows. This closed loop control strategy based on trajectory correction is usually referred as Model Predictive Control (MPC) [49]. Particularly, considering that we want to reach a specific target at a given instant of time, we impose final constraints, and each time an iteration passes, we are closer to the final instant, which is fixed, that is equivalent to saying that our time horizon shrinks. This kind of feedback strategy is usually called Shrinking Horizon Model Predictive Control (SHMPC) or Shrinking Horizon MPC, and it is often used in the aerospace industry [50].

4.3.1 New OCP formulation for Shrinking Horizon Strategy

It is typical for spacecrafts to have and operate more than one physically different thrust system. The Esail can be utilized in the majority of the trajectory, but we can think of our spacecraft as also having an autonomous thrust system like ionic propulsion, that is exclusively used for precision maneuvers, when we already are considerably closer to the target [51]. This extra maneuverability helps to further justify the hypothesis of considering that our mission is considered successful if it reaches the sphere of influence of the planet. Having a high thrust system, it is also possible to modify our velocity by a significant amount. Because of this, we can leave some margin in the arrival flight path angle γ_f. Flight path angle is defined as the angle between the velocity vector of a body and the tangential direction at that point. Even if it is not exactly 0 (as it should be, because the planets' orbits are assumed circular), it can be corrected using other more conventional propulsion systems.

Therefore, it is proposed to use the arrival flight path angle as the cost function. We want to minimize the difference between the real angle and what it should be (0), so to do that, we square the function, minimizing $\gamma^2\left(t_f\right)$. The flight path angle can be computed by applying the *arctangent* function to the radial and tangential components of velocity. Given that arctangent is an expensive function, we can instead minimize the square of arrival radial velocity, $v_r^2\left(t_f\right)$, since v_r is one of our state variables, and for the ideal case, null v_r, γ is necessarily 0. Thus, our cost function is now expressed as

$$J = v_r^2\left(t_f\right) \tag{4.16}$$

This squaring strategy proves to be an extraordinarily efficient way to add error minimization to cost functions. It is, in fact, one of the motivations of finding solutions to optimal control problems with quadratic error functions, such as the LQR presented in the section above. If final radial velocity should equal to a

nonzero value v_{r_f}, the cost function would then be defined as $J = \left(v_r\left(t_f\right) - v_{r_f}\right)^2$.

As it can be observed, there is no information of the nominal orbit in the cost function. In this strategy, the nominal solution only intervenes by providing the values of t_f^{nom} and θ_f^{nom}, necessary to impose the arrival restrictions in (4.4). A prior calculation of the nominal orbit is a way to ensure that the time and true anomaly values that we are fixing are adequate and feasible for the problem. The nominal orbit is also used as the initial guess in the first orbit calculation. From there, each time a new orbit has to be computed, it uses the most recent orbit as its initial guess. This offers an effective way of adding robustness to the algorithm. Even if the new orbit is not equal to the old due to solar wind perturbations, it should not be too far from it, so it provides an efficient starting point.

The complete optimal control problem that we solve in this section is presented in equations 4.17.

$$
\begin{aligned}
&\min_{\tau,\alpha_n} \quad v_r^2\left(t_f\right) \\
&\text{subject to} \\
&\qquad \begin{aligned}
\dot{r} &= v_r \\
\dot{\theta} &= \frac{v_\theta}{r} \\
\dot{v_r} &= \frac{v_\theta^2}{r} - \frac{\mu}{r^2} + \frac{\kappa}{2}\left(\frac{r_\oplus}{r}\right)\left(1+\cos^2\alpha_n\right) \\
\dot{v_\theta} &= -\frac{v_r v_\theta}{r} + \frac{\kappa}{2}\left(\frac{r_\oplus}{r}\right)\cos\alpha_n \sin\alpha_n
\end{aligned} \\
&\qquad \begin{aligned}
0 \leqslant \kappa(t) &\leqslant \kappa^{max}(t) \qquad\qquad t \in \left[0, t_f\right] \\
-\alpha_n^{max} \leqslant \alpha_n(t) &\leqslant \alpha_n^{max}
\end{aligned} \\
&\qquad \begin{aligned}
r\left(0\right) &= r_\oplus \\
\theta\left(0\right) &= 0 \\
v_r\left(0\right) &= 0 \\
v_\theta\left(0\right) &= v_\oplus \\
r\left(t_f\right) &= r_i \\
v_r^2\left(t_f\right) + v_\theta^2\left(t_f\right) &= v_i^2 \\
t_f &= t_f^{nom} \\
\theta\left(t_f\right) &= \theta_f^{nom}
\end{aligned}
\end{aligned}
\tag{4.17}
$$

Where, as done previously, i denotes the planet we are referring to, $i =$ ♂, ♃. As discussed when calculating nominal optimal orbits in Chapter 3, we discretize the time domain of this problem into 500 segments. Note that there is an extra constraint in (4.17) that fixes the arrival speed modulus equal to the velocity of the planet. Now, we set $a_c = 0.6$ mm/s^2, utilizing its maximum available value. However, κ^{max} is time-dependent and its evolution is unknown, since it is given by the value of $p_\oplus$. We deal with this using the same approach as used in the LQR strategy. We define 20 intervals of constant dynamic pressure for Mars, and 50 for Jupiter. These periods of constant dynamic pressure are referred as arcs from now on. At the start of each arc, we extract a value of $p_\oplus$ from the Gamma distribution, and use it to calculate the value of κ^{max} as

$$\kappa^{max} = a_c \sqrt{\frac{p_\oplus}{\overline{p}_\oplus}} \tag{4.18}$$

4.3.2 Strategies under low solar wind conditions. Full thrust arcs

There are a variety of considerations that we can make in regard to $\kappa^{max}(t)$, particularly for when t is not contained in the actual constant dynamic pressure arc. Suppose we have just updated $p_\oplus$ and therefore also κ^{max}. It is reasonable to establish that, during the current arc, the saturation value for thrust lever should be

κ^{max}. However, it is not obvious which value should be used for the rest of the orbit recalculation. If, for example, $p_\oplus$ turns out to be low, and we use the same κ^{max} for all the trajectory recalculation, we may end up with an infeasible situation where the algorithm is not able to find any solution, because with such low thrust it is not possible to reach the target in the fixed amount of time and true anomaly angle. On the other side, if $p_\oplus$ happens to be large, and we use the same κ^{max} recently computed for the rest of the orbit, that may result in a new orbit that demands a high amount of thrust at the last arcs of the flight, which are the most critical. The higher the thrust is predicted to be, the more likely the saturation value will actually limit it, and given that that can happen at latter arcs of the mission, we can well incur again into an infeasible situation. Another approach that can be taken is to use the mean value of $p_\oplus$ (denoted $\overline{p_\oplus}$), which would lead to a mean value of thrust lever denoted as $\overline{\kappa^{max}} = a_c$, for calculations outside the current arc. Yet another justified method would be to not to use the current mean value of thrust lever, but the nominal mean value, that is, $\kappa_{nom}^{max} = a_{c_{nom}}$, or maybe one in between, that could for example be the arithmetic mean between both. Ultimately, the idea is to find an equilibrium between not having such low thrust limit so that we incur into an infeasible situation at the current interval, but not having such large thrust limit which amkes infeasibility very likely in later arcs.

Another important detail to think about is how to proceed if, in fact, the optimization algorithm returns an infeasibility error. The worst case scenario is, obviously, the failure of the mission, which we have to avoid at all costs. We can ask ourselves how can this infeasible scenario happen, since it is the algorithm's way of saying that the problem can not be solved with the restrictions and initial guesses that we gave it. If an arc in which dynamic pressure is large happens, even if κ^{max} increases, the algorithm would not have any problem to deal with it, since it can simply not apply full thrust and thus accomplish the rendezvous at the correct moment. The opposite is not true. If an arc with really low dynamic pressure happens, even applying full thrust at every instant of time may not be sufficient to reach our target. It is in these latter scenarios where the infeasibility situation occurs. Of course the probability of this happening decreases as control margin rises, but the increase in the mission duration may not be worth it. The best we can do when this problem appears is to fly at full thrust during the arc, and hope for a higher value of $p_\oplus$ in the next one that allows us to find a new optimal trajectory again, thus avoiding the infeasible scenario.

We can then determine that, if an infeasible scenario appears during one of the dynamic pressure recalculation arcs, we can exit the closed loop strategy during this time span and go into what we can call a *full thrust arc*, where $\kappa = \kappa^{max}$. The strategy to apply to α_n during that arc is far from being obvious. We may want to obtain maximum thrust cone angle, since that appears to be a good compromise between gaining radial and tangential velocity. But we could also set α_n to 45°, since that provides maximum tangential acceleration. One last logical strategy would be to set the sail pitch angle to 0. With that strategy, we obtain maximum thrust modulus, and most importantly, we can move further from the Sun to avoid the excessive gain of true anomaly due to a larger tangential velocity, which can be way larger than what the Esail maneuverability can counteract, as seen in Chapter 4.1.2. There is no apparent preference for any of these strategies, so we conduct three different studies with multiple simulations and analyse the results, opting for the one that yields the best performance.

However, this strategy is not infallible. It may not be the case that the orbit can be recalculated after a *full thrust arc* (that is to say that the algorithm continues to return an infeasibility error). If that happened, then the spacecraft would enter again in another full thrust arc. This raises an important problem. Since full thrust arc strategy does not carry any kind of information about the nominal orbit, it is probable that, if the spacecraft combines multiple arcs like this in a row, it will only deviate more from where it should be, aggravating the infeasibility situation and entering a positive feedback loop from where it can not escape, resulting in mission failure, with a totally different orbit from the planned. This is why we conduct several studies for each case.

To do these first studies, we run 100 simulations for each of the three full thrust arc strategies; α^{max}, a_t^{max} and a_r^{max}. We fix Mars as our target first for simplicity (with LQR simulations we saw that, even if results can vary between planets, the trend is generally followed by both), and use a thrust lever value for future recalculation intervals of $\kappa^{max} = 0.8\,a_c$, since it is an acceptable middle value (the arithmetic mean) between κ_{nom}^{max} and κ^{max}. Later, when the strategy for full thrust arc is fixed, we also conduct various studies for different values of κ^{max} in future time intervals. In Appendix A, a flowchart of the basic functioning of the program used to solve the closed loop control problem is included. It uses a particular notation for simplicity. The value n_ξ refers to the total number of arc recalculations, while ξ refers to the number of the arc we are currently in. This same nomenclature appears in the *Notation* Section, and is maintained for the

rest of this Chapter.

Having conducted a total of 300 simulations, we can extract some conclusions from the data obtained, collected in table 4.5.

Table 4.5 Performance comparison for Shrinking Horizon MPC for various *full thrust arc* strategies. The value $\overline{d}$ denotes the arrival distance to the planet and σ_d its standard deviation.

Strategy	Success [%]	Total failure [%]	$\overline{d}$ [AU]	σ_d [AU]
α^{max}	52	9	0.0591	0.1226
a_r^{max}	32	14	0.1177	0.2836
a_θ^{max}	56	12	0.0585	0.1386

We can see that the worst strategy is clearly the second, the one that implies zero thrust coning angle in full thrust arcs. The other two strategies, on the contrary, work considerably better. The first one achieves 52% success rate with only 9% of total failures, while the third reaches 56% in success rate at the expense of a slight increase up to 12% of total failures. It is also shown that, in the first strategy, although the mean of the distances is a bit higher, its standard deviation is lower. That, joined to the fact that it is more convenient to end up relatively far from your target but being able to reach it, rather than totally missing it, inclines us into opting for the first strategy for our next simulations. Therefore, α_n is fixed to arccos $\frac{1}{\sqrt{3}}$ in full thrust arcs. Ideally, we would conduct all future studies using these three strategies, and opt for the one that yields the best performance in each case, which may depend, although not probable, on κ^{max}. However, we do not do that because of the same reason explained in the LQR Control Strategy. Such an approach is highly computationally demanding, and is out of the scope of this work. Histograms of simulations for each of the three full thrust strategies are included in figure 4.8. Distance axis has been limited to a maximum value of 0.3 AU for readability, although there are some values that land outside that region.

4.3.3 Strategies for trajectory determination in future time arcs

Now that full thrust arc strategy has been fixed, we can conduct various studies considering different manners to predict future time interval orbits, as exposed previously.

Firstly, we discard some strategies that may seem reasonable in the beginning, but yield bad results. For example, using the same current saturation value given by $p_\oplus(t)$ not only for the current time interval, but for the rest of the trajectory is not a great idea. If we do that, and we enter a large dynamic pressure interval, there is no way of telling the algorithm that, of all possible thrust distributions, it is convenient to use the one that maximizes the usage of thrust in the current time interval, since in future intervals that limit will probably be lower. Therefore, it is not rare to fall into an infeasible situation, scenario that we have to avoid whenever possible.

It is not a great idea to use nominal thrust saturation value for future intervals either. That means that, if at some point we incur in a low dynamic pressure interval, it is highly probable that we will again fall into an infeasible scenario. That is because, if we can not use all thrust predicted in the current interval, we will have to use more of it in the future to compensate, but if future saturation value is fixed at the nominal, then it will be intrinsically impossible to use more thrust than originally predicted at any point, hence the infeasibility error.

It appears to be a reasonable option to use the mean value of a_c for future calculations, that is, $\kappa^{max} = 0.6$ mm/s^2. The only drawback is that, as we can see in figure 4.1, the possibility of thrust lever being lower than that mean value is 60%. Because of that, it may be a good option to use a value in between, not the 60% of the characteristic acceleration (value used for the nominal orbit calculation), nor 100% of it, but, for example, its arithmetic mean, the 80 % of the characteristic acceleration, which is $0.8 \cdot 0.6 = 0.48$ mm/s^2. Moreover, the most critical phase of the mission is the arrival. One noticeable perturbation near the planet can lead to considerable arrival errors. Therefore, we may use a linear distribution, using 0.48 mm/s^2 for future calculations at the first iteration, and 0.6 mm/s^2 at the penultimate (in the last iteration, there are no future intervals). In total, we consider four different strategies to approach orbit determination for future time intervals, listed below.

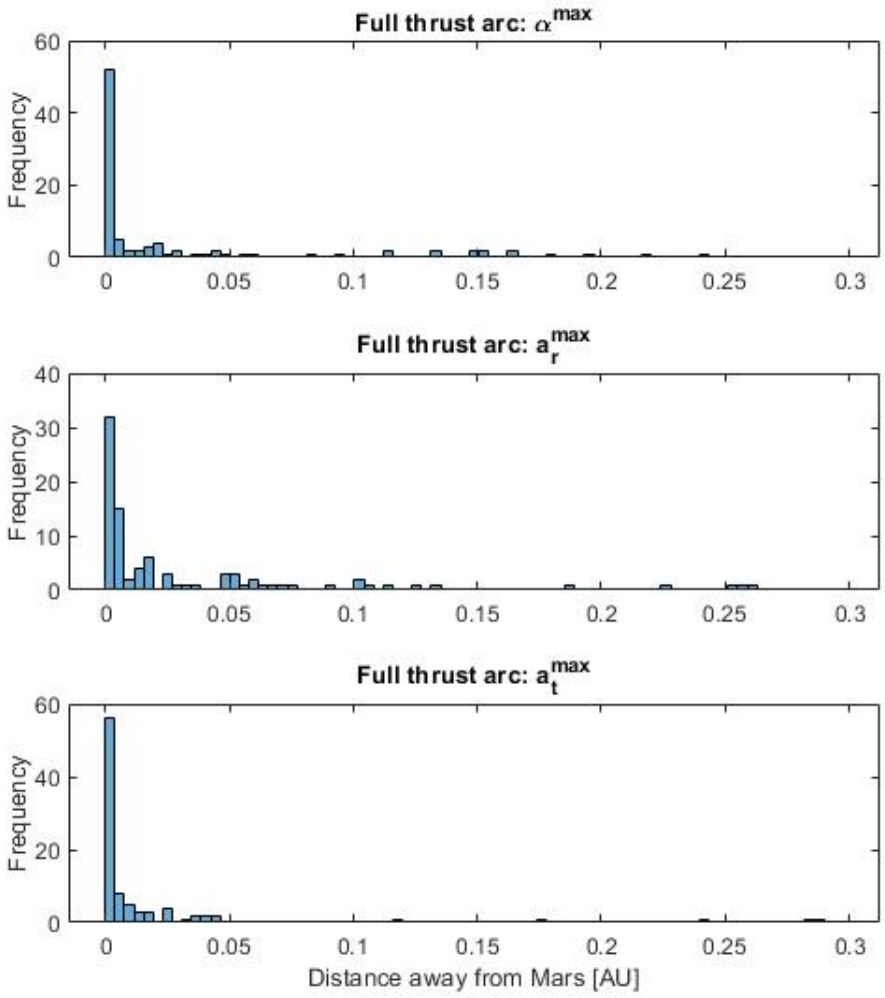

Figure 4.8 Histograms of arrival distance values for simulations to Mars with SHMPC using maximum thrust cone angle (top), maximum radial thrust (middle) and maximum tangential thrust (bottom).

- Usage of nominal thrust lever as the saturation value, $\kappa^{max} = 0.36$ mm/s^2, denoted as *Nominal*.
- Usage of mean current thrust lever as the saturation value, $\kappa^{max} = 0.6$ mm/s^2. We call this strategy *Current* from now on.
- Usage of mean value between nominal thrust lever and mean current thrust lever as the saturation value, $\kappa^{max} = 0.8 \cdot 0.6 = 0.48$ mm^2. We refer to this strategy as *Mean*.
- Usage of linearly increasing thrust lever saturation value between *Current* and *Mean*. This can be expressed as in equation 4.19, where n is the number of the current time interval and N the total number of intervals. This strategy is denoted as *Linear*

$$\kappa^{max} = 0.48 + \frac{n-1}{N-1}(0.6 - 0.48) \quad [\text{mm/s}^2] \tag{4.19}$$

Having run all these simulations, we collect their performance data in table 4.6 to compare them, along with their corresponding histograms for arrival distance in figure 4.9.

In table 4.6, even if the *Nominal* strategy is able to perform 1% better in terms of successful missions, it also fails almost three times more often. Comparing mean distance and standard average values, they strongly

Table 4.6 Performance comparison for Shrinking Horizon MPC for different κ^{max} for future intervals. The value $\overline{d}$ denotes the arrival distance to the planet and σ_d its standard deviation. The value $\overline{d}$ denotes the arrival distance to the planet and σ_d its standard deviation.

Strategy	Success [%]	Total failure [%]	$\overline{d}$ [AU]	σ_d [AU]
Nominal	53	21	0.3310	0.8130
Mean	52	9	0.0591	0.1226
Current	19	29	0.1673	0.2365
Linear	35	15	0.0758	0.2083

differ from the rest. This is the reason why it is preferred to use the *Mean* strategy over the *Nominal* one, to increase reliability. We confirm that our assumptions are correct, the mean value between the nominal and the current thrust is a good compromise value between avoiding infeasibility in the current arc and not restricting too much the latter arcs, converting the *Mean* strategy in the best of all the tested ones. The *Current* strategy yields noticeable worse results, and an increasing linear strategy does not appear to make much of a difference either.

4.3.4 Shrinking Horizon MPC simulation results

Having established *Mean* as the best strategy for updating the orbit in future time intervals, and α^{max} law as the best one during full thrust arcs, we now run the corresponding simulations for Jupiter and present in table 4.7 the performance results for both Mars and Jupiter with this configuration. Examples of successful trajectories to Mars and Jupiter using this control law are included in figure 4.10 and 4.11. These examples have been chosen on purpose, since they both include one arc in which the problem becomes infeasible and the program had to execute a full thrust arc, which is easily recognizable because it uses constant maximum thrust lever and constant $\alpha_n \approx 55^\circ$. After that arc, the program was able to find a solution again. These infeasible arcs happen, as expected, when dynamic pressure is unusually low, becoming more sensitive as we approach the target. Note that bang-bang control in κ does not appear anymore in these trajectories, and it is due to the fact that we are no longer dealing with a time-optimal problem. The discontinuities seen are the borders between different arcs, so there is a different $p_\oplus$ in each of them and thus, a different κ^{max}. This difference in the problem constraints explains the sudden discontinuities seen. Unsuccessful missions can be consulted in Appendix B, along with a brief description of the results.

Table 4.7 Performance final results for missions to Mars and Jupiter with an optimal Shrinking Horizon MPC Strategy. The value $\overline{d}$ denotes the arrival distance to the planet and σ_d its standard deviation.

Planet	Success [%]	Total failure [%]	$\overline{d}$ [AU]	σ_d [AU]
♃	89	8	0.5578	1.8079
♂	52	9	0.0591	0.1226

We can now compare the performance results with the obtained using the LQR controller. Of all the LQR weighting matrices configurations simulated for Mars and Jupiter missions, we opt for unit diagonal weighting matrices, since as seen in Chapter 4.2, it is the configuration that yields the best performance. All these results are collected in table 4.8.

Table 4.8 Performance comparison between LQR Control and SHMPC Strategies. The value $\overline{d}$ denotes the arrival distance to the planet and σ_d its standard deviation.

Planet	Strategy	Success [%]	Total failure [%]	$\overline{d}$ [AU]	σ_d [AU]
♂	LQR	13	2	0.0536	0.0662
	SHMPC	52	9	0.0591	0.1226
♃	LQR	50	21	1.9014	3.1830
	SHMPC	89	8	0.5578	1.8079

The comparison that can be done for a Mars mission between LQR and SHMPC is of great value. Shrinking Horizon MPC Strategy achieves a 52% success ratio, compared to the modest 13% that LQR control yields.

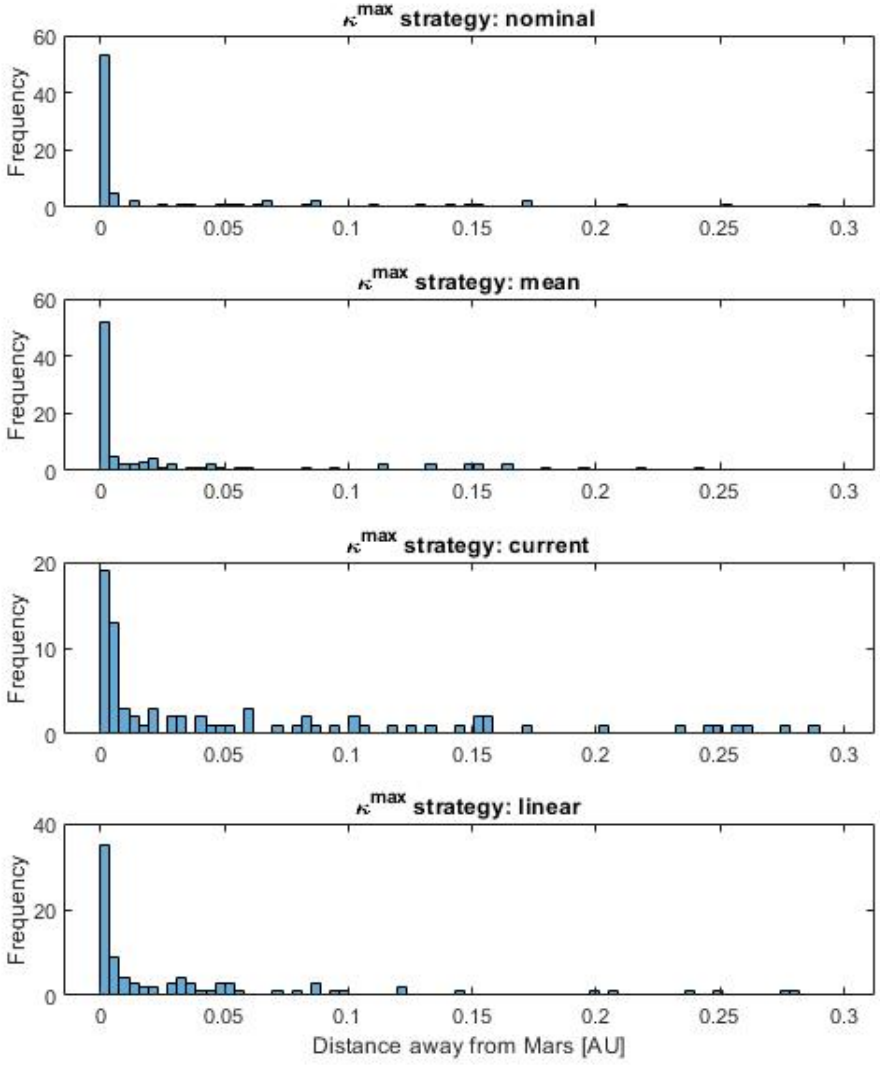

Figure 4.9 Histograms of arrival distance values for simulations to Mars with SHMPC using different strategies for κ^{max}, from top to bottom: *Nominal*, *Mean*, *Current*, *Linear*.

However, with SHMPC, failed missions become more common, a 9% agains the 2% of LQR. It can also be seen that the mean arrival distance to the planet is smaller, although not by much, for the LQR. On the contrary, difference in standard deviation is highly noticeable; it is almost doubled for SHMPC. The best strategy depends on what we focus on. If our mission is sensitive to arrival distance, it may be better to opt for SHMPC, but if as much reliability as possible is desired, the best option would be to use LQR, which would typically be the case.

For a Jupiter mission, there is no doubt, SHMPC is clearly better. A mission to Jupiter is more demanding than one to Mars because of its superior duration and ease to propagate instabilities. SHMPC is still not a stable algorithm, but it appears that updating the orbit adds robustness to it, making it more probable for our spacecraft to reach our target.

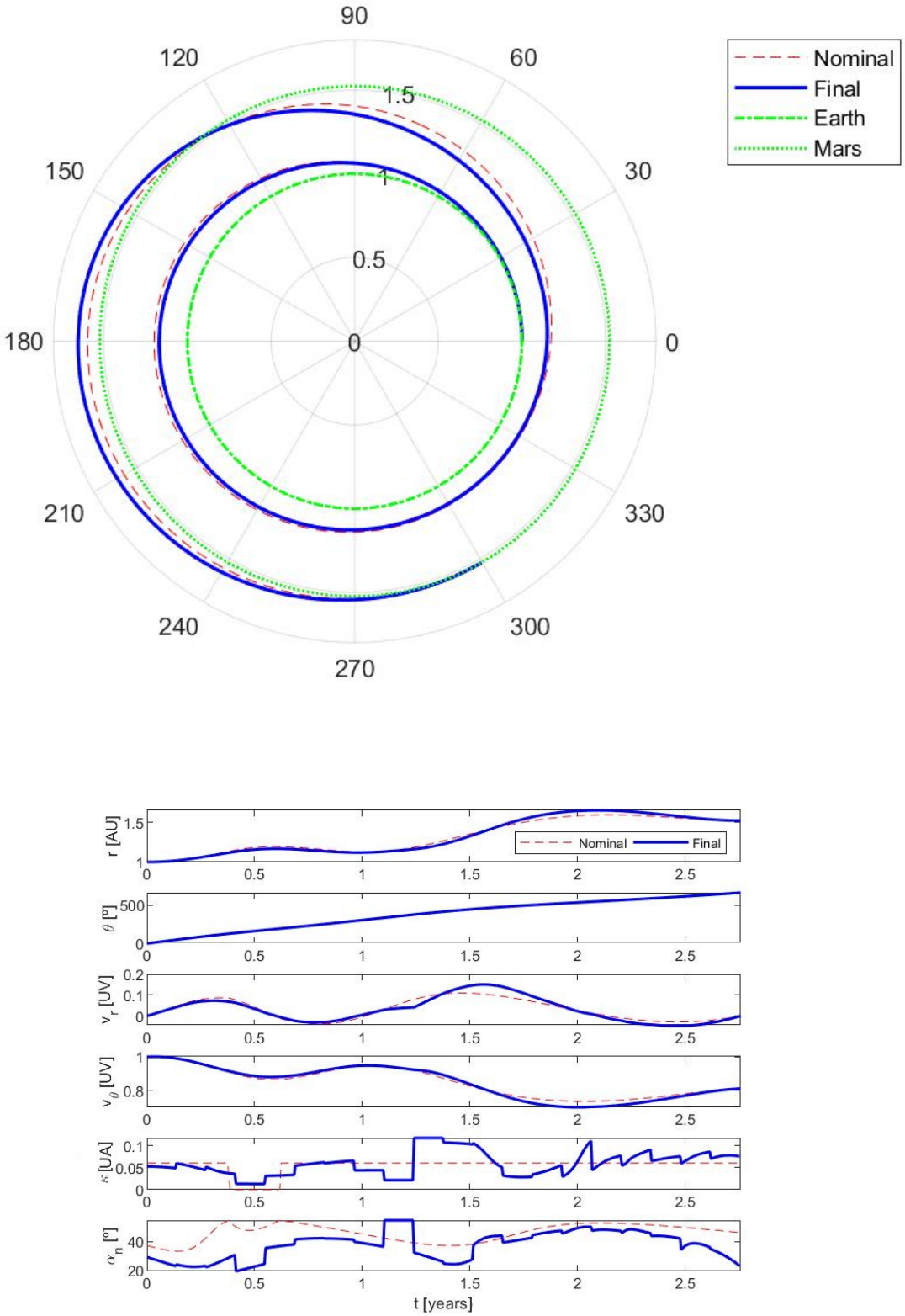

Figure 4.10 Trajectory and evolution of state and control variables in a successful mission to Mars using optimal Shrinking Horizon MPC.

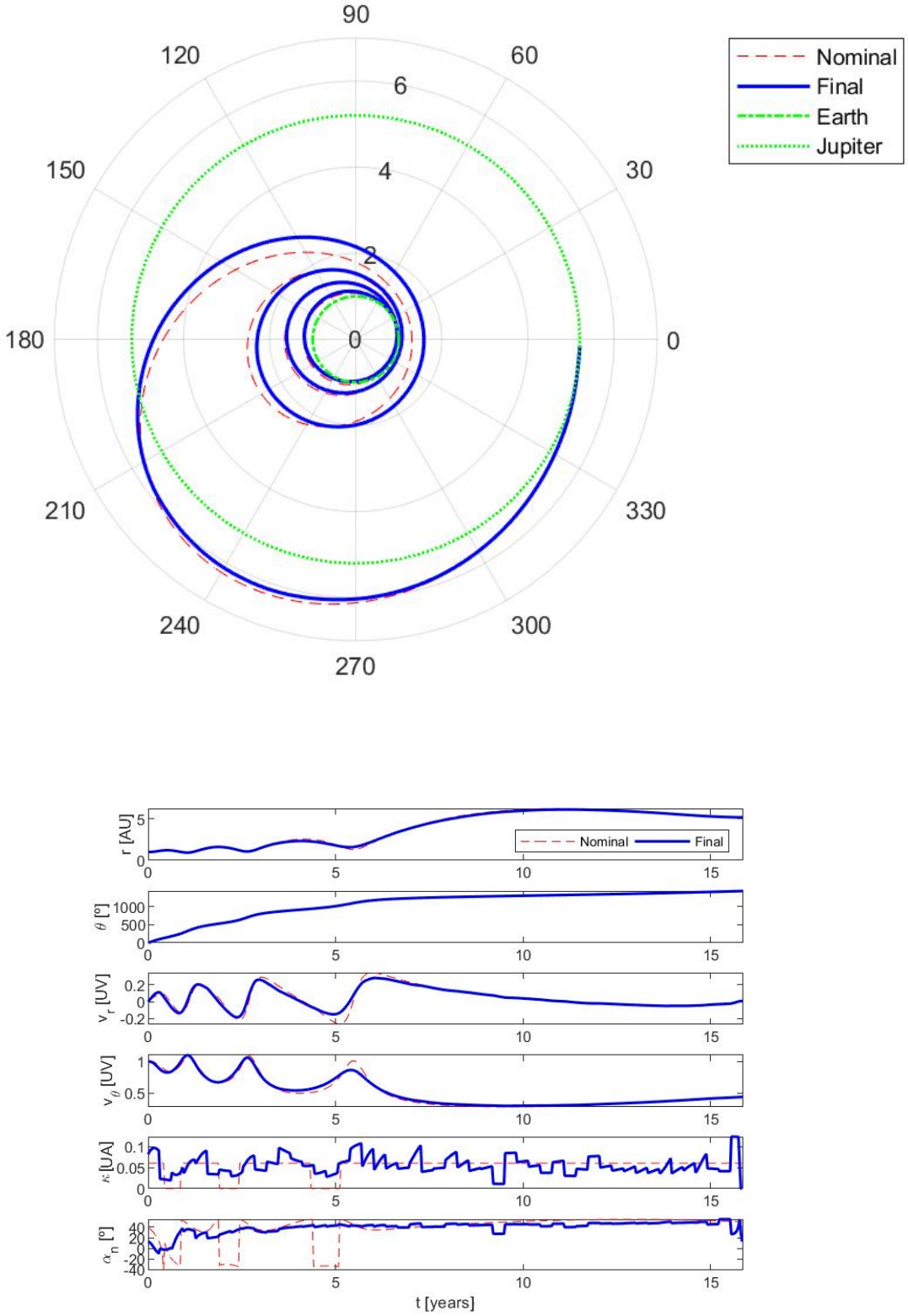

Figure 4.11 Trajectory and evolution of state and control variables in a successful mission to Jupiter using optimal Shrinking Horizon MPC.

We have to remember that, with this Shrinking Horizon MPC Strategy, the spacecraft achieves perfect arrival conditions in position each time it does not fall in a full thrust strategy at the last arc. Unlike LQR control, we have, in that sense, a total dominance over final conditions with this new strategy. However, since our strategy not only contemplates Shrinking Horizon MPC, but also full thrust arcs when it is not possible to find an optimal orbit, we have still not found a stable law that guarantees arrival and that can not fall into a positive feedback loop.

4.3.5 Limitations of Shrinking Horizon MPC Strategy

Having conducted numerous analyses for the Shrinking Horizon MPC Strategy, we can extract some conclusions from the results gathered, and try to use them to find a yet better strategy for our problem.

The first advantage, compared to LQR strategy previously used, is that, assuming we do not encounter infeasibility errors at the arrival, we can set exact final conditions. Spacecraft missions need to have high accuracy. However, the conditions may not be verified if we fall into a full thrust arc at the end of the mission.

SHMPC has proven to be more effective than LQR in missions to Jupiter. It adds a level of robustness that LQR does not possess, and it is able to counteract large solar wind variations. The probability of falling into an infeasible arc depends on whether dynamic pressure becomes very low, and also on the proximity to the end of the mission when such an event happens. This latter factor is responsible for the majority of full thrust arcs. It is not ideal to fall into these arcs, but given that they happen, it is better they do at the end of the mission so the spacecraft has less time to deviate considerably from the nominal trajectory.

Although SHMPC can be considered an improvement if we compare it to the LQR method, it still has an undesired aspect. We have managed to theoretically arrive to the target with exact final conditions, if all the optimizations carried out are feasible. Nevertheless, we still suffer from the positive feedback closed loop phenomenon explained before. As we have seen, a low dynamic pressure at some arc, if it is not near the arrival, is certainly not the first concern. The instability that the problem may present when the spacecraft is near the target is the issue we want to tackle. Recalling that we want to accomplish a rendezvous maneuver, we can know the orbit the spacecraft needs to have in the future, since it has to be the same one as the corresponding planet's, which is known. If we find a way to extend this arrival instant in time, we may find the stability property we are searching for. These are the motivations for the strategy presented in the next section.

4.4 Receding Horizon Model Predictive Control Strategy

So far, we have come up with strategies that either reach the target, oe miss it. By the way of how LQR control and MPC strategies were formulated, fixed arrival time was mandatory. This condition implies that we can not implement any kind of arrival trajectory correction to ensure that we reach the objective, even if it is in a significant greater amount of time. However, considering typical space missions, reaching the target is much more important than the time spent reaching it. Let us introduce the example of Jupiter. It is better to spend two or three years maneuvering if we happen to be considerably far because of solar wind perturbations, rather than missing it, and having to do a kind of a phasing maneuver[1], because Jupiter takes twelve years to complete an orbit around the Sun.

All these arguments indicate that it would be useful to find an strategy that lets us extend the time domain of the problem. The idea is to solve an optimization problem in which the cost function is the spacecraft's arrival error (typically only position errors), but with the addition of extending that error into the future. The key aspect to notice is that, reaching Jupiter yields the position constraints, and wanting to stay exactly in Jupiter's orbit yields the velocity constraints. But another way to impose those velocity constraints (in a weak formulation) is to extend the error in time. If we minimize not only the arrival position error, but a sum of the position error at that instant and in the future, we can be sure that velocities will converge to the correct values, since this is the only way to minimize the cost function to its lowest possible value. This approach, in

[1] A phasing maneuver is a maneuver of typically two impulses (one at the start and one at the end) in which the spacecraft ends in the same orbit in which it was prior to the maneuver, but with a different true anomaly. It is usually performed to achieve a rendezvous with another body, and its duration is of the order of the orbit's period.

which time horizon does not shrink, but rather slides, is often called a Receding Horizon Model Predictive Control (RHMPC) or Receding Horizon MPC Strategy [52].

4.4.1 New OCP formulation for Receding Horizon MPC Strategy

Since we want to extend the trajectory into the future in this strategy, let us first define some nomenclature. The problem is divided into a series of intervals in which it is discretized, and each of the two ends of those intervals constitute the nodes in which state variables are evaluated. This number of segments is initially 500 in our problem, and it is denoted as N as already presented in Chapter 3. We refer to a particular interval of total N using η. This N value must not be confused with the number of arcs into which the problem is divided, updating dynamic pressure and trajectory at the start of each of them. This arc number is denoted as n_ξ, and its value is originally 50 for Jupiter and 20 for Mars. We refer to a particular arc using simply the letter ξ. Since we have the number of time intervals N, and the number of arcs ξ, we can compute the number of time nodes that there are in each arc as $N_\xi = N/n_\xi$.

For the cost function, the idea is to integrate the error over a future time interval, in terms of position error. Since we are using polar coordinates, that error can be expressed in terms of the radius and true anomaly. In a general form, the cost function looks as

$$J = \int_{\max(t_f^{nom}, t_{curr})}^{t_f^{nom}+T_{add}} \varepsilon\left[r(t), \theta(t), r_p, \theta_p(t), t\right] \mathrm{d}t \tag{4.20}$$

Where ε is some position error measuring function. Its explicit time dependence is due to the fact that the function may be subject to weighting, which can depend on time. We define T_{add} as the time an arc lasts multiplied by the number of the current arc the spacecraft is in. That means that its value changes in each arc (and thus, in each trajectory correction). The idea is to maintain, as the name suggest, a receding horizon, so that when we reach a previous time horizon, there is already a new one in the future that serves us as a reference. To do so, each time we advance to the next arc, we must increase the domain of the integral into the future by the same time span. The variable t_{curr} refers to the current time, and is introduced to avoid integrating over the past (since those values can not be changed) when we surpass the predicted arrival time without reaching the target due to solar wind perturbations. Recalling the discretization of our OCP into a NLP, we can more precisely describe our cost function as

$$J = \sum_{\eta=\max(N+1,\, \eta_{curr})}^{N+1+N_\xi(\xi-1)} \left[w(\eta)\, \varepsilon\left[r(\eta), \theta(\eta), r_p, \theta_p(\eta)\right]\right] \tag{4.21}$$

Note that η is the analogous to t in the discrete version. We define Δt as the step size of our problem, that is, the time between two consecutive η, or $\Delta t = t_f^{nom}/(N+1)$. The parameter $w(\eta)$ is the time-depending weighting function mentioned earlier, therefore, ε no longer depends on t or η. Note also that the radius of the planets orbit is a constant (r_p), but its true anomaly is not, it depends on time, following (4.22), the discrete analogous of (4.5).

$$\theta_p(\eta) = \theta_f^{nom} + n_p \Delta t\, (\eta - (N+1)) \tag{4.22}$$

The exact definition of ε to optimize performance is not obvious, and a section is dedicated to the particular formulation of the cost function in that regard.

In terms of constraints, we continue to have fixed initial conditions. However, for final conditions, nothing is fixed, the idea is to add them to the cost function, so the distance to the target can be minimized. The only strong final condition imposed in this formulation is, logically, final simulation time, although it no longer corresponds to arrival time, and it depends in the arc number we are in, following

$$t_e = t_f^{nom} + \Delta t\, N_\xi\, (\xi - 1) \tag{4.23}$$

One should not confuse t_e and t_f. The value t_e refers to the ending simulation time (the time horizon for RHMPC calculations), which is not the same as t_f, the time instant in which we reach the corresponding planet. Each time a new orbit is updated, it uses the orbit from the previous calculation as the initial guess,

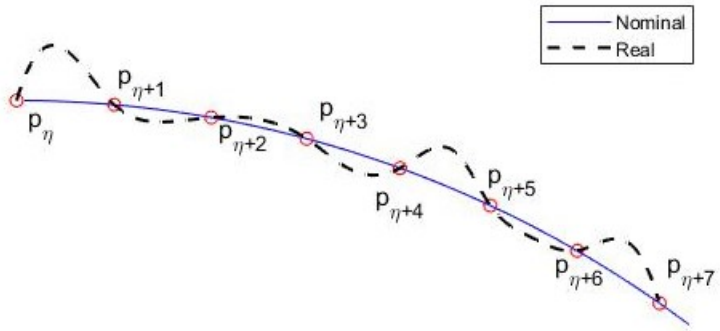

Figure 4.12 Trajectory oscillations due to cost function evaluating distance between points.

since we know for a fact that this orbit must be near the new solution, just as done in Shrinking Horizon MPC. A slight modification has to be made in this case, since we are extending the orbit into the future, so there are required initial guess values that do not appear in the previous orbit. We have found that a robust way to tackle this is to use the values of the last point in the previous orbit, and use them as initial conditions to extend the orbit by following the dynamic equations.

The stopping criteria for this problem is, again, entering the planet's sphere of influence. For the $n_\xi - 1$ first orbit updates this proximity is not even checked, since we are still not in the region in which the cost function is trying to minimize the error (In these arcs, $t < t_f^{nom}$ still). From this point on, each time an arc finishes, we calculate if there is any point in this last arc in which the spacecraft is inside the sphere of influence. In case there is, the program execution stops, otherwise, another arc is added, and the process is again repeated, extending the flight time of the mission. A simple flowchart of this algorithm can be seen in Appendix A. Note that the number of time intervals and constant dynamic pressure arcs are not known anymore. The variables N and n_ξ refer to the number of them at the start of the problem, but if the spacecraft reaches t_f^{nom} and is not still in the sphere of influence, another arc will be added. If we encounter us having to add k arcs before the spacecraft completes the mission, the problem ends up having $n_\xi + k$ arcs, and $N + 1 + N_\xi\, k$ time nodes (or $N + N_\xi\, k$ intervals).

4.4.2 Cost function definition

There is no simple way of determining which cost function we should use to maximize the performance of our method. It is certain that it has to depend of the spacecraft and planet positions at each instant, but how we measure that error is not totally determined. Note that we have to be careful with its definition. If we just set the cost function to minimize the error in a certain set of points (each of our η), the algorithm may find an oscillating path that is able to minimize that error, but differs significantly from the nominal path between points, as it can be seen in figure 4.12. In that case, special cost functions measuring distance to segments instead of points may be necessary [53]. However, due to our highly limited maneuverability, this oscillation issue does not appear in our problem, so this cost function modification is not considered.

We may, as a first guess, think of minimizing both radius and true anomaly errors, with equal weighting for both. To reduce this error, in a manner that is computationally efficient for the algorithm, we can use difference of squares, nondimensionalized with the reference planet's values in order to get errors of the same order of magnitude, so theoretically the algorithm is not biased, and gives the same preference to both when optimizing. There is also no weighting in time, so for this case $w(\eta) = 1$ Such a cost function, denoted by J_1, is defined as

$$J_1 = \sum_{\eta=N+1}^{N+1+N_\xi(\xi-1)} \left[\left(\frac{r(\eta) - r_p}{r_p} \right)^2 + \left(\frac{\theta(\eta) - \theta_p(\eta)}{\theta_p(\eta)} \right)^2 \right] \tag{4.24}$$

We may now think of the repercussion an error can have in the distance to the planet. If, for example, we have no error in θ but an error of 0.1 AU in r, the we will obviously be 0.1 AU far away from our target. If we suppose that we have no radial error, but an error of 0.1 rad (they are not the same units, but they were nondimensionalized in the cost function), then for a reference distance of $r_p = 3$ AU, a middle value between

Mars and Jupiter, the distance from the target is now 0.3 AU, three times more. That is a reasonable argument to privilege angular error in our cost function. Joined with the fact that it is easier for the Esail to correct radial position compared to angular error, we can make a modification of our cost function with weighted errors, as

$$J_2 = \sum_{\eta=N+1}^{N+1+N_\xi(\xi-1)} \left[\left(\frac{r(\eta) - r_p}{r_p} \right)^2 + 5 \left(\frac{\theta(\eta) - \theta_p(\eta)}{\theta_p(\eta)} \right)^2 \right] \tag{4.25}$$

We refer to this cost function as J_2. One last possibility can be to not think about r and θ errors, but distance as a whole. In polar coordinates, we can compute the distance between two points $(r_1, \theta_1), (r_2, \theta_2)$ with

$$d = \sqrt{r_1^2 + r_2^2 - 2r_1 r_2 \cos(\theta_2 - \theta_1)} \tag{4.26}$$

The square root is a computational expensive function, and we can avoid its usage by minimizing d^2 instead of d, since $f(x) = x^2$ is an increasing function $\forall x \in (0, \infty)$. With these considerations, we can construct a new cost function denoted J_3 as

$$J_3 = \sum_{\eta=N+1}^{N+1+N_\xi(\xi-1)} \left[r_p^2 + r^2(\eta) - 2r_p r(\eta) \cos\left(\theta_p(\eta) - \theta(\eta)\right) \right] \tag{4.27}$$

A contour representation of these three functions for the case of Mars and Jupiter can be seen in figure 4.13. The values in which contour curves have been evaluated are proportional and have been escalated accordingly so graphs are of similar sizes. It can be seen that functions J_1 and J_3, although not equal, do not differ by too much. J_2 shrinks contour curves in the direction of θ, that means that it privileges the minimization of this value. The dashed line represents the planet orbit, and the direction of Sun is southwest, towards (0,0) point in both axes.

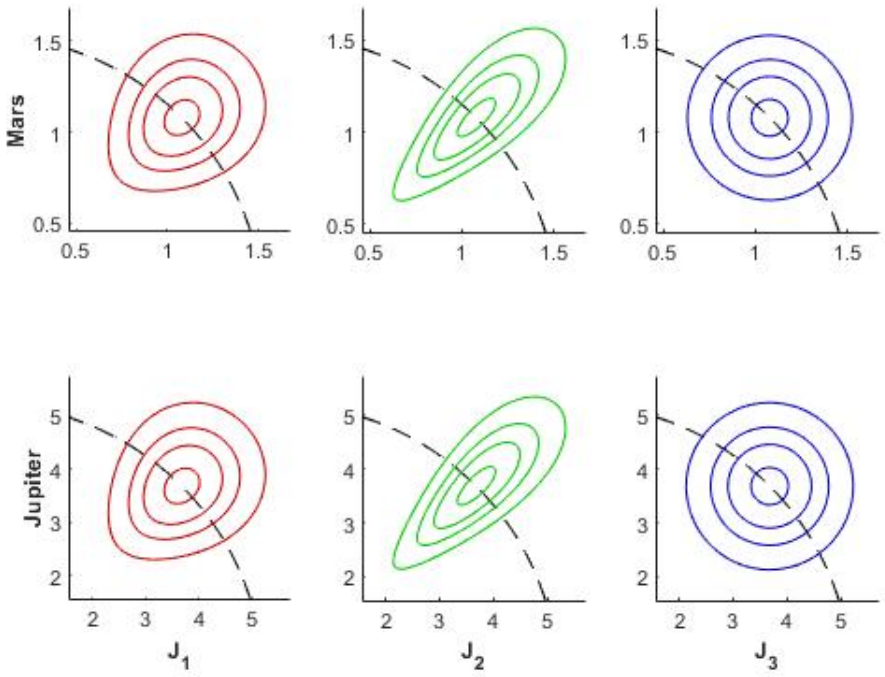

Figure 4.13 Contour representation of the three different cost functions considered.

All these three cost function types have been presented with $w(\eta) = 1$. The idea of considering a time-depending weighting function comes from the fact that is a way of telling the algorithm that we care more about closer time intervals rather than farther ones. If we do not include these weighting functions, the algorithm may find the best way to insert the spacecraft into the planet's orbit, but it can take a long time to do so. It is preferable to insert the spacecraft quicker, even if that translates into some more error in velocities, because then high thrust systems can take the lead. That is the motivation to consider weighting functions. We propose three scenarios:

- No time weighting. $w_1(\eta) = 1$.
- Decreasing linear weighting. $w_2(\eta) = N + 1 + N_\xi(\xi - 1) - \eta$
- Decreasing quadratic weighting. $w_3(\eta) = \left[N + 1 + N_\xi(\xi - 1) - \eta\right]^2$

With all these considerations, the new OCP problem to solve can be presented as

$$\min_{\tau,\alpha_n} \quad J_{m_{w_n}}$$

subject to

$$\begin{aligned}
\dot{r} &= v_r \\
\dot{\theta} &= \frac{v_\theta}{r} \\
\dot{v_r} &= \frac{v_\theta^2}{r} - \frac{\mu}{r^2} + \frac{\kappa}{2}\left(\frac{r_\oplus}{r}\right)\left(1 + \cos^2\alpha_n\right) \\
\dot{v_\theta} &= -\frac{v_r v_\theta}{r} + \frac{\kappa}{2}\left(\frac{r_\oplus}{r}\right)\cos\alpha_n \sin\alpha_n
\end{aligned} \tag{4.28}$$

$$\begin{aligned}
0 &\leqslant \kappa(t) \leqslant \kappa^{max}(t) \\
-\alpha_n^{max} &\leqslant \alpha_n(t) \leqslant \alpha_n^{max}
\end{aligned}$$

$$\begin{aligned}
r(0) &= r_\oplus \\
\theta(0) &= 0 \\
v_r(0) &= 0 \\
v_\theta(0) &= v_\oplus \\
t_e &= t_f^{nom} + \Delta t\, N_\xi(\xi - 1)
\end{aligned}$$

where $J_{m_{w_n}}$ means that we use the cost function of the type m, which can vary from one to three (J_1 J_2 and J_3 as defined above) using time-depending weights of the type n (w_1, w_2 and w_3, also defined above).

Studies and simulation results for missions to both Mars and Jupiter using these different cost function and time-depending weights definitions are conducted next.

4.4.3 Receding Horizon MPC Simulation results

We now conduct various simulations for missions to both Mars and Jupiter. The objective is to find the best strategy for each of them. It is of great importance to remember that this strategy is stable, or at least it does not have an apparent positive feedback loop in which it could fall. Therefore, it is expected that we reach our target every time, so it does not make sense anymore to keep track of variables like successful or failed missions, since we expect all of them to be successful. However, this stability property is obtained at the expense of not fixing the arrival time anymore, so our mission could last considerably longer than expected. Due to how the algorithm is built, it is not possible to arrive to the target earlier than expected, so our most optimistic scenario is to arrive at the same time that the nominal orbit predicted. Because of that, it is reasonable to conclude that the variable that must be tracked is time difference with respect to the nominal orbit, magnitude that we express as a percentage. We also compute the standard deviation of mission flight times, along with the number of times the strategy is able to reach the target in the same time as predicted in

nominal calculations (in other words, not having to add extra arcs).

We start our simulations with missions to Mars, because it is a good way of learning key conclusions before stepping into the harder and longer problem of reaching Jupiter. When performing simulations, an interesting phenomenon arises. There are certain cost function configurations in which a noticeable amount of simulations get stuck in an infinite loop. In those cases, the spacecraft gets really close to the target, entering in a circular orbit at its same distance to the Sun, with the difference that it has a gap in its true anomaly high enough to leave the spacecraft outside the planet's sphere of influence. One could then think that a phasing maneuver of some type could be made to account for this mismatch. Given that we have continuous thrust, the phasing arc may not have to be as long as an entire revolution around the Sun, differing from what is typically done. The problem is that, since we are building the cost function as the sum of errors not only at the corresponding instant but also at a fixed length future interval, the algorithm is not able to look far enough into the future to see that a phasing maneuver of that type could lead to a zero value cost function given that sufficient arcs are added. Thus, it prefers not to act, and leave thrust lever off, which leads to the spacecraft being at the same distance from the planet when the arc ends, entering in an infinite loop.

This phenomenon has been observed for combinations of cost functions and time-depending weights $\{J_2, w_1\}$ (2% of attempts) and $\{J_2, w_3\}$ (15% of attempts), having done 100 simulations for each of them. When a spacecraft enters in an infinite loop of this type, its distance to Mars is typically between 1 and 3.5 times its sphere of influence. That is really not a catastrophic misalignment, and maybe other types of propulsion systems could take over at that instant to approach the planet correctly, but it is definitely not ideal. We use some reasoning now to disregard more cost function combinations because they would also yield infinite loops. The first thing to notice is that we have used the cost function configuration J_2, which represents the equation of the weighted difference of squares in r and θ in (4.25). The problem that leads to the infinite loop is that the algorithm sees no benefit in stepping out from the orbit momentarily to then match it precisely, since it does not give future states enough importance. Given that, and recalling that it entered in infinite loops for weights w_1, which do not depend on time and give current state the same importance as the future ones, we can firmly assure that the same problem arises when using w_2, since now we are linearly prioritizing more recent states, and thus giving the algorithm a stronger reason to not deviate the spacecraft from where it currently is. Moreover, the algorithm not opting for stepping out from the orbit momentarily is the same as saying that it does not see any benefits in decreasing true anomaly error, because of the associated consequences. However, this error is precisely what is prioritized in J_2, as explained in Chapter 4.4.2, and even so, it enters infinite loops. This reasoning serves us to affirm that J_1 would also fail too, since it lacks that preference of reducing true anomaly gap that J_2 has because of the weights.

Having reported this phenomenon, we are only left with the third cost function, J_3. We perform simulations for all three types of time-depending weights w_1, w_2 and w_3. As usual, 100 simulations are conducted for each type. It is found that the algorithm now never falls into an infinite loop, which is promising. The increasing time results are presented in table 4.9. A histogram of final number of arcs is also included in figure 4.14.

Table 4.9 Performance comparison for Receding Horizon MPC for Mars missions using J_3 and different time-depending weightings.

Planet	Cost function	Weighting	$\overline{\Delta t_f}$ [%]	σ_{t_f} [%]	Attempts where $t_f = t_f^{nom}$ [%]
♂	J_3	w_1	6.75	14.53	72
		w_2	8.35	16.69	70
		w_3	5.15	12.80	76

Looking at the table 4.9, it is seen that the best option to minimize the increase in mission time is, in fact, choosing quadratic time-depending weights w_3. They yield the lowest mean time increase, along with lesser standard deviation in flight time and more attempts in which mission flight time is not increased. Results between w_1 and w_2 are, however, counter-intuitive; the addition of linear time-depending weights worsens the results compared to not adding weights at all. Other time-depending weight distributions could be studied as future work.

The performance improvement of this strategy compared to the other two previously developed is notorious. We have developed a guidance control law that guarantees our arrival to Mars, with just a 5% increase in

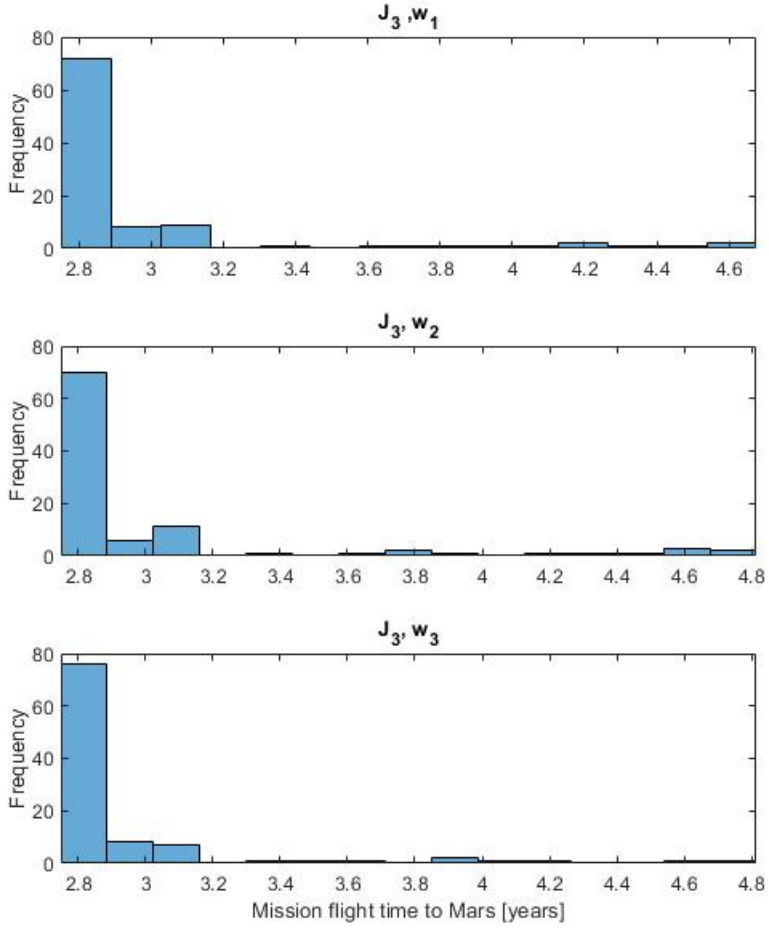

Figure 4.14 Histograms of mission flight time to Mars with RHMPC using different time-depending weights.

mission flight time, which is definitely preferable than having a non-negligible possibility of not reaching Mars at all.

We now begin with simulations to Jupiter. We have seen that the best option for the cost function appears to be J_3, so we choose that for our studies initially. The first study to conduct now is which weighting configuration is better for Jupiter, w_1, w_2 or w_3. These results are shown in table 4.10.

Table 4.10 Performance comparison for Receding Horizon MPC for Jupiter missions using J_3 and different weightings.

Planet	Cost function	Weighting	$\overline{\Delta t_f}$ [%]	σ_{t_f} [%]	Attempts where $t_f = t_f^{nom}$ [%]
♃	J_3	w_1	0	0	100
		w_2	0.06	0.44	98
		w_3	0.26	1.31	96

As it can be seen, w_1 yields the best possible results; w_3 is not the best option anymore, in contrast with what is seen for Mars. Interestingly, not adding time-depending weights is the best option in this case. The difference is so small that this variation in the results can be consequence of the relatively small number of simulations conducted in each case. Nonetheless, we still opt for w_1, since it has another advantage; not giving more priority at the nearer instant has a positive effect in the arrival velocity, reducing its error with respect to Jupiter's, since the algorithm "looks more" into the future. In fact, it is observed that errors in

velocity are quite low. For radial velocity (which should be 0 at the arrival), the absolute error is in the order of 0.005 UV, while the relative error for the tangential velocity is not greater than 0.8%. Since the algorithm is really effective for the cost function J_3, we do not conduct more analyses with J_1 nor J_2. Example missions' trajectory and evolution of variables using RHMPC strategy can be seen in figure 4.15 for Mars and in figure 4.16 for Jupiter. In these missions, no time has needed to be added in order to reach the targets properly. Examples in which extra arcs needed to be added can be found in Appendix B.

4.4.4 Limitations of Receding Horizon MPC Strategy

With this new strategy, we have solved a crucial flaw that caused issues in the previous sections: reliability. However, and as it has been observed, we have to carefully determine the error minimization cost function that we need to utilize. Otherwise, we may fall into an infinite loop; which even then is definitely a better scenario than the ones presented in previous strategies, since we remain quite close to the planet; but it definitely is not a feature to search for.

Another drawback of this strategy is that time is not fixed anymore. This fact may cause issues in missions that have a limited time-span, either because they carry degradable scientific tools or because of other reasons. However, it is unlikely that this strategy could be discarded because of that, since simulations show that this increment in time is remarkably low.

Regardless, this last strategy is undoubtedly the best one of the three developed since, with an adequate definition of the cost function, the spacecraft's arrival to the desired target is guaranteed.

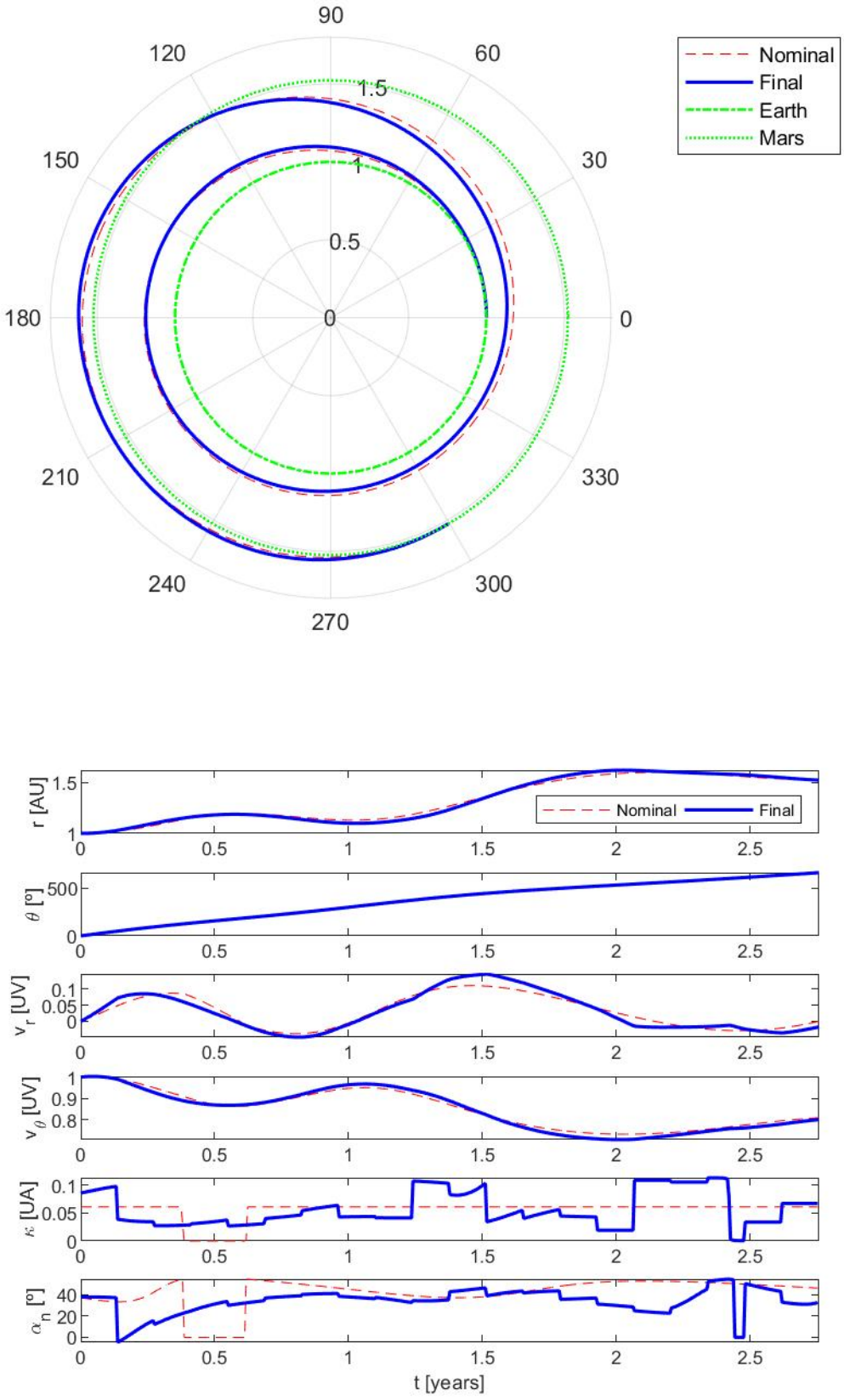

Figure 4.15 Trajectory and evolution of state and control variables in a mission To Mars using optimal Receding Horizon MPC.

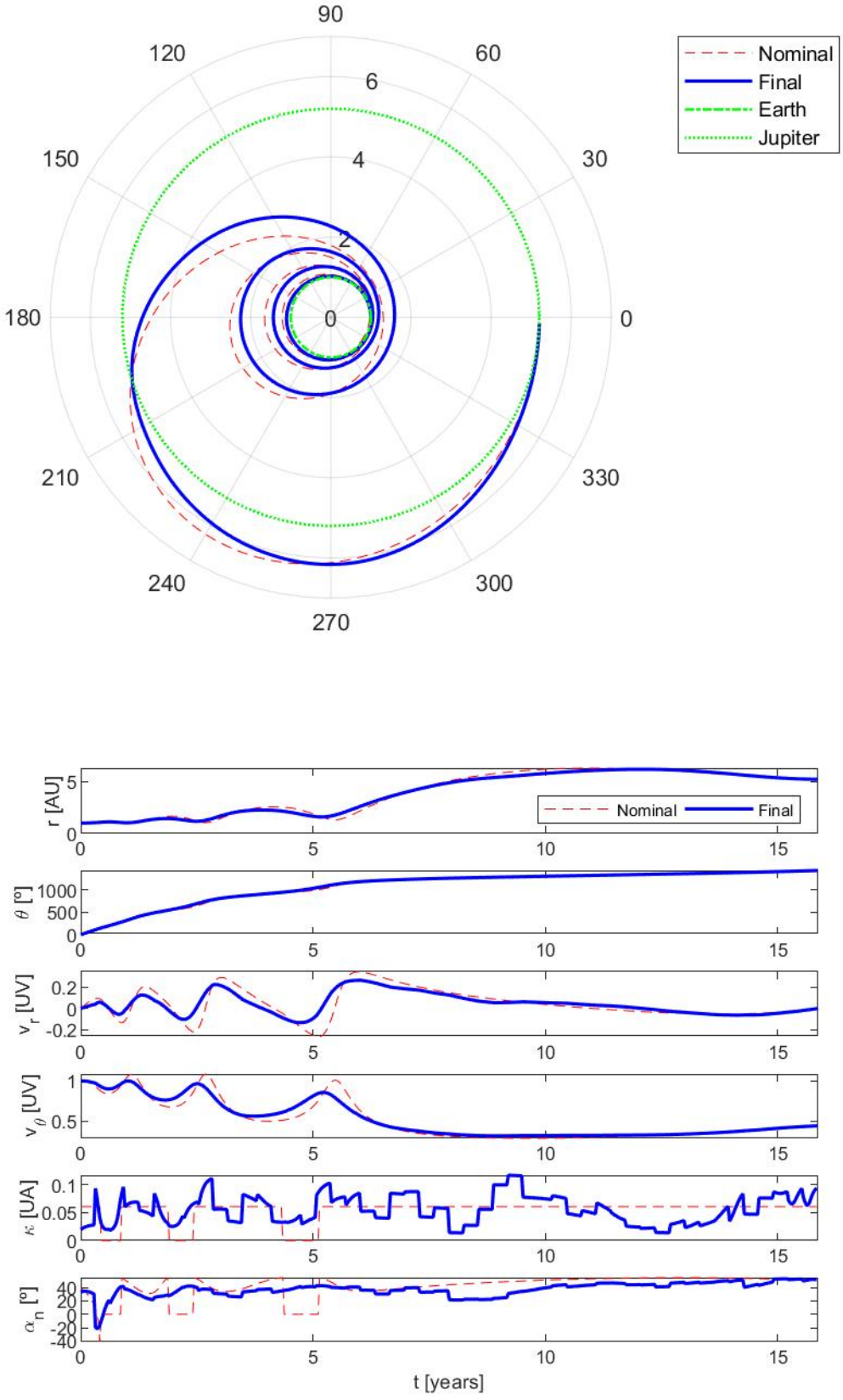

Figure 4.16 Trajectory and evolution of state and control variables in a mission To Jupiter using optimal Receding Horizon MPC.

5 Conclusions and future work

In this project, Esail's operating principle, development and current state of the art have been analysed. That has made the election of an adequate thrust model for the system possible, along with appropriate boundary values. Then, it has served as a good example to apply Optimal Control Theory to determine optimal planning orbits for missions to both Mars and Jupiter, along with the inclusion of a parametric study of flight times in terms of final orbit radius and characteristic acceleration. Then, we used that optimal planning to implement different guidance strategies involving LQR control and variations of MPC.

First, optimal nominal orbits have been calculated for interplanetary missions to Mars and Jupiter, and results have been compared to the ones in literature for Mars missions, concluding that they are remarkably similar. The principal difference is that, in most of other projects, the correspondent Optimal Control Problem was solved as a Two Point Boundary Value Problem (TPBVP), which is the formulation of the problem after applying Pontryagin's Minimum Principle and Euler-Lagrange equations, and obtaining boundary conditions accordingly. On the contrary, the problem in this project is solved by first discretizing time domain and transforming the OCP into a Non Linear Programming problem, which can be solved numerically with large scale non linear optimization algorithms such as IPOPT. In the final stages of the project, the time-optimal transfer orbit to Mars was solved using an indirect approach, and its results served as a comparison between solutions obtained using direct and indirect methods. Another lesson learned is that, even if the problem is not solved with an indirect approach, it is useful to study it anyway, since it can reveal simple laws that the optimal solution must follow (we anticipated bang-bang control using indirect methods). We also learned about the heuristic behaviour of algorithms like IPOPT when used to solve highly non convex optimization problems, and its sensitivity to initial guesses, as well as simple practices that we can include in future projects to add robustness to the solving method, for example, using the most recent orbit as the initial guess for the calculation of the next.

Investigations around solar wind uncertainty were also conducted, as well as its decay with respect to the distance from the Sun. We extracted a statistical model for the solar wind dynamic pressure from NASA OMNIWeb Database and other projects, and saw its effects on the behaviour of the Esail, which turned out to be only in saturation value, since a small study conducted on Esail's attitude revealed us the different scales of characteristic times.

We have also learned about LQR control as it was one of the guidance strategies proposed when solar perturbations were included. We studied its strengths and its limitations (such as not being able to impose tolerances to arrival conditions) as well as the effect on the solution of modifying weighting matrices.

A Shrinking Horizon MPC strategy was also presented, introducing us to Model Predictive Control. We developed a program that can often avoid infeasibilitty errors when a period of low dynamic pressure happens, by applying another strategy during that arc, similar to what is proposed in [38]. When the strategy is able to avoid those errors, it gets to the target with total precision in final conditions.

Lastly, we presented a Receding Horizon MPC strategy, in which the solution is extended into the future, and cost function is built in such a way that arrival velocities are not strong constraints anymore, but rather their error is minimized by the cost function. These two changes of extending the solution into the future

and modifying the cost function correctly led us to a strategy that was stable, compared to the previous two. It always reaches the target, the only drawback being that mission flight times can become considerably longer.

The conclusion to extract from these strategies is that, given that reliability is a requirement for any control strategy, it is better to opt for the Receding Horizon Model Predictive Control, even if that increases flight time. Moreover, it has been shown that this increase is, in fact, quite low. The stability properties of RHMPC make it highly useful, hence its common usage in other engineering scopes such as chemical batch processes.

This project has been conducted assuming a series of hypotheses that simplify the problem. Moreover, Optimal Control Theory is being constantly studied and it is applied to new systems everyday. Therefore, there are many varied improvements that can be made in this project, and that are proposed as future work. Our project presents a general idea on what to expect when dealing with optimal planning and guidance strategies in regards to Electric Solar Wind Sails, and these improvements should be thought as ways of refining the solution, or as necessary changes to apply these formulations to other problems or scenarios. Some of the improvements that can be made are presented next.

- Circular orbits hypothesis could be suppressed. We could consider the orbits real elliptic shapes by knowing the orbital elements $\{a, e, \omega, \theta(t)\}$. We can leave initial true anomaly value θ_0 free and get a new degree of freedom (due to the problem not being rotationally simetric anymore), so the algorithm not only solves for the optimal trajectory, but also the optimal launch date.
- 2D hypothesis can be suppressed too. By knowing all the set of orbital elements $\{a, e, i, \omega, \Omega, \theta(t)\}$ we know where planet is going to be exactly at any instant of time. By expressing the laws of motion in terms of orbital elements, the problem can be extended into 3D. However, classical orbit elements usually suffer from singularities, and the so called Modified Equinoctial Orbital Elements (MEOEs) are preferred.
- We could refine our Probability Density Function of dynamic pressure to better resemble data from NASA.
- In Direct Transcription to transform the OCP into a NLP problem, instead of discretizing time into equidistant nodes, an algorithm to find a more convenient adaptive mesh could be developed.
- Indirect methods can be developed for all the missions' optimal planning, as a way to compare the solutions with the obtained using direct transcription. Then the faster one can be chosen.
- Strategies for finding global minima can be included to further decrease mission flight time.
- Given that high computational power is available, a more exhaustive analysis could have conductive to correctly tune the LQR controller. Furthermore, an integral term can be added to the controller, along with its corresponding Anti Windup law.
- Other perturbations discarded, such as gravitational force exerted by other planets, could be implemented.
- In Receding Horizon MPC, more time-depending weight distributions can be studied.
- These experiments can be conducted to other planets. It may be interesting to study the case of Venus because of it being a planet closer to the Sun than the Earth.
- Guidance strategies for this problem that are prepared to deal with uncertainties could be developed using Stochastic Optimal Control Theory [54], potentially including MPC.

Appendix A
Flowchart of developed MATLAB programs

A.1 Shrinking Horizon MPC Strategy

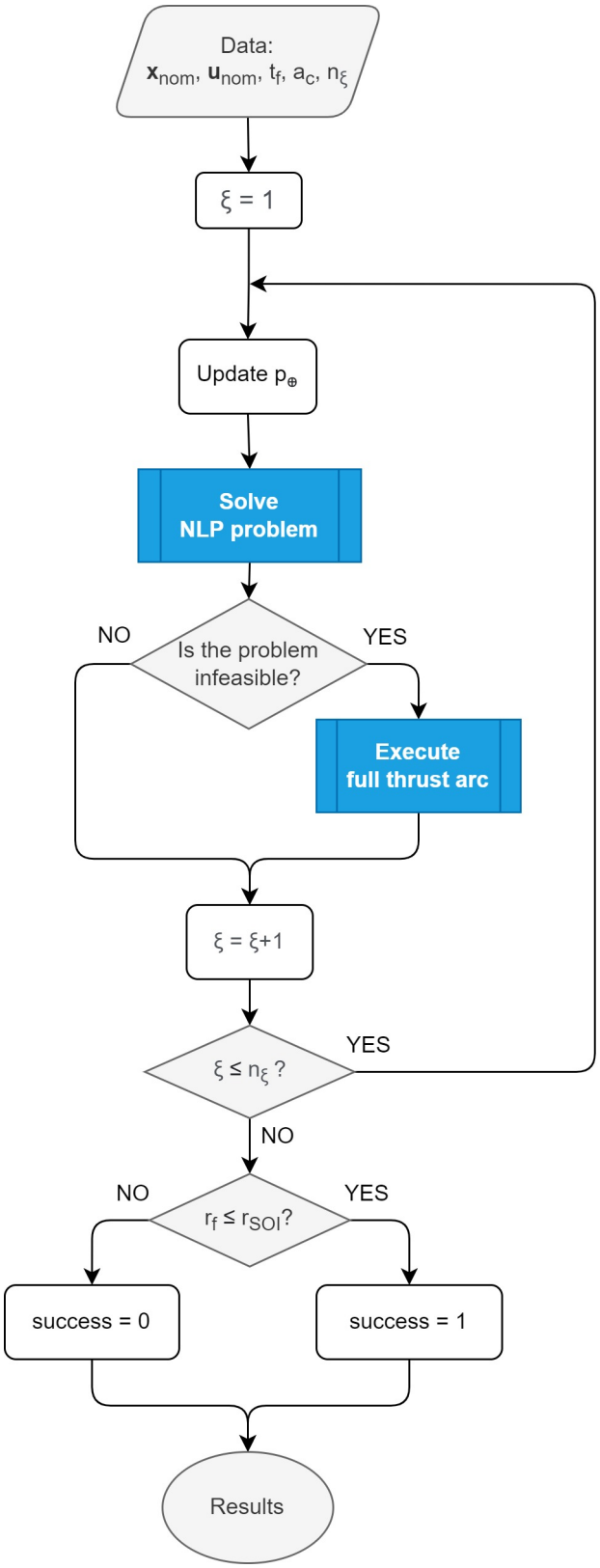

Figure A.1 Flowchart for Shrinking Horizon MPC Strategy MATLAB program.

A.2 Receding Horizon MPC Strategy

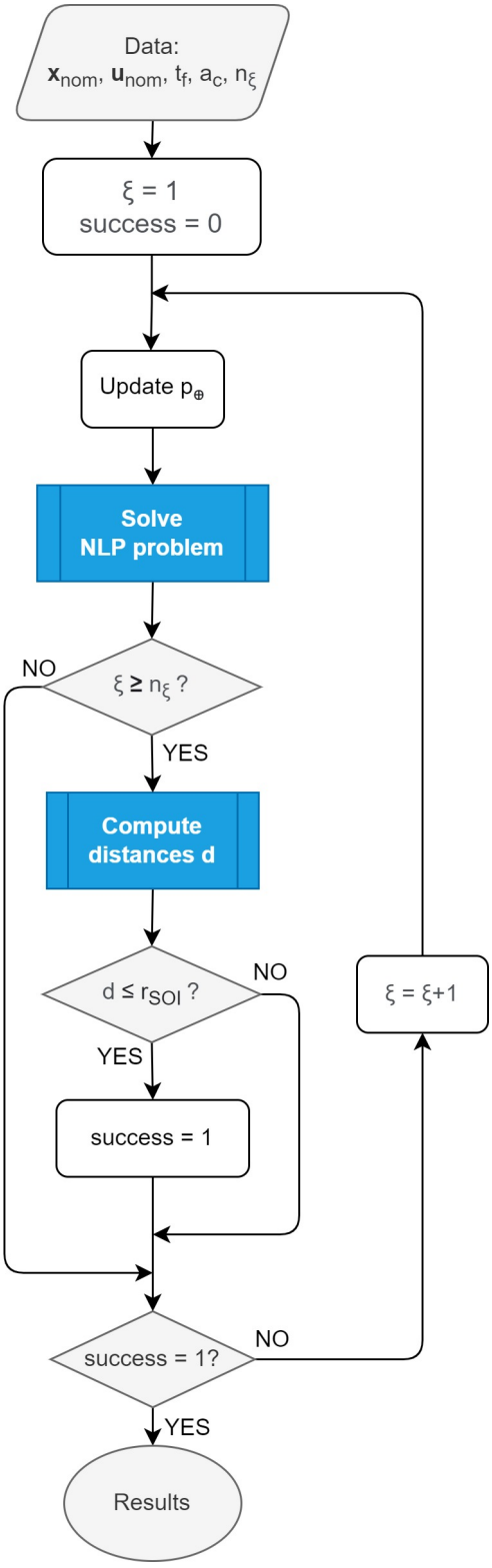

Figure A.2 Flowchart for Receding Horizon MPC Strategy MATLAB program.

Appendix B
Esail additional mission simulations for different guidance strategies

In this appendix, we present additional figures that contain visual representations of mission trajectories and the evolution of state and control variables. These figures are listed below:

- In figure B.1, a successful Mars mission using LQR control is presented and, in figure B.2, a failed example.
- In figures B.3 and B.4, failed missions for Mars and Jupiter using SHMPC are presented. It can be seen that the spacecraft enters a *full thrust arc* quite early, and it is not able to recover from that situation, thus not tracking the nominal orbit and ending considerably far from it.
- In figures B.5 and B.6 we present trajectories that reached Mars and Jupiter respectively, but took considerably longer than expected. It can be seen that, in both cases, the spacecraft is not able to reach the corresponding planet at the arrival due to solar wind perturbations, but in both missions the spacecraft is able to correct its orbit to eventually reach it. In the case of Jupiter, it is observed that a coasting arc was performed during the correction maneuvers.

B.1 LQR Control Strategy

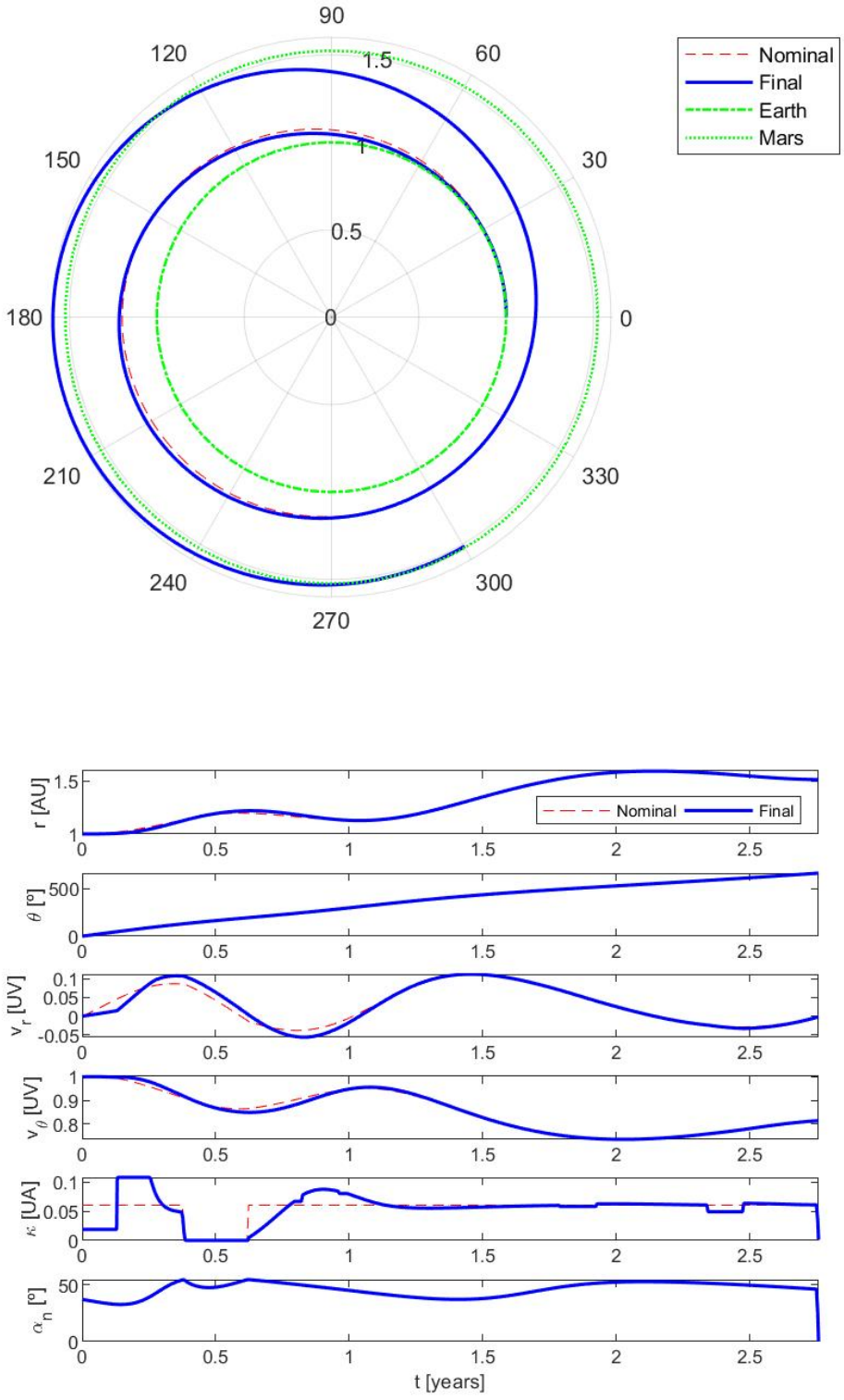

Figure B.1 Trajectory and evolution of state and control variables in a successful mission to Mars using Finite Horizon LQR with unit diagonal weighting matrices.

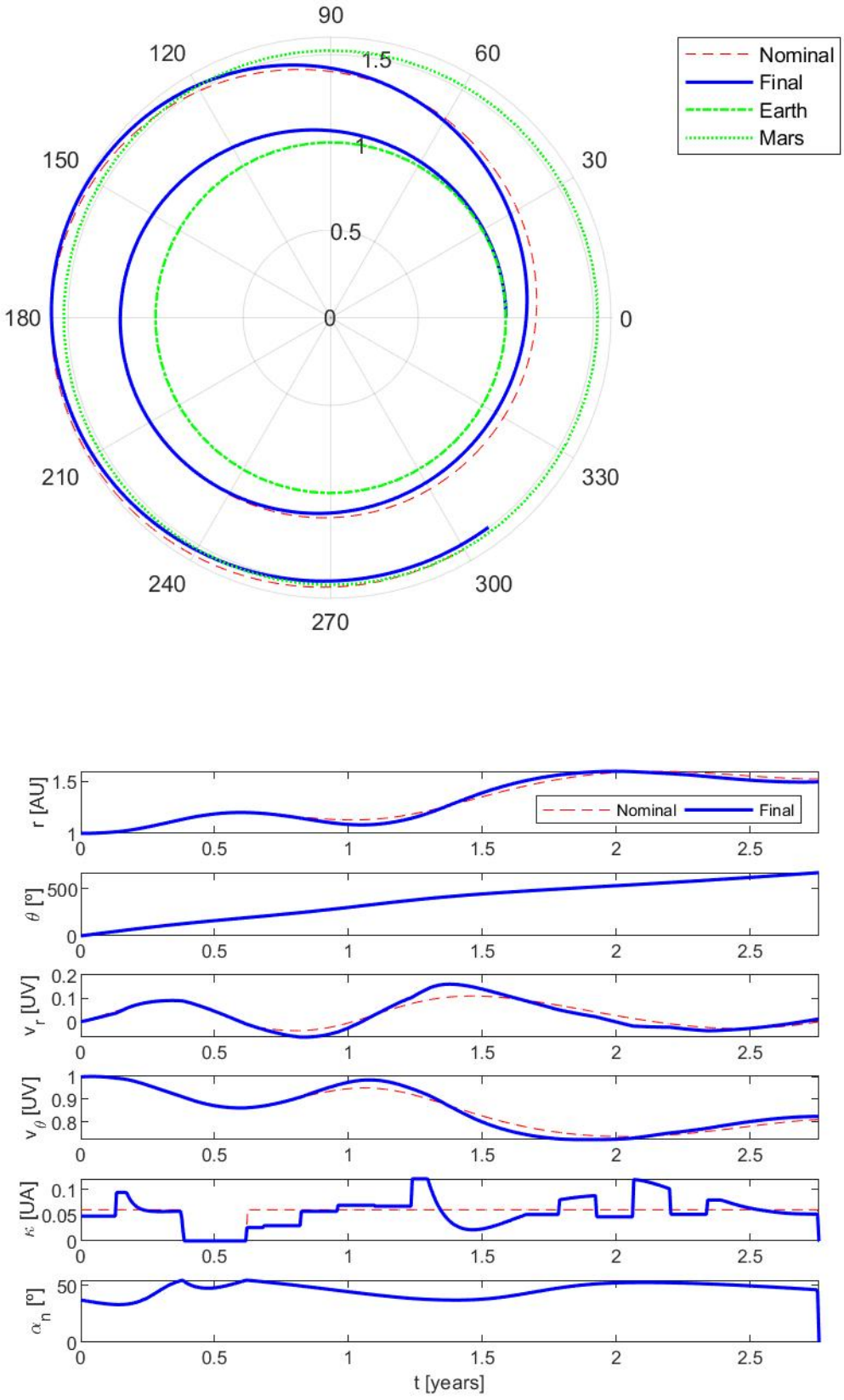

Figure B.2 Trajectory and evolution of state and control variables in a failed mission to Mars using Finite Horizon LQR with unit diagonal weighting matrices.

B.2 Shrinking Horizon MPC Strategy

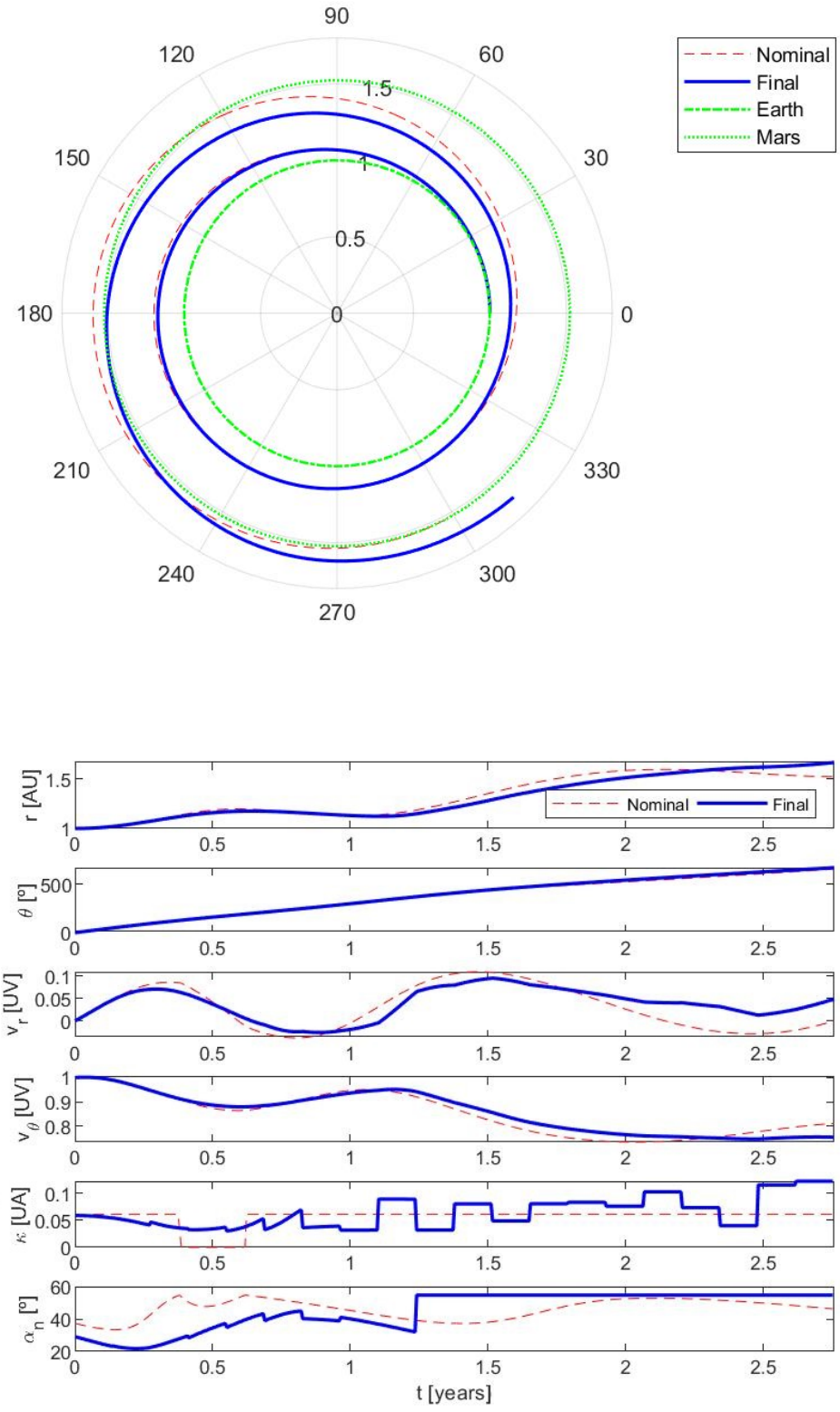

Figure B.3 Trajectory and evolution of state and control variables in a failed mission to Mars using optimal Shrinking Horizon MPC.

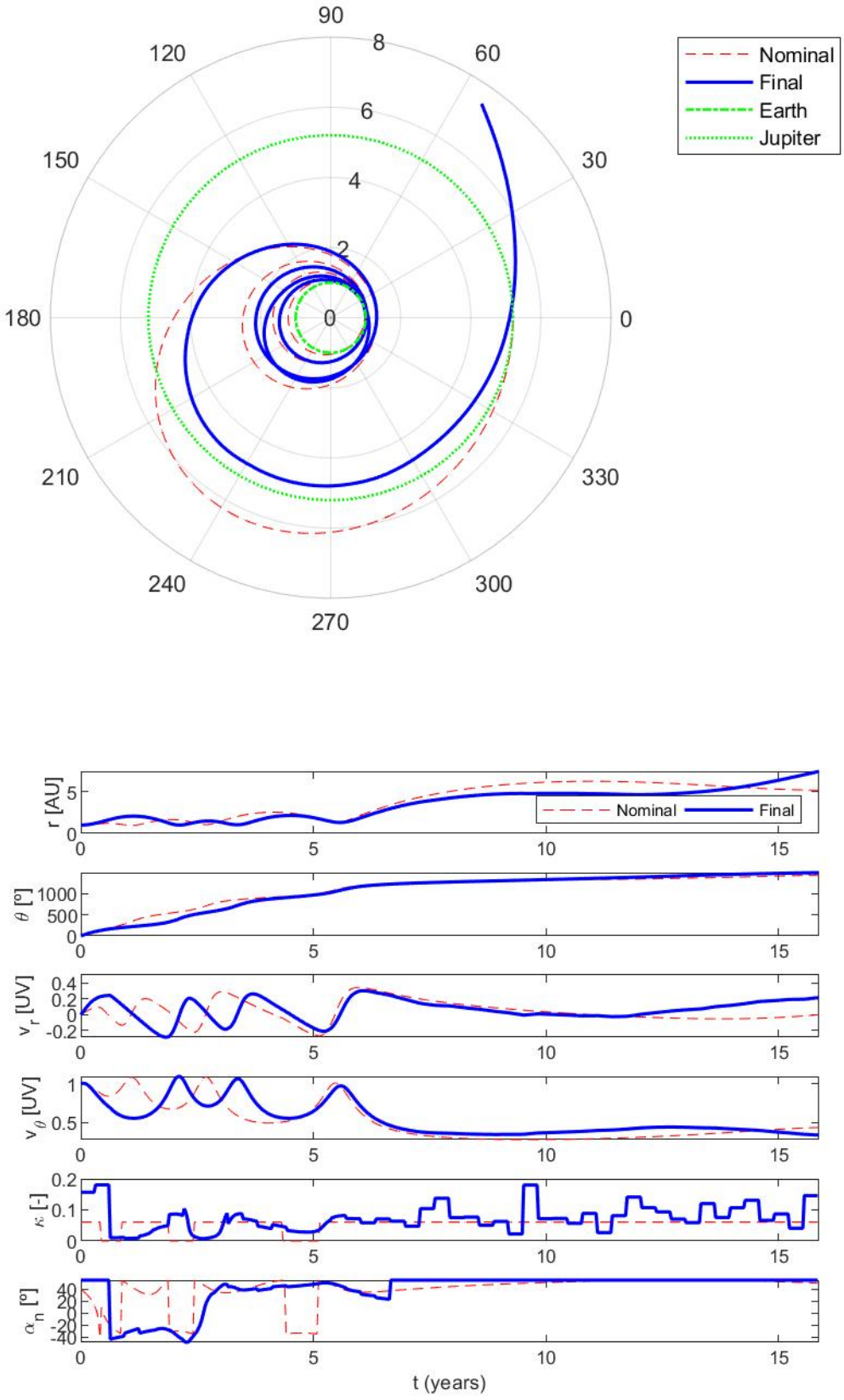

Figure B.4 Trajectory and evolution of state and control variables in a failed mission to Jupiter using optimal Shrinking Horizon MPC.

B.3 Receding Horizon MPC Strategy

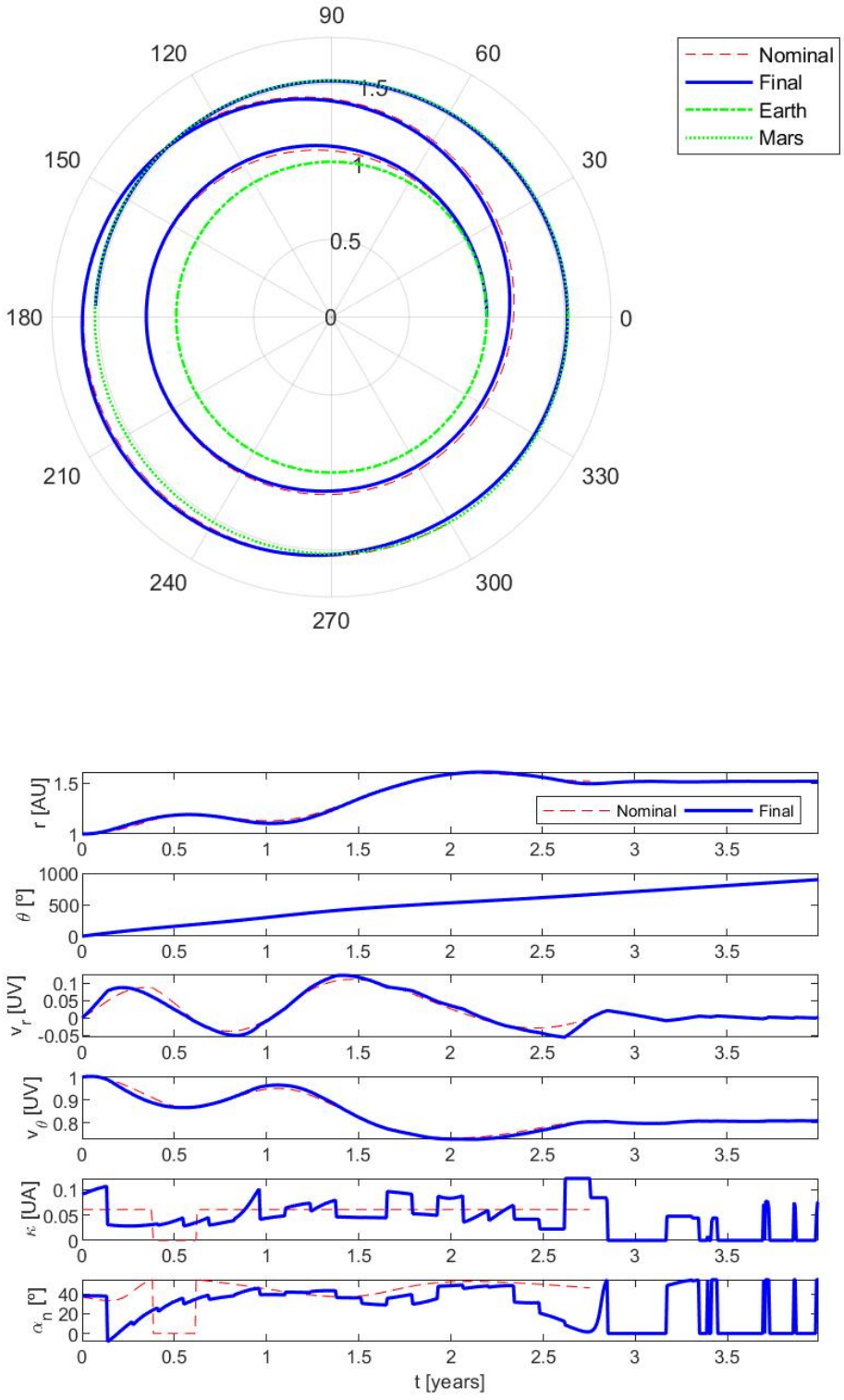

Figure B.5 Trajectory and evolution of state and control variables in a prolonged mission to Mars using Receding Horizon MPC.

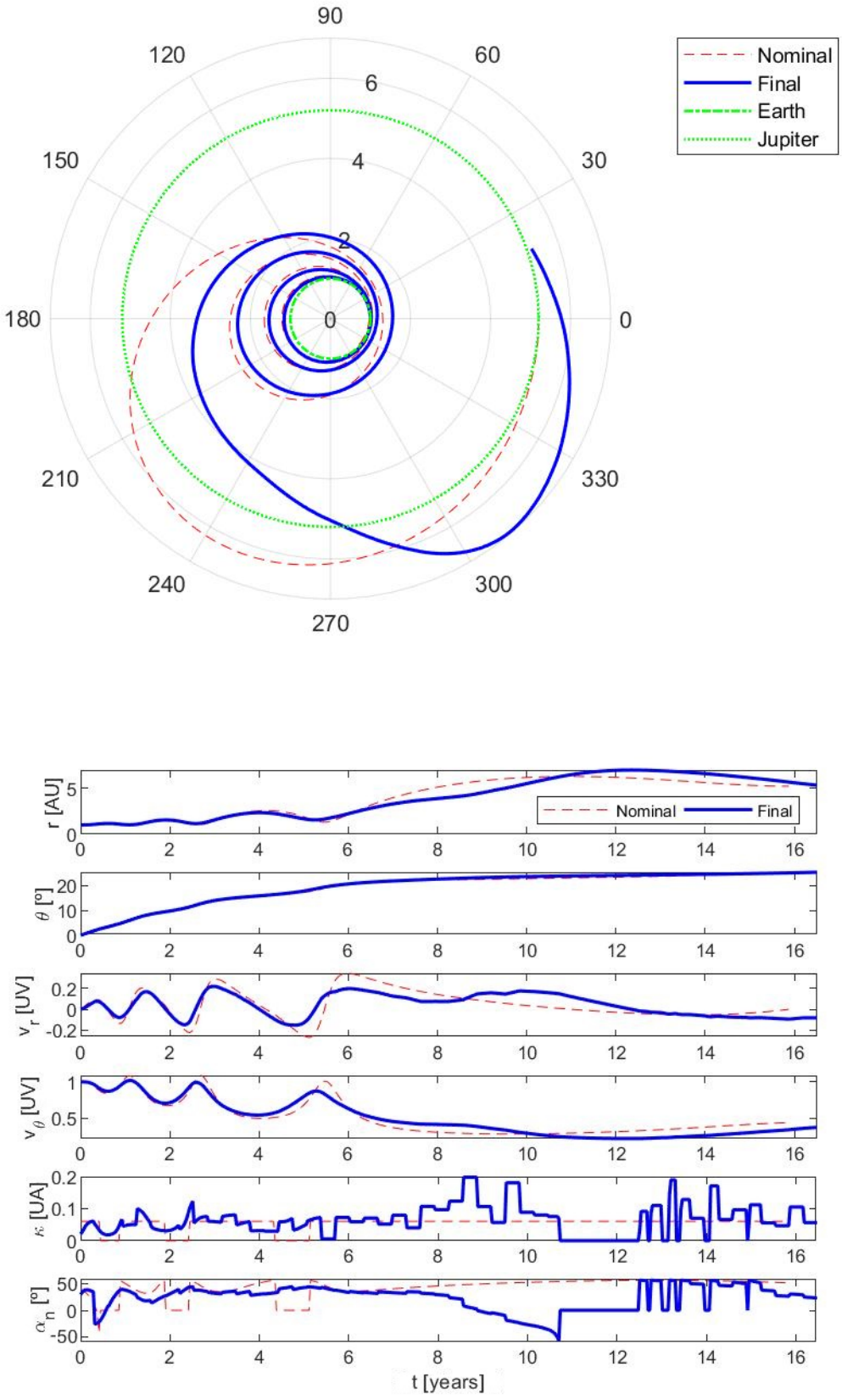

Figure B.6 Trajectory and evolution of state and control variables in a prolonged mission to Jupiter using Receding Horizon MPC.

Bibliography

[1] M. Bassetto, G. Mengali, and A. Quarta, "Thrust and torque vector characteristics of axially-symmetric e-sail," *Acta Astronautica*, vol. 146, 03 2018.

[2] L. Niccolai, A. Anderlini, G. Mengali, and A. A. Quarta, "Impact of solar wind fluctuations on electric sail mission design," *Aerospace Science and Technology*, vol. 82-83, pp. 38–45, 2018. [Online]. Available: https://www.sciencedirect.com/science/article/pii/S1270963818311040

[3] L. Niccolai, A. Anderlini, G. Mengali, and A. Quarta, "Electric sail displaced orbit control with solar wind uncertainties," *Acta Astronautica*, vol. 162, 07 2019.

[4] G. A. Flandro, "Fast reconnaissance missions to the outer solar system utilizing energy derived from the gravitational field of jupiter," *Astronautica Acta*, vol. 12, pp. 329–337, 1966.

[5] D. A. Spencer, B. Betts, J. M. Bellardo, A. Diaz, B. Plante, and J. R. Mansell, "The lightsail 2 solar sailing technology demonstration," *Advances in Space Research*, vol. 67, no. 9, pp. 2878–2889, 2021, solar Sailing: Concepts, Technology, and Missions II. [Online]. Available: https://www.sciencedirect.com/science/article/pii/S027311772030449X

[6] P. Janhunen, "Electric sail for spacecraft propulsion," *Journal of Propulsion and Power - J PROPUL POWER*, vol. 20, pp. 763–764, 07 2004.

[7] S. p. Gong and M. Macdonald, "Review on solar sail technology," *Astrodynamics*, vol. 3, 03 2019.

[8] P. Janhunen, P. K. Toivanen, J. Polkko, S. Merikallio, P. Salminen, E. Haeggström, H. Seppänen, R. Kurppa, J. Ukkonen, S. Kiprich, G. Thornell, H. Kratz, L. Richter, O. Krömer, R. Rosta, M. Noorma, J. Envall, S. Lätt, G. Mengali, A. A. Quarta, H. Koivisto, O. Tarvainen, T. Kalvas, J. Kauppinen, A. Nuottajärvi, and A. Obraztsov, "Invited article: Electric solar wind sail: Toward test missions," *Review of Scientific Instruments*, vol. 81, no. 11, p. 111301, 2010. [Online]. Available: https://doi.org/10.1063/1.3514548

[9] N. Perakis, "Maneuvering through solar wind using magnetic sails," *Acta Astronautica*, vol. 177, 07 2020.

[10] P. Janhunen, "Increased electric sail thrust through removal of trapped shielding electrons by orbit chaotisation due to spacecraft body," *Annales Geophysicae*, vol. 27, no. 8, pp. 3089–3100, 2009. [Online]. Available: https://angeo.copernicus.org/articles/27/3089/2009/

[11] ——, "Photonic spin control for solar wind electric sail," *Acta Astronautica*, vol. 83, pp. 85–90, 2013. [Online]. Available: https://www.sciencedirect.com/science/article/pii/S0094576512003955

[12] M. Lingam and A. Loeb, "Electric sails are potentially more effective than light sails near most stars," *Acta Astronautica*, vol. 168, pp. 146–154, mar 2020. [Online]. Available: https://doi.org/10.1016%2Fj.actaastro.2019.12.013

[13] A. Slavinskis, M. Pajusalu, H. Kuuste, E. Ilbis, T. Eenmäe, I. Sünter, K. Laizans, H. Ehrpais, P. Liias, E. Kulu, J. Viru, J. Kalde, U. Kvell, J. Kütt, K. Zalite, K. Kahn, S. Lätt, J. Envall, P. Toivanen, and M. Noorma, "Estcube-1 in-orbit experience and lessons learned (harry rowe mimno award 2016)," *IEEE Aerospace and Electronic Systems Magazine*, vol. 30, pp. 12–22, 10 2015.

[14] B. M. Wiegmann, *The Heliopause Electrostatic Rapid Transit System (HERTS) - Design, Trades, and Analyses Performed in a Two Year NASA Investigation of Electric Sail Propulsion Systems*, 07 2017. [Online]. Available: https://arc.aiaa.org/doi/abs/10.2514/6.2017-4712

[15] P. Janhunen, S. Merikallio, and M. Paton, "Emmi—electric solar wind sail facilitated manned mars initiative," *Acta Astronautica*, vol. 113, pp. 22–28, 2015. [Online]. Available: https://www.sciencedirect.com/science/article/pii/S0094576515001290

[16] A. Quarta, G. Mengali, and P. Janhunen, "Electric sail for a near-earth asteroid sample return mission: Case 1998 ky26," *asce journal of aerospace engineering*, vol. 27, 11 2014.

[17] A. Quarta and G. Mengali, "Electric sail mission analysis for outer solar system exploration," *Journal of Guidance, Control, and Dynamics*, vol. 33, pp. 740–755, 05 2010.

[18] A. Slavinskis, P. Janhunen, P. Toivanen, K. Muinonen, A. Penttilä, M. Granvik, T. Kohout, M. Gritsevich, A. Slavinskis, M. Pajusalu, I. Sünter, H. Ehrpais, J. Dalbins, I. Iakubivskyi, T. Eenmäe, M. Pajusalu, E. Ilbis, H. Ehrpais, K. Muinonen, M. Gritsevich, D. Mauro, J. Stupl, A. S. Rivkin, and W. F. Bottke, "Nanospacecraft fleet for multi-asteroid touring with electric solar wind sails," in *2018 IEEE Aerospace Conference*, 2018, pp. 1–20.

[19] P. Janhunen, P. Toivanen, J. Envall, S. Merikallio, G. Montesanti, J. Gonzalez del Amo, U. Kvell, M. Noorma, and S. Lätt, "Electric solar wind sail applications overview," *Proceedings of the Estonian Academy of Sciences*, vol. 63, 04 2014.

[20] A. Quarta, G. Mengali, and P. Janhunen, "Electric sail option for cometary rendezvous," *Acta Astronautica*, vol. 127, 06 2016.

[21] M. Bassetto, G. Mengali, and A. Quarta, "E-sail attitude control with tether voltage modulation," *Acta Astronautica*, vol. 166, 10 2019.

[22] M. Walker, B. Ireland, and J. Owens, "A set modified equinoctial orbit elements," *Celestial mechanics*, vol. 36, no. 4, pp. 409–419, 1985.

[23] M. Bassetto, A. Quarta, and G. Mengali, "Locally-optimal electric sail transfer," *Proceedings of the Institution of Mechanical Engineers, Part G: Journal of Aerospace Engineering*, vol. 233, p. 095441001772897, 09 2017.

[24] P. Janhunen and A. Sandroos, "Simulation study of solar wind push on a charged wire: Basis of solar wind electric sail propulsion," *Annales Geophysicae*, vol. 25, pp. 755–767, 03 2007.

[25] A. Quarta and G. Mengali, "Analysis of electric sail heliocentric motion under radial thrust," *Journal of Guidance, Control, and Dynamics*, vol. 39, pp. 1–5, 12 2015.

[26] G. Mengali, A. Quarta, P. Janhunen, A. Sandroos, C. Kluever, B. Wie, V. Coverstone, and B. Dachwald, "Electric sail performance analysis," *Journal of Spacecraft and Rockets*, vol. 45, pp. 122–129, 01 2008.

[27] K. Yamaguchi and H. Yamakawa, "Study on orbital maneuvers of electric sail with on-off thrust control," *AEROSPACE TECHNOLOGY JAPAN, THE JAPAN SOCIETY FOR AERONAUTICAL AND SPACE SCIENCES*, vol. 12, pp. 79–88, 09 2013.

[28] P. K. Toivanen and P. Janhunen, "Spin plane control and thrust vectoring of electric solar wind sail," *Journal of Propulsion and Power*, vol. 29, no. 1, pp. 178–185, 2013. [Online]. Available: https://doi.org/10.2514/1.B34330

[29] M. Huo, G. Mengali, and A. Quarta, "Electric sail thrust model from a geometrical perspective," *Journal of Guidance, Control, and Dynamics*, vol. 41, pp. 1–7, 10 2017.

[30] P. Janhunen, A. Quarta, and G. Mengali, "Electric solar wind sail mass budget model," *Geoscientific Instrumentation, Methods and Data Systems*, vol. 2, pp. 85–95, 02 2013.

[31] A. E. Bryson and Y. C. Ho, *Applied Optimal Control*. New York: Blaisdell, 1969.

[32] D. F. Lawden, *Optimal Trajectories for Space Navigation*. London: Butterworths, 1963.

[33] J. T. Betts, "Survey of numerical methods for trajectory optimization," *Journal of Guidance, Control, and Dynamics*, vol. 21, no. 2, pp. 193–207, 1998. [Online]. Available: https://doi.org/10.2514/2.4231

[34] F. Topputo and C. Zhang, "Survey of direct transcription for low-thrust space trajectory optimization with applications," *Abstract and Applied Analysis*, vol. 2014, pp. 1–15, 06 2014.

[35] H. Lei, T. Liu, D. Li, and J. Ye, "Adaptive mesh refinement method for optimal control based on hermite-legendre-gauss-lobatto direct transcription," *Journal of Vibroengineering*, vol. 19, 12 2017.

[36] P. Williams, "Hermite–legendre–gauss–lobatto direct transcription in trajectory optimization," *Journal of Guidance Control and Dynamics - J GUID CONTROL DYNAM*, vol. 32, pp. 1392–1395, 07 2009.

[37] J. A. E. Andersson, J. Gillis, G. Horn, J. B. Rawlings, and M. Diehl, "CasADi – A software framework for nonlinear optimization and optimal control," *Mathematical Programming Computation*, vol. 11, no. 1, pp. 1–36, 2019.

[38] A. Caruso, L. Niccolai, G. Mengali, and A. Quarta, "Electric sail trajectory correction in presence of environmental uncertainties," *Aerospace Science and Technology*, vol. 94, p. 105395, 09 2019.

[39] A. A. Quarta and G. Mengali, "Minimum-time trajectories of electric sail with advanced thrust model," *Aerospace Science and Technology*, vol. 55, pp. 419–430, 2016. [Online]. Available: https://www.sciencedirect.com/science/article/pii/S1270963816302322

[40] M. A. Paluszek and S. J. Thomas, "Trajectory optimization using global methods iepc05-173," in *The 29th International Electric Propulsion Conference*, 2005, p. 15.

[41] M. Molga and C. Smutnicki, "Test functions for optimization needs," *Test functions for optimization needs*, vol. 101, p. 48, 2005.

[42] B. D. O. Anderson and J. B. Moore, *Optimal Control: Linear Quadratic Methods*. USA: Prentice-Hall, Inc., 1990.

[43] L. Guarnaccia, R. Bevilacqua, and S. Pastorelli, "Suboptimal lqr-based spacecraft full motion control: Theory and experimentation," *Acta Astronautica*, vol. 122, 02 2016.

[44] R. Quero Campos, "Planificación y guiado óptimos de la trayectoria de ascenso a órbita de un vehículo lanzador sometida a perturbaciones y errores de modelado," 2021.

[45] L. Pandolfi, "Controllability and stabilization for linear systems of algebraic and differential equations," *Journal of Optimization Theory and Applications*, vol. 30, no. 4, pp. 601–620, 1980.

[46] I. H. Whang and T. W. Hwang, "Horizontal waypoint guidance design using optimal control," *IEEE Transactions on Aerospace and Electronic Systems*, vol. 38, no. 3, pp. 1116–1120, 2002.

[47] F. G. Jiménez, "Sistemas de control y guiado para vehículos aéreos no tripulados: Diseño de algoritmos y sistemas embarcados," Ph.D. dissertation, Universidad de Sevilla, 2012.

[48] S. Galeani, S. Tarbouriech, M. Turner, and L. Zaccarian, "A tutorial on modern anti-windup design," in *2009 European Control Conference (ECC)*, 2009, pp. 306–323.

[49] L. Magni, G. De Nicolao, R. Scattolini, and F. Allgöwer, "Robust model predictive control for nonlinear discrete-time systems," *International Journal of Robust and Nonlinear Control: IFAC-Affiliated Journal*, vol. 13, no. 3-4, pp. 229–246, 2003.

[50] W. B. Greer and C. Sultan, "Shrinking horizon model predictive control method for helicopter–ship touchdown," *Journal of Guidance, Control, and Dynamics*, vol. 43, no. 5, pp. 884–900, 2020.

[51] A. Quarta, G. Mengali, and P. Janhunen, "Optimal interplanetary rendezvous combining electric sail and high thrust propulsion system," *Acta Astronautica*, vol. 68, pp. 603–621, 03 2011.

[52] W. H. Kwon and S. H. Han, *Receding horizon control: model predictive control for state models*. Springer Science & Business Media, 2006.

[53] F. Gavilan, R. Vazquez, and E. Camacho, "An iterative model predictive control algorithm for uav guidance," *IEEE Transactions on Aerospace and Electronic Systems*, vol. 51, pp. 2406–2419, 07 2015.

[54] W. H. Fleming and R. W. Rishel, *Deterministic and stochastic optimal control*. Springer Science & Business Media, 2012, vol. 1.

Glossary

AU Astronomical Units. 4, 21

Esail Electric Solar Wind Sail. 3

HJB equation Hamilton-Jacobi-Bellman equation. 23

LQR Linear Quadratic Regulator. 49, 52

MEOEs Modified Equinoctial Orbital Elements. 10

MPC Model Predictive Control. 49, 63, 73

NLP Non Linear Programming. 22, 63

OCP Optimal Control Problem. 20

PDF Probability Density Function. 15

PMP Pontryagin's Minimum Principle. 23

RHMPC Receding Horizon Model Predictive Control. 73

SHMPC Shrinking Horizon Model Predictive Control. 63

SOI Sphere Of Influence. 17

TPBVP Two Point Boundary Value Problem. 22

UA Units of Acceleration. 21

UT Units of Time. 21

UV Units of Velocity. 21